Università degli Studi di Napoli Federico II
-
Dottorato di Ricerca in Fisica Fondamentale ed Applicata
18° ciclo

Dott. Francesco Vita

Switchable Bragg Gratings

Based on Soft Materials

Il Coordinatore
Prof. A. Tagliacozzo

Novembre 2005

Table of contents

Introduction **3**

1 Liquid crystals **7**

1.1 Between liquids and crystals 7

1.2 Physics of nematics 7

1.2.1 The order parameter 7

1.2.2 Continuum theory 8

1.2.3 External field effect 10

1.2.4 Freédericksz effect 11

1.2.5 Reorientation dynamics 13

1.3 Optics of liquid crystals 15

1.4 Polymer dispersed liquid crystals 16

1.4.1 Introduction 16

1.4.2 Preparation and morphology 16

1.4.3 Optical properties 17

1.4.4 Switching properties 18

2 Holographic gratings **19**

2.1 Introduction and classification 19

2.2 Rigorous formulation of the diffraction problem 20

2.2.1 The Floque theorem and the Bragg condition 20

2.2.2 The system of coupled differential equations 23

2.3 Diffraction from thin gratings 24

2.4 Diffraction from thick gratings 25
2.4.1 Kogelnik theory 25
2.4.2 Diffraction efficiency for transmission gratings 26
2.4.3 Diffraction efficiency for reflection gratings 28
2.5 Diffraction from thick anisotropic gratings 28
2.5.1 Montemezzani and Zgonik's theory 28
2.5.2 Transmission gratings 30
2.5.3 Reflection gratings 32
2.6 Criteria for thin-thick grating classification 32

3 Holographic gratings in LC-polymer composites 33

3.1 Introduction 33
3.2 Production procedure 35
3.2.1 Set-up 35
3.2.2 Sample preparation 36
3.2.3 Exposure 37
3.3 Materials 38
3.3.1 Monomers 38
3.3.2 Liquid crystals 41
3.3.3 Photoinitiators 42
3.3.4 Reactive diluent 43
3.3.5 Surfactants 44
3.4 Formation dynamics 44
3.5 Non-droplet gratings: Policryps and Poliphem 47
3.5.1 A new class of LC-polymer gratings 47

3.5.2 Policryps 48

3.5.3 Poliphem 49

4 H-PDLC gratings: characterization and modeling 53

4.1 Introduction 53

4.2 Angular measurements 54

4.2.1 Experimental 54

4.2.2 Data fitting 56

4.3 Morphological model 58

4.4 Comments on the effects of the optical dispersion 62

4.5 Measurements under electric field 64

5 Policryps and Poliphem characterization 67

5.1 Introduction 67

5.2 Thermal properties 68

5.3 Diffraction efficiency and switching properties 69

5.4 Bandwidth and losses 71

5.5 Switching times 73

5.5.1 Policryps dynamic measurements 73

5.5.2 A model for Policryps dynamics: switching off 76

5.5.3 A model for Policryps dynamics: switching on 78

6 Optical characterization of soft materials 83

6.1 Introduction 83

6.2 Experimental techniques 84

6.2.1 Spectroscopic ellipsometry 84

6.2.2 Half-leaky guided mode technique 86

6.3 Optical dispersion in liquid crystal 87

6.3.1 HLGM measurements on liquid crystals 87

6.3.2 Ellipsometric measurements on liquid crystals 89

6.3.3 E7 and 5CB dispersion spectra 91

Bibliography **95**

Acknowledgments

The present work has been carried out at the Integrated Optics Laboratory of the University of Naples, under the precious guide of Prof. Abbate. From him I received advice, knowledge, stimulation, and opportunities.

I am also very grateful to Dr. Marino and Dr. Tkachenko: we worked together every day and they definitely had a part in all my researches.

The present work would have been impossible without a fruitful collaboration with many scientific groups, which provided me with materials, ideas and experience. My sincere thanks goes to:

- Prof. Simoni and his group at the Polythecnic University of Marche (Ancona, Italy);
- Prof. Umeton and his groups at the University of Calabria (Cosenza, Italy);
- Prof. Stumpe and Dr. Slussarenko at the Fraunhofer Institute for Applied Polymer Research (Potsdam, Germany);
- Prof. Crawford and his group at the Brown University (Providence RI, USA).

And after the professional acknowledgments, the personal ones. Again a special thanks to Giancarlo, Antigone, and Vladimir: more than colleagues, they were close friends; it was a pleasure to share with them most days of the last three years. I hope to keep having coffee breaks together!

I must thanks two special persons, Ferdinando and Giovanni: they do not even know what liquid crystals are (although I have tried to explain it so many times), but their friendship was really important for me in these years; so there is a bit of them in this work.

Finally and above all, I will be eternally grateful to my parents and my brother Luca: things change with time, but their presence is still fundamental in my life. Without them, I would never be arrived at this moment.

To my family

The real voyage of discovery
consists not in seeking new landscapes
but in having new eyes
Marcel Proust

Introduction

Nowadays optics plays a major role in telecommunications. Optical fibers are the long-time established backbone for long-haul data transmission. However, a great limit to the full development of optical telecom networks is set by the need of electro-optical conversions for operations like routing, (de-)multiplexing, equalization, data control, etc. All these tasks are now performed by electronic devices, which require the signal to be decoupled from the fiber, converted to electrical, elaborated, reconverted to optical, and coupled back into the fiber. This process results in elevated coupling losses, low transmission rates and high costs. At present, realization and optimization of new devices, acting directly on the optical signal, is among the main goals of research in the telecom field.

In this regard, many different technologies have been proposed: MEMS (micro electro-mechanical systems), devices exploiting the electro-optical, acusto-optical, or thermo-optical effect in media like $LiNbO_3$, polymers, silica, semiconductors, etc., devices based on the bubble technology, and finally liquid crystals (LCs). Actually, research is still in progress [1] and none of these technologies is definitely established on the market. However, the so-called *soft materials* (liquid crystals, polymers, gels) seem very promising and advantageous in many respects when compared with more traditional hard materials (semiconductors, metals, glasses).

In particular, polymers attracted a great interest ever since the early studies on their optical properties. As a matter of fact, the real utilization of polymers in the field of photonics has been limited. The reason can be found in part in some intrinsic drawbacks of polymers (long term stability, layer uniformity and purity), in part in the last decades' restless developments in semiconductor technology. Nonetheless, recent advances in polymer science and the increasing requirements of the market in terms of costs and performance seem to make times mature for a technological breakthrough. Due to their structural flexibility, special optical properties, high optical quality, and unique processing and fabrication capabilities, polymers are now being increasingly used for a variety of optical applications including high density data storage, optical interconnects, displays, optical processing, electro-optic modulation and switching.

On the other hand, liquid crystals own a number of features that make them attractive well beyond the well-established display applications:

- transparency, both in the visible and in the near infra-red (NIR);
- a huge optical anisotropy, of the order of ~ 0.2, much larger than in conventional birefringent materials;
- capability to be driven by relatively weak electric fields (few Volts);

- integratability into other materials, like polymers, oxides, silicon, etc.;
- low cost;
- plenty of different composites and mesophases, permitting a fine tuning of the physical properties and the exploitation of many different effects;
- a mature technology, industrially well-known for its use in the fields of displays.

Until now liquid crystals have not been much used in the telecom field, mainly because of the significant scattering losses, the need for aligning and containing surfaces and the relatively low response times (milliseconds). However, as for polymers, the situation is rapidly evolving, and the first LC based photonic devices are already on the market. A further interest in liquid crystals comes from the possibility to be used in conjunction with polymers, in form of composite materials. In these systems the above mentioned LC drawbacks are circumvented or greatly reduced, while the most interesting properties of both polymers and liquid crystals are retained. The better-known LC-polymer composites are the so-called polymer dispersed liquid crystals (PDLCs), i.e. matrices of polymer embedding micrometric liquid crystal droplets. Due to the optical mismatch between the polymer and the LC droplets, these materials exhibit a strong light scattering; yet, the optical contrast, hence the amount of scattering, can be controlled by an external electric field till a transparent state is reached.

Most interestingly, PDLCs can be adopted as suitable media for holographic recording. In 1993 Sutherland et al. [2-3] first realized what they called holographic-PDLCs (H-PDLCs), i.e. holographic Bragg gratings recorded in LC-polymer composites. They found that a periodic structure, made of alternate polymer-rich and LC-rich layers, arises when a photosensitive LC-monomer mixture is cured with a laser interference pattern. This microscopic arrangement results in a volume phase grating, whose diffraction efficiency can be switched between a diffraction and a transmission state by applying an adequate voltage. H-PDLCs thus represent a simple, reliable, flexible, and effective technique to produce switchable and/or tunable diffraction Bragg gratings (DBGs). With minor geometrical changes, these elements can be the base for many photonic devices (switches, filters, multiplexers, cross connectors, lasers, etc.) of great importance in optical communication systems [4]. Furthermore, they have been proposed for many other interesting applications, like data storage, displays, holographic optical elements, sensors etc.

In order to be actually adopted in commercial devices, these materials must undergo an optimization process. Among the main requirements are high diffraction efficiency, angular selectivity, low losses, low driving voltages, and fast switching times; moreover, they should be able to work at the telecom wavelengths, typically in the NIR range. All these properties are directly connected with the structural features of the gratings, in particular with the type

of phase separation occurring between polymer and liquid crystal. On the other hand, the microscopic details of the grating morphology depend on a number of variable involved in the fabrication procedure, namely the components in the initial mixture, the exposure (intensity and duration), and the sample geometry. Understanding the deep connections among these three levels (production, morphology, macroscopic behavior) is the way to design devices with the best performance.

Taking this line, this work has been aimed to produce, test and optimize different kinds of LC-polymer DBGs, in view of their use as telecom photonic devices. In particular, interest has been focused on issues like modeling of H-PDLC gratings, H-PDLC anisotropy, characterization/extrapolation of the grating behavior at NIR wavelengths, comparison of H-PDLC and non-droplet gratings, influence of the LC-polymer interface on response times.

This thesis has been thus organized according to the following structure:

1. The first chapter provides an introduction to the physics of nematic liquid crystals, including continuum theory, static and dynamic electric properties, and optics of anisotropic media. The last section introduces some basic concepts on PDLCs, also useful for H-PDLCs.

2. The second chapter concerns the theory of holographic phase gratings, with special attention to the coupled wave theory for isotropic and anisotropic media. It provides the mathematical model to analyze data obtained from experimental measurements.

3. The third chapter describes the main experimental issues related to the realization of H-PDLC gratings, with focus on materials, preparation procedure, and morphology.

4. The forth chapter is a detailed discussion on the characterization measurements carried out on H-PDLC gratings, in particular the angular dependence of the diffraction efficiency.

5. The fifth chapter deals with the special features of non-droplet gratings (namely Policryps and Poliphem gratings). Series of measurements highlight the difference with traditional H-PDLCs and a careful analysis of the response times is carried out.

6. Finally, the sixth chapter explains how optical parameters of polymers and liquid crystals can be measured with high accuracy by variable angle ellipsometry and/or half-leaky guided mode method. Knowledge of these parameters is fundamental to get a full comprehension of soft material behavio and design efficient devices.

Chapter 1
Liquid crystals

1.1 Between liquids and crystals

Anisotropy is generally thought as an exclusive trait of crystalline materials, which exhibit different physical properties along the different lattice directions. It was 1888 when Friedrich Reinitzer first observed the existence of a new phase of matter, intermediate between the crystalline and the liquid phase. Nowadays, the substances showing such a peculiar phase are called *liquid crystals* (LCs), as they share features with both liquids (fluidity) and crystals (anisotropy).

The occurrence of a liquid crystalline phase in materials is connected with a large shape anisotropy of the constituent molecules. Indeed, a substance made up of isotropic (spherical) molecules can exhibit only two configurations: one spatially ordered (crystalline phase) and another one spatially disordered (isotropic liquid phase). Conversely, the spatial distribution of anisotropically shaped molecules involves both the positional and the orientational order. As a consequence, several intermediate phases (*mesophases*), characterized by high orientational order and a lower degree of positional order, are also possible (Fig. 1.1).

The most common of these mesophases, and the only one considered in this work, is the *nematic* phase. In this state the elongated molecules[1] possess no positional order at all, while are on average aligned along a preferred direction. Each mesophase occurs in a certain range of temperatures. The temperature corresponding to the nematic-isotropic transition is usually known as clearing point (T_{N-I}), as the material, cloudy in the nematic phase, becomes transparent when entering the isotropic phase. Common values for T_{N-I} are in the range $30 \div 90\,^{\circ}\mathrm{C}$.

1.2 Physics of nematics

1.2.1 The order parameter

In nematic liquid crystals, molecules can be represented as cylindrical rods almost parallel to each other. The local alignment direction can be represented by a unit vector

[1] Most types of liquid crystals consist of alongated, rod-shaped, organic molecules. However, liquid crystals made up of disc-, babana-, T-shaped, etc. molecules do also exist.

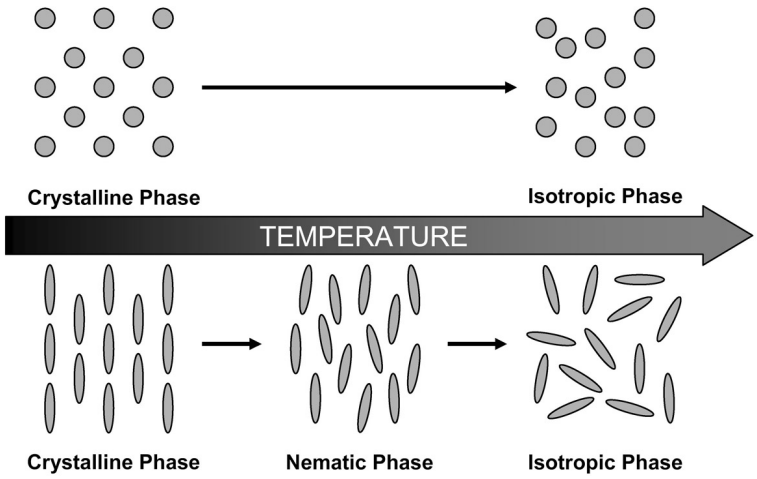

Figure 1.1: Phase transitions for a system of isotropic and anisotropic molecules.

$\hat{\mathbf{n}}$, known as the *molecular director*. In a reference system with the z-axis along $\hat{\mathbf{n}}$, the orientation of each molecule is described by the zenithal angle θ and the azimuthal angle φ. If we introduce the angular distribution function $f(\theta, \varphi)$, the probability of finding a molecule oriented in the solid angle $d\Omega$ is, by definition, $f(\theta, \varphi)d\Omega$. In order to describe correctly the nematic properties, $f(\theta, \varphi)$ has to respect two constraints:

1. $f(\theta, \varphi)$ has not to depend on φ, for the cylindrical symmetry around $\hat{\mathbf{n}}$ of the nematic phase;

2. $f(\theta) = f(\pi - \theta)$, for the equivalence of $\hat{\mathbf{n}}$ and $-\hat{\mathbf{n}}$ (i.e. on average as many molecules point up, as point down).

The molecule degree of alignment can be synthetically described by an order parameter S, defined as the average quadrupole moment[2]:

$$S = \frac{1}{2}\left\langle\left(3\cos^2\theta - 1\right)\right\rangle = \int f(\theta)\frac{1}{2}\left(3\cos^2\theta - 1\right)d\Omega. \tag{1.1}$$

With this definition one gets $S = 1$, when all the molecules are perfectly parallel to $\hat{\mathbf{n}}$, and $S = 0$, when the molecules are randomly oriented.

1.2.2 Continuum theory

In general $\hat{\mathbf{n}}$ is not spatially constant over the whole volume, because of the interaction with boundaries and external fields. In many circumstances significant variations of $\hat{n}$ occur

[2] The average dipole moment $\langle\cos\theta\rangle$ always vanishes, due to the second of the previous statements.

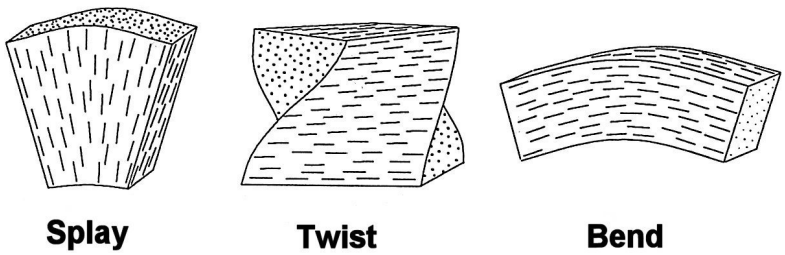

Figure 1.2: The three fundamental deformation modes of nematic liquid crystals.

over a distance ($\gtrsim 1\,\mu\mathrm{m}$) much longer than the molecular scale ($\sim 20\,\text{Å}$). In this case microscopic details can be neglected and the system can be treated according to the continuum theory.

For a LC sample at a fixed temperature T, the equilibrium director configuration $\hat{\mathbf{n}}(\mathbf{r})$ is found minimizing the free energy of the system under appropriate boundary conditions. The free energy per unit volume F_d can be derived through an expansion in powers of the director distortion. Without going into details (for a detailed analysis see Refs. [5-6]), one can just note that symmetry reasons (equivalence of $\hat{\mathbf{n}}$ and $-\hat{\mathbf{n}}$, invariance under rotations and inversions) lead us to discard linear terms in the gradient and write down the three-term quadratic expression

$$F_d = \frac{1}{2}k_1\left(\vec{\nabla}\cdot\hat{\mathbf{n}}\right)^2 + \frac{1}{2}k_2\left[\hat{\mathbf{n}}\cdot\left(\vec{\nabla}\times\hat{\mathbf{n}}\right)\right]^2 + \frac{1}{2}k_3\left[\hat{\mathbf{n}}\times\left(\vec{\nabla}\times\hat{\mathbf{n}}\right)\right]^2, \tag{1.2}$$

where the three elastic constants k_i are associated to the three fundamental modes of distortion (*splay*, *twist* and *bend*), represented in Fig. 1.2.

However, surface forces have also to be considered. Indeed, it is the type of interaction between the LC and the substrate that sets the alignment at the boundaries. Such alignment is then transferred to the whole sample by the bulk elastic forces. Mathematically this is expressed by appropriate boundary conditions for the director field (strong anchoring assumption).

The equilibrium condition is obtained by minimizing the total free energy with respect to variations of $\hat{\mathbf{n}}$ and its derivatives, under the constraint $|\hat{\mathbf{n}}|^2 = 1$. Using the method of Lagrange multipliers, the functional $\mathcal{F}$ to be minimized is:

$$\mathcal{F} = \int_V \left\{F_d(n_\alpha, \partial_\beta n_\alpha) - \lambda\,|\hat{\mathbf{n}}|^2\right\} d\mathbf{r}, \tag{1.3}$$

where λ is the Lagrange multiplier and the compact notation $\partial_\alpha = \frac{\partial}{\partial r_\alpha}$ has been used. Imposing the stationary condition with respect to small variations of the director components

n_α and their derivatives $\partial_\beta n_\alpha$ gives

$$\delta\mathcal{F} = \int_V \left\{ \frac{\partial F_d}{\partial n_\alpha}\delta n_\alpha + \sum_\beta \frac{\partial F_d}{\partial(\partial_\beta n_\alpha)}\delta(\partial_\beta n_\alpha) - 2\lambda n_\alpha \delta n_\alpha \right\} d\mathbf{r} = 0. \tag{1.4}$$

The second term in the integral can be evaluated by inverting the derivative with the variation, integrating by parts and letting the surface terms go to zero:

$$\begin{aligned} \int_V \frac{\partial F_d}{\partial(\partial_\beta n_\alpha)}\delta(\partial_\beta n_\alpha) d\mathbf{r} &= \int_V \frac{\partial F_d}{\partial(\partial_\beta n_\alpha)}\partial_\beta(\delta n_\alpha) d\mathbf{r} \\ &= \left.\frac{\partial F_d}{\partial(\partial_\beta n_\alpha)}\delta n_\alpha\right|_{\partial V} - \int_V \partial_\beta \left(\frac{\partial F_d}{\partial(\partial_\beta n_\alpha)}\right)\delta n_\alpha d\mathbf{r} \\ &= -\int_V \partial_\beta \left(\frac{\partial F_d}{\partial(\partial_\beta n_\alpha)}\right)\delta n_\alpha d\mathbf{r}. \end{aligned} \tag{1.5}$$

Hence we have

$$\delta\mathcal{F} = \int_V \delta n_\alpha \left\{ \frac{\partial F_d}{\partial n_\alpha} - \sum_\beta \partial_\beta \left(\frac{\partial F_d}{\partial(\partial_\beta n_\alpha)}\right) - 2\lambda n_\alpha \right\} d\mathbf{r} = 0. \tag{1.6}$$

This has to be true for any variation δn_α, so finally one obtains

$$\frac{\partial F_d}{\partial n_\alpha} - \sum_\beta \partial_\beta \left(\frac{\partial F_d}{\partial(\partial_\beta n_\alpha)}\right) = 2\lambda n_\alpha. \tag{1.7}$$

The quantities

$$h_\alpha = \frac{\partial F_d}{\partial n_\alpha} - \sum_\beta \partial_\beta \left(\frac{\partial F_d}{\partial(\partial_\beta n_\alpha)}\right) \tag{1.8}$$

can be considered as the components of a vector $\mathbf{h}$, called molecular field. In this way Eq. 1.7 simply states that the director $\hat{\mathbf{n}}$ at the equilibrium is point by point parallel to the molecular field $\mathbf{h}$. Equation 1.7 can also be interpreted in terms of torques. Being $\hat{\mathbf{n}}$ adimensional, the vector $\mathbf{h}$ has the dimensions of a force times a length divided by a volume. Therefore we can define the elastic distortion torque per unit volume

$$\boldsymbol{\tau}_d = \hat{\mathbf{n}} \times \mathbf{h}, \tag{1.9}$$

and recast the equilibrium condition in this simple form:

$$\boldsymbol{\tau}_d = \mathbf{0}. \tag{1.10}$$

1.2.3 External field effect

Let us now consider the effect of static external fields on nematic liquid crystals. In general, electric and magnetic fields induce a reorientation of the LC molecules, changing the bulk configuration of the molecular director. Instead, within the limits of the strong anchoring hypothesis, they do not affect the director alignment at the boundaries.

From an electromagnetic point of view, liquid crystals can be ideally regarded as diamagnetic dielectrics[3]. Their anisotropic features are expressed by the tensorial nature of the electric permittivity $\underline{\epsilon}$ and the magnetic permeability $\underline{\boldsymbol{\mu}}$. However, in almost all LC applications, including the ones discussed in this work, the electric effects are of much more practical interest than the magnetic ones. Therefore, the present analysis is limited to the case of electric fields (the treatment of magnetic fields follows the same lines).

Due to the nematic cylindrical symmetry around $\hat{\mathbf{n}}$, the permittivity tensor $\underline{\epsilon}$ can be written, in the laboratory frame, as

$$\epsilon_{ij} = \epsilon_{\perp}\delta_{ij} + (\epsilon_{\parallel} - \epsilon_{\perp})\, n_i n_j, \tag{1.11}$$

where $\epsilon_{\perp}$ and $\epsilon_{\parallel}$ are the values of permittivity measured respectively orthogonally and along the molecular director and n_i is the i-th components of $\hat{\mathbf{n}}$. Consequently, the constitutive equation becomes, in Gaussian units,

$$\mathbf{D} = \epsilon_{\perp}\mathbf{E} + \Delta\epsilon(\hat{\mathbf{n}} \cdot \mathbf{E})\hat{\mathbf{n}}, \tag{1.12}$$

with $\Delta\epsilon = \epsilon_{\parallel} - \epsilon_{\perp}$ representing the dielectric anisotropy.

From electromagnetism, the energy term to be added to the thermodynamic potential[4] is

$$F_E = -\frac{1}{4\pi}\int \mathbf{D} \cdot d\mathbf{E} = -\frac{\epsilon_{\perp}}{8\pi}E^2 - \frac{\Delta\epsilon}{8\pi}(\hat{\mathbf{n}} \cdot \mathbf{E})^2. \tag{1.13}$$

The first term is independent of reorientation. The second term is the interesting one: it favors parallel alignment if $\Delta\epsilon > 0$, and perpendicular alignment if $\Delta\epsilon < 0$.

Minimizing the total free energy, as in the previous section, leads to introduce an electric torque per unit volume $\boldsymbol{\tau}_{el}$

$$\boldsymbol{\tau}_{el} = \frac{\Delta\epsilon}{4\pi}(\hat{\mathbf{n}} \cdot \mathbf{E})(\hat{\mathbf{n}} \times \mathbf{E}), \tag{1.14}$$

and to express the equilibrium condition in presence of external electric fields as

$$\boldsymbol{\tau}_d + \boldsymbol{\tau}_{el} = \mathbf{0}. \tag{1.15}$$

1.2.4 Freédericksz effect

Let us consider a nematic liquid crystal with positive dielectric anisotropy ($\Delta\epsilon > 0$), which is the case most often encountered in practical applications. Be the LC placed between two aligning surfaces and be the electric field applied normally to the undistorted molecular director. The three basic geometries are shown in Fig. 1.3; they correspond respectively to a splay, twist and bend deformation[5]. In all the three cases, the torque exerted by the

[3] We are neglecting conduction effects.

[4] The potential used here is the one to be minimized for a fixed voltage applied to external electrods.

[5] In fact, while the second case corresponds to a pure twist, a splay deformation is always associated

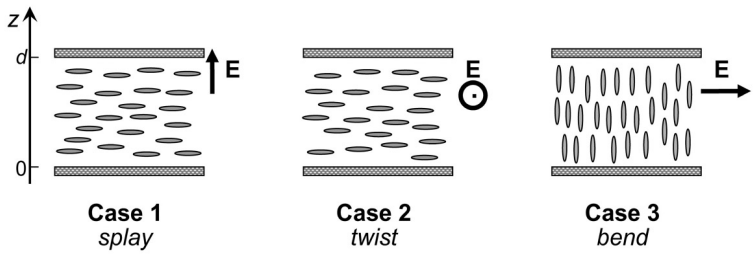

Figure 1.3: The three fundamental geometries encountered in Freédericksz effect.

electric field is null on the base of Eq. 1.14. In fact, if the electric field is strong enough to overcome the elastic torque, the small fluctuations of the director can be amplified by the electric field, resulting in a reorientation of $\hat{\mathbf{n}}$ along $\mathbf{E}$. The presence of a threshold E_0 in this reorientation process is known as *Freédericksz effect*: for $E < E_0$ no reorientation is observed; for $E > E_0$ reorientation begins, starting from the center of the sample, where the restoring torque exerted by the elastic forces is weaker.

The value of E_0 can be derived by a simple argument [5]. Let us consider the director configuration $\hat{\mathbf{n}}$ correspondent to a small perturbation $\delta\mathbf{n}$ of the undistorted configuration $\hat{\mathbf{n}}_0$

$$\hat{\mathbf{n}} = \hat{\mathbf{n}}_0 + \delta\mathbf{n}, \tag{1.16}$$

with $\delta\mathbf{n}$, orthogonal to $\hat{\mathbf{n}}_0$ and parallel to $\mathbf{E}$, only depends on z (where the z-axis is normal to the boundaries, as in Fig. 1.3). For this slightly distorted configuration, the elastic free energy density (Eq. 1.2) becomes

$$F_d = \frac{1}{2} k_i \left(\frac{\partial \delta\mathbf{n}}{\partial z} \right)^2, \tag{1.17}$$

where k_i represents the splay, twist or bend elastic constant according to the case considered, as shown in Fig. 1.3. Analogously the electric contribution to the free energy density (Eq. 1.13) becomes, apart from a factor independent of $\delta\mathbf{n}$,

$$F_E = -\frac{\Delta\epsilon}{8\pi} E^2 \delta\mathbf{n}^2. \tag{1.18}$$

Assuming strong anchoring at the boundaries, we have that $\delta\mathbf{n}$ must be null at $z = 0$ and $z = d$, where d is the sample thickness. Hence, we can expand $\delta\mathbf{n}$ in a Fourier series

$$\delta\mathbf{n} = \sum_{\nu=1}^{\infty} \delta n_\nu \sin \frac{\nu\pi z}{d}. \tag{1.19}$$

---

to a small bend deformation and vice versa.

Inserting this expression in the total free energy density $F_d + F_E$ and integrating over the thickness, one obtains (per unit surface)

$$\mathcal{F} = \frac{d}{4}\sum_{\nu=1}^{\infty}\delta n_\nu^2\left[k_i\left(\frac{\nu\pi}{d}\right)^2 - \frac{\Delta\epsilon}{4\pi}E^2\right]. \tag{1.20}$$

As the system moves towards a stable state, the free energy $\mathcal{F}$ describing the deformed state must be negative for some values δn_ν. The deformation mode that requires the weakest field to be induced is the one with $\nu = 1$; this mode can be excited by any electric field respecting the inequality

$$\frac{\Delta\epsilon}{4\pi}E^2 > k_i\left(\frac{\pi z}{d}\right)^2. \tag{1.21}$$

The minimum of such values is the sought threshold field

$$E_{0i} = \frac{\pi}{d}\sqrt{\frac{4\pi}{\Delta\epsilon}k_i}. \tag{1.22}$$

As expected the first deformation mode corresponds to a higher distortion in the center of the sample. For higher electric fields, higher modes are excited and the distortion moves closer to the boundaries.

It can be demonstrated that when the strong anchoring assumption is no more valid (weak surface anchoring), reorientation occurs even at the boundaries, while the threshold field decreases.

1.2.5 Reorientation dynamics

Of the three reorientation configurations represented in Fig. 1.3, the one interesting for the present work is the third one, i.e. the one corresponding to a bend distortion of a homeotropically aligned sample. Studying dynamics in this geometry requires some care, for two different reasons: first, bend distortion is always accompanied by a splay distortion (and vice versa); second, bend and splay distortions inevitably involve a flow process coupled with the director rotation (backflow effect)[6]. The latter effect could be taken into account by renormalizing the viscous coefficients, but this is beyond the scope of our work. Beckflow effect will thus be neglected.

In this assumption and for infinite anchoring energy, the equation of motion of the director is expressed through the balance of elastic, electric and viscous torques

$$\left(k_1\cos^2\theta + k_3\sin^2\theta\right)\frac{\partial^2\theta}{\partial z^2} + (k_3 - k_1)\sin\theta\cos\theta\left(\frac{\partial\theta}{\partial z}\right)^2 + \frac{\Delta\epsilon}{4\pi}E^2\sin\theta\cos\theta = \gamma_1\frac{\partial\theta}{\partial t}. \tag{1.23}$$

[6] Backflow effects are absent in the pure twist deformation. For this reason, this is the case more often studied in literature.

Here, z is a coordinate normal to the boundaries, θ is the angle between the director and the z-axis, γ_1 is the rotational viscosity; the inertial term ($I\frac{\partial^2\theta}{\partial t^2}$) has also been disregarded. In the one-constant ($k_1 \sim k_3$) and small angle approximations, a simplified expression is obtained

$$k_3\frac{\partial^2\theta}{\partial z^2} + \frac{\Delta\epsilon}{4\pi}E^2\left(\theta - \frac{2}{3}\theta^3\right) = \gamma_1\frac{\partial\theta}{\partial t}. \tag{1.24}$$

Given the boundary conditions $\theta(0) = \theta(d) = 0$, we can expand the solution in a Fourier series. For small reorientations, i.e. for electric fields just over the threshold, we can neglect higher harmonics and look for solutions in the form

$$\theta(z,t) \simeq \theta_m(t)\sin\frac{\pi z}{d}. \tag{1.25}$$

Substituting in Eq. 1.24, multiplying both sides by $\sin\frac{\pi z}{d}$ and integrating over the thickness d, one arrives at

$$\left(1 - \frac{E_0^2}{E^2}\right)\theta_m - \frac{1}{2}\theta_m^3 = \frac{4\pi\gamma_1}{\Delta\epsilon E^2}\frac{d\theta_m}{dt}, \tag{1.26}$$

where Eq. 1.22 has been used.

If the initial director configuration is undistorted (but still subjected to thermal fluctuations) and an electric field is applied at $t = 0$, the solution of Eq. 1.26 is

$$\theta_m^2(t) = \frac{\theta_m^2(\infty)}{1 + \left(\frac{\theta_m^2(\infty)}{\theta_m^2(0)} - 1\right)\exp\left(-\frac{2t}{\tau_E}\right)}, \tag{1.27}$$

where $\theta_m(\infty)$ represents the steady state value of θ_m, $\theta_m(0)$ is the amplitude of the initial director fluctuations and τ_E is the reorientation time constant under the influence of the electric field

$$\tau_E = \frac{\gamma_1}{\frac{\Delta\epsilon}{4\pi}E^2 - k_3\frac{\pi^2}{d^2}} = \frac{\gamma_1 d^2}{k_3\pi^2}\frac{1}{\left(\frac{E^2}{E_0^2} - 1\right)} = \frac{4\pi\gamma_1}{\Delta\epsilon\left(E^2 - E_0^2\right)}. \tag{1.28}$$

On the other hand, when the director, initially in some distorted configuration $\theta(z,0)$, reorients itself under the only action of the restoring elastic forces, putting $E = 0$ in Eq. 1.24 (term in θ^3 can also be neglected) leads to the solution

$$\theta(z,t) \simeq \theta_0\sin\frac{\pi z}{d}\exp\left(-\frac{t}{\tau_0}\right). \tag{1.29}$$

Here θ_0 is the maximum deformation angle in the initial director profile, while τ_0 is the restoring time constant

$$\tau_0 = \frac{\gamma_1 d^2}{k_3\pi^2}. \tag{1.30}$$

In the case of larger initial deformation, higher harmonics should be taken into account. However, the time constant corresponding to the n-th harmonic results to be

$$\tau_{0,n} = \frac{\gamma_1 d^2}{k_3 \pi^2 (2n+1)^2} = \frac{\tau_0}{(2n+1)^2}. \tag{1.31}$$

This means that higher order distortions decay much faster than the fundamental mode and can thus be disregarded after a relatively short time.

1.3 Optics of liquid crystals

The anisotropic nature of liquid crystals also reflects on their optical properties. Indeed, liquid crystals own a very large optical birefringence, of the order of ~ 0.2. The optical behavior of birefringent materials is summarized in this section. For a detailed analysis starting from the Maxwell's equations see for instance Ref. [7].

1. Let us consider the propagation of a monochromatic plane wave of frequency ω and wave vector $\mathbf{k} = \frac{\omega}{c} n \hat{\mathbf{k}}$, with n the refractive index of the medium and $\hat{\mathbf{k}}$ a unit vector normal to the wave front. Let the propagation medium be described by a dielectric permittivity tensor $\underline{\boldsymbol{\epsilon}}$[7],[8], such that the electric field $\mathbf{E}$ and the electric displacement field $\mathbf{D}$ are generally not parallel

$$\mathbf{D} = \underline{\boldsymbol{\epsilon}} \cdot \mathbf{E}. \tag{1.32}$$

   The first result arising from Maxwell's equations is that vectors $\mathbf{k}$, $\mathbf{D}$ and $\mathbf{H}$ (the magnetic field) are orthogonal to each others. A different tern of orthogonal vectors is given by $\mathbf{S}$, $\mathbf{E}$ and $\mathbf{H}$, where $\mathbf{S} \equiv \frac{c}{4\pi} (\mathbf{E} \times \mathbf{H})$ is the Poynting vector and c the light velocity in the vacuum. In other words, in anisotropic media the flux of energy, represented by $\mathbf{S}$, is not parallel to the wave vector $\mathbf{k}$. The angle formed by $\mathbf{S}$ and $\mathbf{k}$, or equivalently by $\mathbf{E}$ and $\mathbf{D}$, is known as walk-off angle.

2. The second fundamental result is that, fixed a direction of propagation, the wave equation in anisotropic media admits two solutions, characterized by different polarization and refractive index. Nematics exhibit cylindrical symmetry around the molecular director. Such materials are called uniaxial, and the axis of symmetry is called optical axis. In a reference system with the z-axis parallel to the optical axis ($\hat{\mathbf{n}}$ in the case of nematics)

---

[7] Dielectric permittivity depends on the frequency. Therefore, the tensor considered when studying the optical phenomena is different from the one considered when studying the effect of static or quasi-static electric fields.

[8] With regards to optics, magnetic properties can usually be neglected, i.e. it is always supposed $\mathbf{H} = \mathbf{B}$.

the permittivity tensor $\underline{\boldsymbol{\epsilon}}$ can always be written as

$$\underline{\boldsymbol{\epsilon}} = \begin{pmatrix} \epsilon_\perp & 0 & 0 \\ 0 & \epsilon_\perp & 0 \\ 0 & 0 & \epsilon_{\parallel} \end{pmatrix}. \tag{1.33}$$

It can be demonstrated that, when light propagates through an uniaxial material, experiences a refractive index given by

$$n_{eff}(\theta) = \frac{n_o n_e}{\sqrt{n_e^2 \sin^2\theta + n_o^2 \cos^2\theta}}, \tag{1.34}$$

where θ is the angle between the vector $\mathbf{D}$ and the optical axis. The quantity $n_o = \sqrt{\varepsilon_\perp}$ and $n_e = \sqrt{\varepsilon_{\parallel}}$ are called respectively ordinary and extraordinary refractive indices. The optical anisotropy, also known as birefringence, is defined as $\Delta n = n_e - n_o$ and for rod-like nematics is always positive.

1.4 Polymer dispersed liquid crystals

1.4.1 Introduction

Polymer Dispersed Liquid Crystals (PDLCs) consist in a dispersion of liquid crystal droplets embedded in a polymeric matrix. As they share many features with the related holographic-PDLCs, this section provides a brief overview on their morphological, optical and electro-optical properties. For a more thorough analysis a very good reference is [8].

1.4.2 Preparation and morphology

PDLCs are realized from a homogeneous mixture of a liquid crystal and fluid prepolymer. Polymerization can be obtained in different ways: thermally, by solvent evaporation or by optical curing, the latter being the method also used for holographic-PDLCs. As liquid crystal is very little soluble in polymer, polymerization produces the phase separation of LC and the formation of small nematic droplets. Droplet dimension is typically about a few microns, even though it can vary in the range $0.01 \div 20\,\mu\mathrm{m}$, depending on the material properties and the preparation procedure.

An important issue is the alignment of the LC director inside each droplet. The topic is quite complex and have been object of deep study. Many different configurations are possible, critically depending on the droplet dimension, on its ellipticity, and on the values of LC elastic constants. Some of the most common geometries are represented in Fig. 1.4:

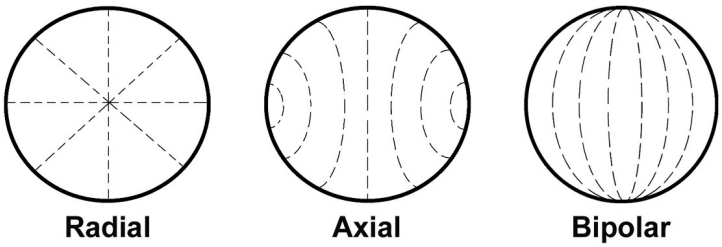

Figure 1.4: Three possible director configurations in liquid crystal droplets.

radial and axial ones correspond to normal anchoring to the surfaces, bipolar one to tangential anchoring.

The LC director alignment can be synthetically described by introducing a droplet director $\mathbf{N}_d$, representing the average orientation of the liquid crystal director $\hat{\mathbf{n}}$ in each droplet, and a droplet order parameter S_d, describing the geometrical fluctuations of $\hat{\mathbf{n}}$ with respect to $\mathbf{N}_d$ in the droplet volume V_d

$$S_d = \frac{1}{2} \left\langle 3 \left(\mathbf{N}_d \cdot \hat{\mathbf{n}} \right)^2 - 1 \right\rangle_{V_d} . \tag{1.35}$$

1.4.3 Optical properties

As the diameter of the LC droplets is comparable or larger than the light wavelength, PDLCs exhibit a strong light scattering and appear cloudy on visual inspection. The amount of scattered light is proportional to the index mismatch between the polymeric matrix and the droplets, which can be as high as 0.1, due to the high birefringence of the liquid crystal. When no electric field is applied, the droplets directors are randomly oriented, and the index mismatch changes from droplet to droplet depending on their orientation. In fact, droplets are optically anisotropic, with the optical axis given by the droplet director. Therefore one can introduce an extraordinary refractive index of the whole droplet, n_{ed}, defined as the average index experienced by a light wave polarized along $\mathbf{N}_d$ and travelling in a direction normal to it. Analogously, one can define a droplet ordinary refractive index n_{od}, defined as the average index experienced by a light wave travelling in a direction parallel to $\mathbf{N}_d$ and with any transversal polarization. These values depend in a complicated way on the droplet shape and on the liquid crystal alignment inside the droplet. Calculations can be worked out

in the case of spherical bipolar droplets, with the following results:

$$n_{ed}(S_d) = \frac{n_o n_e}{\sqrt{n_e^2 + \frac{1}{3}\left(n_o^2 - n_e^2\right)\left(2S_d + 1\right)}}, \tag{1.36a}$$

$$n_{od}(S_d) \simeq \frac{2}{\pi} n_o F\left(\frac{\pi}{2}, \frac{\sqrt{\frac{2}{3}\left(n_e^2 - n_o^2\right)\left(1 - S_d\right)}}{n_e}\right). \tag{1.36b}$$

In these equations n_o and n_e represent the ordinary and extraordinary LC refractive indices respectively, and F is the complete elliptic integral of the first kind, defined as

$$F\left(\frac{\pi}{2}, m\right) = \int_0^1 \frac{dx}{\sqrt{\left(1 - x^2\right)\left(1 - m^2 x^2\right)}}. \tag{1.37}$$

As expected, Eqs. **??** reduce to n_e and n_o for uniform director alignment along the droplet axis ($S_d \longrightarrow 1$).

1.4.4 Switching properties

When an electric field is applied, for instance by means of an external voltage, all the droplet directors tend to align themselves parallel to the field, provided the liquid crystal own a positive dielectric anisotropy. If the droplet ordinary refractive index is chosen to match the polymer refractive index, incident light experiences an optically homogeneous materials and no scattering is observed: PDLC becomes transparent.

Discussing the Freédericksz effect, it has been observed that the threshold field is proportional to d^{-1}; as a consequence, the voltage $V = Ed$ necessary to reorient an ordinary homogeneous liquid crystal cell does not depend on the cell thickness. This is not the case for PDLCs: in this materials the electric field E_0 needed to switch the sample is not inversely proportional to the sample thickness, but to the average radius of the droplet R. As for the droplet refractive indices, exact calculations involve assumptions on the droplet shape and the LC alignment. The model proposed by Wu et al.[9] predicts that, in the case of a quasi-ellipsoidal droplet with small radius of curvature, the reorientation of $\mathbf{N}_d$ under an applied electric field is described by the equation

$$\theta\left(E\right) = \frac{1}{2}\arctan\left(\frac{2u\sqrt{1 - u^2}}{2u^2 - 1 + \left(E/E_0\right)^2}\right), \tag{1.38}$$

in which θ is the angle between $\mathbf{E}$ and $\mathbf{N}_d$, E_0 is the critical field for switching, and $u = \cos\theta_0$ with θ_0 being the value of θ for $E = 0$. The critical field is inversely proportional to the length of the droplet major axis and increases as the droplet aspect ratio increases.

Chapter 2
Holographic gratings

2.1 Introduction and classification

Holography is a well-known technique for producing a tridimensional image of an object [10]. It is based on the following principle: let us consider two coherent beams, known as the *signal* (or *object*) and the *reference*; the signal is used to light the object to be reproduced and the resulting scattered radiation is made interfere with the reference; interference of the two beams generates a complex fringe pattern that is recorded on a photosensitive material. This special "photographic image" of the object is called *hologram* and contains all the amplitude and phase information carried by the scattered wave. Indeed, if the hologram is illuminated once again by the reference beam, diffraction occurs and the wavefront of the scattered signal is reconstructed beyond the hologram in both intensity and phase. In the simplest case the signal and the reference are both plane waves and the hologram is just a planar grating, with fringes orthogonal to the plane of incidence (Fig. 2.1).

Holographic gratings can be divided into different classes. A first distinction concerns the kind of modulation recorded into the photosensitive medium: gratings consisting in a spatially periodic variation of the refractive index are called *phase gratings*, whereas gratings realized by a periodic variation of the absorption coefficient are called *amplitude gratings*. Because the soft materials studied in this thesis are almost completely transparent, only phase gratings are analyzed; however, study of amplitude gratings is along the same line. The important difference is that phase gratings can reach a theoretical diffraction efficiency (DE) of 100%, whereas the limit for amplitude gratings is $\sim 7\%$ [10].

Gratings can be further classified according to geometrical factors: holograms whose thickness is small compared to the grating spacing are referred to as *thin gratings*; conversely, one talks of *thick* (or *volume*) *gratings* when the thickness is large in comparison with the fringe spacing. A rigorous quantitative definition of thin and thick gratings is discussed in Sec. 2.6. Thin grating properties are much like the ones of ordinary metal gratings, with many diffraction orders and a limited diffraction efficiency (no more than 34%). On the other hand, in volume gratings diffracted light is concentrated in only one diffracted order, with up to 100% efficiency.

A further distinction is possible considering the orientation of the fringe planes in respect to the grating boundaries. Two different configurations are possible: in *transmission* or in *reflection*, according to whether the incoming and the diffracted beams propagate on

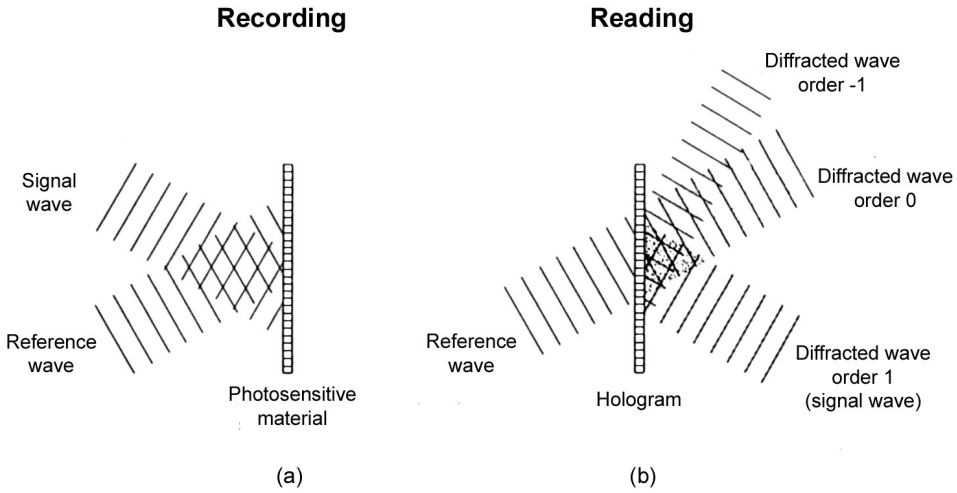

Figure 2.1: Holographic grating: recording (a) and reading (b).

the opposite or on the same side of the grating (Fig. 2.2). In particular, fringes parallel to the boundaries correspond to a reflection configuration, fringes perpendicular correspond to a transmission configuration; intermediate cases, with slanted fringes, can work in transmission as well as in reflection, depending on the angle of incidence.

Experimentally only transmission gratings were studied in this work, hence the focus of the chapter is on them; however, final results are given for reflection gratings as well.

2.2 Rigorous formulation of the diffraction problem

2.2.1 The Floque theorem and the Bragg condition

Light propagation and diffraction in dielectric gratings is a general problem of electromagnetism. It can be solved by different approaches, exact and approximate, numerical and analytical; a very good review on the topic is provided by Ref. [11]. Here the general problem is introduced in a rigorous way.

Figure 2.3 shows a generic planar dielectric grating, in a reference system with the z-axis chosen perpendicular to the grating boundaries, the x-axis in the plane of incidence and parallel to the medium boundaries and the y-axis perpendicular to the paper. The grating is always assumed of length d in the z-direction, infinite in the x- and y-directions. Fringe planes are orthogonal to the plane of incidence (xz-plane); the grating vector $\mathbf{K}$ is perpen-

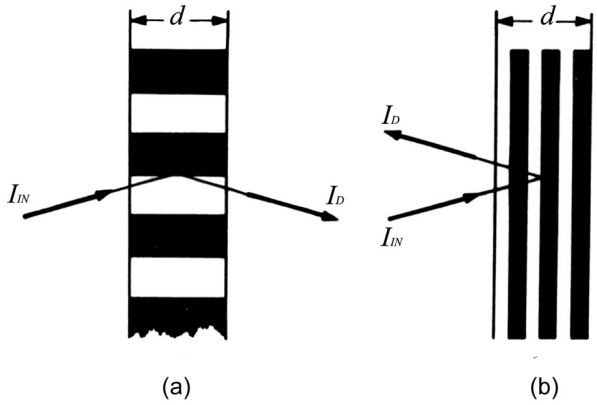

Figure 2.2: Schematic view of a transmission (a) and a reflection grating (b).

dicular to the fringe planes and makes an angle ψ with the z-axis; its module is $K = \frac{2\pi}{\Lambda}$, where Λ is the grating period.

The grating is assumed dielectric, non magnetic, completely lossless and isotropic; the case of anisotropic gratings is discussed later on. With regard to the light propagation, two different polarizations must be considered, in the plane of incidence (p-polarization) and normal to the plane of incidence (s-polarization). For the sake of simplicity, only the latter case is considered at this stage. Under this assumptions the wave equation describing the propagation through the grating has the following scalar form:

$$\nabla^2 E_y + k_0^2 \epsilon E_y = 0, \tag{2.1}$$

in which E_y is the y-component of the electric field, $k_0 = \frac{2\pi}{\lambda}$ is the light wavevector in the vacuum, and λ the light wavelength in the vacuum; $\epsilon = \epsilon(\mathbf{r})$ is a periodic function, of average value ϵ_0, describing the dielectric permittivity within the grating boundaries, i.e. for $0 \leq z \leq d$. Both $E_y(\mathbf{r})$ and $\epsilon(\mathbf{r})$ only depend on the x- and z-coordinates, as translational symmetry is assumed along y.

Let us consider a plane wave of wavevector $\mathbf{k}_i$ entering the grating at $z = 0$; $\mathbf{k}_i$ makes an angle θ_i with the z-axis, while its module is given by $k_0 n_0$, where $n_0 = \sqrt{\epsilon_0}$ is the medium average refractive index. Because the permittivity is periodically modulated, the incoming wave exchanges its energy with higher spatial harmonics growing in the grating while propagation takes place. Mathematically this idea is expressed by the Floquet theorem, which sets for the general solution of Eq. 2.1 the form

$$E_y(x,z) = \sum_{n=-\infty}^{\infty} A_n(z)\, e^{-i(\mathbf{k}_i + n\mathbf{K})\cdot\mathbf{r}} = \sum_{n=-\infty}^{\infty} A_n(z)\, e^{-i\mathbf{k}_n'\cdot\mathbf{r}}. \tag{2.2}$$

The electric field is hence a superposition of plane waves, whose amplitudes $A_n(z)$ change along z due to the energy exchange. By definition, when no modulation is present ($\epsilon(\mathbf{r}) =$

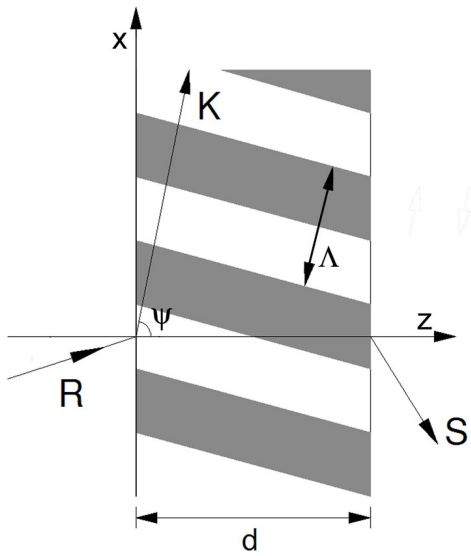

Figure 2.3: Schemtic representation of a slanted grating.

ϵ_0), only the zero-th wave propagates through the medium and solution is just $E_y(x,z) = A_0 e^{-i\mathbf{k}_i \cdot \mathbf{r}}$.

The wavevector of the n-th wave is given by

$$\mathbf{k}_n^{'} = \mathbf{k}_i + n\mathbf{K}, \tag{2.3}$$

with $\mathbf{k}_n^{'}$ having module $k_0 n_0$ and making an angle $\theta_n^{'}$ with the z-axis. One can express Eq. 2.3 in a graphical way, by observing that the three vectors form a close isosceles triangle, with $\mathbf{k}_i$ and $\mathbf{k}_n^{'}$ representing the sides of equal length. This vector configuration is possible only for certain values of θ_i, depending on the modules of $\mathbf{k}_i$ and $\mathbf{K}$, hence on the values of λ and Λ. Indeed, Eq. 2.3, considered component by component, becomes

$$k_0 n_0 \sin\theta_n^{'} = k_0 n_0 \sin\theta_i + n\frac{2\pi}{\Lambda}\sin\psi, \tag{2.4a}$$

$$k_0 n_0 \cos\theta_n^{'} = k_0 n_0 \cos\theta_i + n\frac{2\pi}{\Lambda}\cos\psi, \tag{2.4b}$$

along x- and z-direction respectively. These equations can be combined eliminating θ_n and give the well-known Bragg formula in its more general formulation

$$\cos(\theta_i - \psi) = n\frac{\lambda}{2\Lambda n_0}. \tag{2.5}$$

When θ_i and λ are chosen to satisfy the n-th order Bragg condition, the reference zero-order wave and the diffracted n-th wave are phase-matched and energy exchange is favored; consequently diffraction efficiency is generally maximized on the n-th diffracted order.

However, Bragg condition need not necessarily be satisfied exactly to observe some diffraction; the allowance depends upon $\mathbf{K}$ and d, or, in other words, on whether the grating is thin or thick. In fact, the Floquet condition stated by Eq. 2.3 is a consequence of the grating translational invariance, but this invariance is only approximate along the z-direction, due to the finite grating length. For this reason while Eq. 2.4a is always matched exactly, Eq. 2.4b often holds only approximately. In general, the longer is the grating, the stronger is the requirement of matching the Bragg condition. On the other hand, thin gratings exhibit diffraction even when Eq. 2.5 is far to be respected.

When detuning from the Bragg condition is considered, Eqs. 2.2 and 2.3 can be reformulated respectively as

$$E_y(x,z) = \sum_{n=-\infty}^{\infty} A_n(z)\, e^{-i(\mathbf{k}_i + n\mathbf{K} - \Delta\mathbf{k}_n)\cdot\mathbf{r}} = \sum_{n=-\infty}^{\infty} A_n(z)\, e^{-i\mathbf{k}_n\cdot\mathbf{r}} \tag{2.6}$$

and

$$\mathbf{k}_n = \mathbf{k}_i + n\mathbf{K} - \Delta\mathbf{k}_n, \tag{2.7}$$

where the displacement vector $\Delta\mathbf{k}_n$ is parallel to the z-axis for the considerations expressed above, and $\mathbf{k}_n$ has propagation direction θ_n and module always equal to $k_0 n_0$. Obviously, for $\Delta\mathbf{k}_n = \mathbf{0}$, the Bragg condition is respected and the previous expressions are obtained.

2.2.2 The system of coupled differential equations

In order to calculate diffraction efficiencies, the shape of the permittivity profile must be specified. As the permittivity modulation is assumed small in comparison to the average value ϵ_0, it is always possible to expand ϵ in Fourier series and retain only the first harmonic

$$\epsilon(\mathbf{r}) = \epsilon_0 + \epsilon_1 \cos \mathbf{K}\cdot\mathbf{r} = \epsilon_0 + \frac{\epsilon_1}{2}\left(e^{i\mathbf{K}\cdot\mathbf{r}} + e^{-i\mathbf{K}\cdot\mathbf{r}}\right). \tag{2.8}$$

Substituting Eqs. 2.6, 2.7, and 2.8 into Eq. 2.1 and performing the indicated differentiations gives

$$\begin{aligned}\sum_{n=-\infty}^{\infty} \Bigg\{ & \frac{d^2 A_n(z)}{dz^2} - i2k_{nz}\frac{dA_n(z)}{dz} \\ & + \frac{k_0^2\epsilon_1}{2}\left[A_{n-1}(z)\, e^{-i(\Delta\mathbf{k}_n - \Delta\mathbf{k}_{n-1})\cdot\mathbf{r}} + A_{n+1}(z)\, e^{-i(\Delta\mathbf{k}_n - \Delta\mathbf{k}_{n+1})\cdot\mathbf{r}}\right]\Bigg\} e^{-i\mathbf{k}_n\cdot\mathbf{r}} = 0,\end{aligned} \tag{2.9}$$

where $k_{nz} = k_0 n_0 \cos\theta_n$ is the z-component of $\mathbf{k}_n$. Each term in the series is a coefficient multiplied by an exponential. Since the exponentials are linearly independent, the coefficients must be individually equal to zero. This eventually gives the set of coupled-wave equations

$$\frac{d^2 A_n(z)}{dz^2} - i2k_{nz}\frac{dA_n(z)}{dz} + \frac{k_0^2\epsilon_1}{2}\left[A_{n-1}(z)\, e^{-i(\Delta\mathbf{k}_n - \Delta\mathbf{k}_{n-1})\cdot\mathbf{r}} + A_{n+1}(z)\, e^{-i(\Delta\mathbf{k}_n - \Delta\mathbf{k}_{n+1})\cdot\mathbf{r}}\right]. \tag{2.10}$$

By inspection, this is an infinite set of differential equations, representing the energy coupling between the i-th plane wave and the $i+1$-th and $i-1$-th space harmonics. The fact that only adjacent orders are coupled is a consequence of the pure cosinusoidal shape of the permittivity profile. Numerically solving this system of differential equations provides an exact solution to the problem of diffraction by dielectric gratings [11].

2.3 Diffraction from thin gratings

Thin gratings typically operate in a diffraction regime, known as Raman-Nath regime, in which:

1. many diffraction orders are excited;
2. diffraction efficiency is almost independent of the angle of incidence;
3. maximum diffraction efficiency is always limited to rather low values.

In fact, when the grating thickness is small if compared to the period, energy coupling, hence diffraction efficiency, does not strictly depend on the Bragg condition. As discussed above, in general only Eq. 2.4a holds exactly. However, since K is small (for Λ is large), displacements from the Bragg condition Δk_n are small as well. As a consequence one can make the approximation that $\Delta k_n = 0$ for every n; neglecting also the second derivatives, the rigorous system of equations 2.10 thus becomes

$$\left[\cos\theta_i + n\frac{\lambda}{\Lambda n_0}\cos\psi\right]\frac{dA_n(z)}{dz} + i\kappa\left[A_{n-1}(z) + A_{n+1}(z)\right] = 0, \tag{2.11}$$

where the coupling constant κ has been defined as

$$\kappa = \frac{\pi\epsilon_1}{2n_0\lambda} \tag{2.12}$$

and the relation $\cos\theta_n = \cos\theta_i + n\frac{\lambda}{\Lambda n_0}\cos\psi$, valid for $\Delta k_n = 0$, has been used.

In the important case of unslanted fringe transmission gratings ($\psi = \pi/2$), Eq. 2.11 takes the form of a recurrence relation satisfied by Bessel function. For boundary conditions $A_0(z) = 1$ and $A_n(z) = 0$ ($n \neq 0$) the solution is

$$A_n(z) = (-i)^n J_n\left[\frac{2\kappa z}{\cos\theta_i}\right], \tag{2.13}$$

where J_n is the Bessel function of the first kind of order n. By definition, diffraction efficiency of the n-th order is given by

$$\eta_n = \left|\frac{A_n(d)}{A_0(0)}\right|^2 = J_n^2\left[\frac{2\kappa d}{\cos\theta_i}\right]. \tag{2.14}$$

From the properties of the Bessel function, one has that diffraction efficiency in thin transmission phase gratings cannot exceed, for $n \neq 0$, the value of 0.339.

2.4 Diffraction from thick gratings

2.4.1 Kogelnik theory

Thick gratings typically exhibit only one diffracted order and a strong sensitivity to the angle of incidence; moreover very high diffraction efficiencies can easily be reached. This behavior is known as Bragg regime. Many approximate theories have been developed for this interesting case. The most widely applied is the Kogelnik theory [12], also known as two coupled-wave theory. It can be obtained directly from the rigorous system of Eq. 2.10 with the two following approximations:

1. considering only two coupled waves, namely the zero-th order A_R (the reference) and the first diffracted order A_S (the signal);
2. neglecting the second derivative, as the energy interchange between waves is assumed to be spatially slow.

This leads to two coupled-wave equations

$$i \cos\theta_R \frac{dA_R(z)}{dz} = \kappa A_S(z) e^{i\Delta k z}, \tag{2.15a}$$

$$i \cos\theta_S \frac{dA_S(z)}{dz} = \kappa A_R(z) e^{-i\Delta k z}, \tag{2.15b}$$

in which θ_R and θ_S are the angle of propagation of the reference and the signal respectively, κ is the coupling constant defined in Eq. 2.12, and Δk is the dephasing from the Bragg condition. By definition Δk is given by

$$k_0 n_0 \cos\theta_S + \Delta k = k_0 n_0 \cos\theta_R + K \cos\psi \tag{2.16}$$

and vanishes when θ_R and λ fulfill Eq. 2.5.

A general solution of the coupled-wave equations is

$$A_R(z) = r_1 e^{\gamma_1 z} + r_2 e^{\gamma_2 z}, \tag{2.17a}$$

$$A_S(z) = s_1 e^{\gamma_1 z} + s_2 e^{\gamma_2 z}, \tag{2.17b}$$

where r_i and s_i are constants which depend on the boundary conditions. For a transmission grating these are

$$A_S(0) = 0, \tag{2.18a}$$
$$A_R(0) = 1, \tag{2.18b}$$

and

$$\frac{dA_S}{dz}(0) = -i\frac{\kappa}{\cos\theta_S}, \tag{2.19a}$$
$$\frac{dA_R}{dz}(0) = 0. \tag{2.19b}$$

Using Eqs. 2.18a and 2.19a in Eq. 2.17b, it follows that

$$s_1 = -s_2 = -i\frac{\kappa}{\cos\theta_S\left(\gamma_1 - \gamma_2\right)}. \tag{2.20}$$

Equations 2.15a and 2.15b can be combined and give

$$\frac{d^2A_S(z)}{dz^2} + i\Delta k\frac{dA_S(z)}{dz} + \chi^2 A_S(z) = 0, \tag{2.21}$$

where $\chi^2 = \frac{\kappa^2}{\cos\theta_S\cos\theta_R}$. Using for $A_S(z)$ the solution provided by Eq. 2.17b, one obtains a quadratic expression for $\gamma_{1,2}$ with solutions

$$\gamma_{1,2} = -i\frac{\Delta k}{2} \pm i\sqrt{\chi^2 + \left(\frac{\Delta k}{2}\right)^2}. \tag{2.22}$$

Substituting Eqs. 2.20 and 1.3 in Eq. 2.17b leads to the complete expression for $A_S(z)$

$$A_S(z) = -i\sqrt{\frac{\cos\theta_R}{\cos\theta_S}}e^{-id\frac{\Delta k}{2}}\frac{\sin\sqrt{d^2\chi^2 + \left(d\frac{\Delta k}{2}\right)^2}}{\sqrt{1 + \left(\frac{\Delta k}{2\chi}\right)^2}}. \tag{2.23}$$

2.4.2 Diffraction efficiency for transmission gratings

Diffraction efficiency for transmission gratings is defined as

$$\eta = \frac{\cos\theta_S}{\cos\theta_R}\left|\frac{A_S(d)}{A_R(0)}\right|^2, \tag{2.24}$$

where the obliquity factors $\cos\theta_R$ and $\cos\theta_S$ indicate that it is only the power flow in the z-direction that must be considered. Inserting the solution provided by Eq. 2.23 eventually gives the final formula for the diffraction efficiency

$$\eta_s = \frac{\sin^2\sqrt{\nu_s^2 + \xi^2}}{1 + \frac{\xi^2}{\nu_s^2}}, \tag{2.25}$$

where the grating strength ν and the grating detuning ξ are defined respectively as

$$\nu_s = \frac{\kappa_s d}{\sqrt{\cos\theta_R \cos\theta_S}} = \frac{\pi\epsilon_1 d}{2n_0\lambda\sqrt{\cos\theta_R \cos\theta_S}} \tag{2.26}$$

and

$$\xi = \frac{\Delta k}{2} d. \tag{2.27}$$

In these expressions there is an s as subscript to remind that only s-polarization has been considered. In fact Kogelnik theory holds for p-polarization as well [12]. In this case a vectorial wave equation must be considered in place of Eq. 2.1

$$\nabla^2\mathbf{E} - \vec{\nabla}\left(\vec{\nabla}\cdot\mathbf{E}\right) + k_0^2\epsilon\mathbf{E} = 0. \tag{2.28}$$

Calculations similar to the ones described above lead to an expression for the diffraction efficiency formally identical to Eq. 2.25, provided that the coupling constant, and hence the grating strength, is redefined as

$$\kappa_p = \frac{\pi\epsilon_1 \cos\left(\theta_R - \theta_S\right)}{2n_0\lambda}. \tag{2.29}$$

Some important features of diffraction efficiency can be now outlined:

1. For $\xi = 0$ the Bragg condition is satisfied and Eq. 2.25 reduces to

$$\eta_{s,p} = \sin^2\nu_{s,p} = \sin^2\frac{\kappa_{s,p} d}{\sqrt{\cos\theta_R \cos\theta_S}}, \tag{2.30}$$

   which reaches the maximum value of 100% at $\nu = \pi/2$. For $0 \leq \nu \leq \pi/2$ the higher is ν, the higher is the diffraction efficiency; however for $\nu > \pi/2$, the so-called overmodulation regime, η decreases and increases with a cyclical behavior.

2. By the respective definitions, it follows that $\kappa_s \geq \kappa_p$; as a consequence it is always $\eta_s \geq \eta_p$, for the usual case in which $\nu \leq \pi/2$.

3. For $\xi \neq 0$ efficiency decreases; in normal regime ($\nu \leq \pi/2$), $\eta\left(\xi\right)$ exhibits a pronounced peak at $\xi = 0$ and a series of much smaller side lobes. The main peak full-width at half-amplitude $2\Delta\xi$is an important parameter for practical applications. It can be calculated either in terms of angular detuning $2\Delta\theta_i$ (angular bandwidth), or in terms of wavelength detuning $2\Delta\lambda$ (wavelength bandwidth) from the Bragg condition; for unslanted transmission ($\psi = \pi/2$) and reflection ($\psi = 0$) gratings it results

$$2\Delta\theta_i \simeq \frac{\Lambda}{d} \qquad (\psi = \pi/2), \tag{2.31a}$$

$$2\Delta\theta_i \simeq \frac{\Lambda}{d\tan\theta_{iB}} \qquad (\psi = 0), \tag{2.31b}$$

and

$$\frac{2\Delta\lambda}{\lambda_B} \simeq \frac{\Lambda}{d\tan\theta_{iB}} \qquad (\psi = \pi/2), \tag{2.32a}$$

$$\frac{2\Delta\lambda}{\lambda_B} \simeq \frac{\Lambda}{d} \qquad (\psi = 0). \tag{2.32b}$$

This means that the grating bandwidth is depends essentially on the ratio between period and thickness. When grating enters the overmodulation regime, the amplitude of the side lobes can exceed that one of the main peak and in general the previous approximate expressions are no more valid.

2.4.3 Diffraction efficiency for reflection gratings

Kogelnik theory can also describe thick reflection gratings [12]. With similar calculations diffraction efficiency is found to be

$$\eta_{s,p} = \left[1 + \frac{1 - \frac{\xi_r^2}{\nu_{s,pr}^2}}{\sinh^2\sqrt{\nu_{s,p}^2 - \xi^2}}\right]^{-1}. \tag{2.33}$$

For $\xi = 0$, η becomes

$$\eta_{s,p} = \tanh^2 \nu_{s,p}. \tag{2.34}$$

For the reflection geometry, ν is defined as in Eq. 2.26; the only difference is that $\cos\theta_S < 0$, so it must be replaced with $|\cos\theta_S|$.

2.5 Diffraction from thick anisotropic gratings

2.5.1 Montemezzani and Zgonik's theory

Kogelnik theory, even though approximated, is able to describe most practical situations. However, it fails in describing the properties of grating recorded in anisotropic materials, like the ones containing liquid crystal. An extension of the two coupled-wave theory to the anisotropic case has been developed by Montemezzani and Zgonik [13]. The basic assumptions of the theory are the same as the ones of Kogelnik's. As in the previous sections, the present discussion is limited to the case of pure phase gratings (no absorption).

An anisotropic grating is described by a dielectric permittivity tensor $\underline{\boldsymbol{\epsilon}}$

$$\underline{\boldsymbol{\epsilon}}(\mathbf{r}) = \underline{\boldsymbol{\epsilon}}_0 + \underline{\boldsymbol{\epsilon}}_1 \cos(\mathbf{K}\cdot\mathbf{r}) = \underline{\boldsymbol{\epsilon}}_0 + \frac{\underline{\boldsymbol{\epsilon}}_1}{2}\left(e^{i\mathbf{K}\cdot\mathbf{r}} + e^{-i\mathbf{K}\cdot\mathbf{r}}\right), \tag{2.35}$$

where $\underline{\boldsymbol{\epsilon}}_0$ is the average permittivity tensor and $\underline{\boldsymbol{\epsilon}}_1$ the permittivity modulation tensor.

Considering generic polarization, the wave equation for the electric field vector $\mathbf{E}$ is

$$\vec{\nabla} \times \left(\vec{\nabla} \times \mathbf{E}\right) - k_0^2 \underline{\boldsymbol{\epsilon}} \cdot \mathbf{E} = 0. \tag{2.36}$$

The basic approximation of a two coupled-wave theory is that the total electric field is the superposition of the two plane waves, the reference and the signal,

$$\mathbf{E}(\mathbf{r}, t) = \left[\mathbf{E}_R(\mathbf{r}) e^{+i\mathbf{k}_R \cdot \mathbf{r}} + \mathbf{E}_S(\mathbf{r}) e^{+i\mathbf{k}_S \cdot \mathbf{r}}\right] e^{-i\omega t} + c.c., \tag{2.37}$$

where $\mathbf{E}_R$ and $\mathbf{E}_S$ are the complex amplitudes of the two waves, and $\mathbf{k}_R$ and $\mathbf{k}_S$ the respective wavevectors. Substituting this expression in Eq. 2.36, the first term becomes:

$$\begin{aligned} \vec{\nabla} \times \left(\vec{\nabla} \times \mathbf{E}\right) &= e^{i\mathbf{k}_S \cdot \mathbf{r}} \left\{\vec{\nabla} \times \left(\vec{\nabla} \times \mathbf{E}_S\right) - i\left(\vec{\nabla} \times \mathbf{E}_S\right) \times \mathbf{k}_S \right. \\ &\left. + \vec{\nabla} \times (\mathbf{E}_S \times \mathbf{k}_S) - (\mathbf{E}_S \times \mathbf{E}_S) \times \mathbf{k}_S \right\} + e^{i\mathbf{k}_R \cdot \mathbf{r}} \{...\} \end{aligned} \tag{2.38}$$

where the second set of curly brackets contains analogous terms in $\mathbf{E}_R$ and $\mathbf{k}_R$. The first terms on the right-hand side of Eq. **??** contains only second-order derivatives and can be neglected in the slowly varying amplitude approximation, as done for Kogelnik theory.

Using the relationship

$$-\left[(\mathbf{E}_S \times \mathbf{k}_S) \times \mathbf{k}_S\right] e^{i\mathbf{k}_S \cdot \mathbf{r}} = k_0^2 \underline{\boldsymbol{\epsilon}}_0 \cdot \mathbf{E}_S e^{i\mathbf{k}_S \cdot \mathbf{r}}, \tag{2.39}$$

which describes the linear propagation of each wave in absence of modulation ($\underline{\boldsymbol{\epsilon}}(\mathbf{r}) = \underline{\boldsymbol{\epsilon}}_0$), Eq. 2.36 reduces to the two coupled-wave equations

$$\left(\vec{\nabla} \times \mathbf{E}_S\right) \times \mathbf{k}_S + \vec{\nabla} \times (\mathbf{E}_S \times \mathbf{k}_S) = i\frac{k_0^2}{2} \underline{\boldsymbol{\epsilon}}_1 \cdot \mathbf{E}_R e^{i\Delta\mathbf{k} \cdot \mathbf{r}}, \tag{2.40a}$$

$$\left(\vec{\nabla} \times \mathbf{E}_R\right) \times \mathbf{k}_R + \vec{\nabla} \times (\mathbf{E}_R \times \mathbf{k}_R) = i\frac{k_0^2}{2} \underline{\boldsymbol{\epsilon}}_1 \cdot \mathbf{E}_S e^{-i\Delta\mathbf{k} \cdot \mathbf{r}}. \tag{2.40b}$$

Here vector $\Delta\mathbf{k}$ is the dephasing from the Bragg condition and is defined as done in Sec. 2.2.1

$$\mathbf{k}_S = \mathbf{k}_R + n\mathbf{K} - \Delta\mathbf{k}. \tag{2.41}$$

Using some vector algebra, the left-hand sides of Eq. 2.40a can be rewritten as

$$\left(\vec{\nabla} \times \mathbf{E}_S\right) \times \mathbf{k}_S = k_S \left\{\left(\hat{\mathbf{k}}_S \cdot \vec{\nabla} E_S\right) \hat{\mathbf{e}}_S - \left(\hat{\mathbf{e}}_S \cdot \hat{\mathbf{k}}_S\right) \vec{\nabla} E_S\right\} \tag{2.42}$$

and

$$\vec{\nabla} \times (\mathbf{E}_S \times \mathbf{k}_S) = k_S \left\{\left(\hat{\mathbf{k}}_S \cdot \vec{\nabla} E_S\right) \hat{\mathbf{e}}_S - \left(\hat{\mathbf{e}}_S \cdot \vec{\nabla} E_S\right) \hat{\mathbf{k}}_S\right\}, \tag{2.43}$$

where $\hat{\mathbf{e}}_S$ and $\hat{\mathbf{k}}_S$ are real unit vectors along the electric field vector and the wavevector. Similar expressions hold for the wave field $\mathbf{E}_R$. Summing Eqs. 2.42 and 2.43 and multiplying both sides of Eq. 2.40a with the versor $\hat{\mathbf{e}}_S$, one obtains

$$2k_S \left\{\vec{\nabla} E_S \cdot \left[\hat{\mathbf{k}}_S - \left(\hat{\mathbf{e}}_S \cdot \hat{\mathbf{k}}_S\right) \hat{\mathbf{e}}_S\right]\right\} = i\frac{k_0^2}{2} \left(\hat{\mathbf{e}}_S^T \cdot \underline{\boldsymbol{\epsilon}}_1 \cdot \hat{\mathbf{e}}_R\right) E_R e^{i\Delta\mathbf{k} \cdot \mathbf{r}} \tag{2.44}$$

For what has been said in Sec. 1.3, the vector in square brackets is parallel to the energy propagation direction (Poynting vector) of the wave $\mathbf{E}_S$, thus one can write

$$\hat{\mathbf{k}}_S - \left(\hat{\mathbf{e}}_S \cdot \hat{\mathbf{k}}_S\right) \hat{\mathbf{e}}_S = g_S \hat{\mathbf{u}}_S, \tag{2.45}$$

with $\hat{\mathbf{u}}_S$ being the unit vector along the Poynting vector. Reminding that $\hat{\mathbf{k}}_S \cdot \hat{\mathbf{d}}_S = \hat{\mathbf{e}}_S \cdot \hat{\mathbf{u}}_S = 0$ and $\hat{\mathbf{k}}_S \cdot \hat{\mathbf{u}}_S = \hat{\mathbf{d}}_S \cdot \hat{\mathbf{e}}_S = \cos\beta_S$, with β_S walk-off angle, one gets $g_S = \hat{\mathbf{e}}_S \cdot \hat{\mathbf{d}}_S = \cos\beta_S$; here the versor $\hat{\mathbf{d}}_S$ is along the electric displacement vector. Introducing the average refractive indices n_S and n_R seen respectively by the signal and reference wave, with $k_{S/R} = k_0 n_{S/R}$, the coupled-wave Eqs. 2.40a and 2.40b are rewritten as

$$\vec{\nabla} E_S \cdot \hat{\mathbf{u}}_S = \frac{k_0}{4 n_S g_S} \left(\hat{\mathbf{e}}_S^T \cdot \underline{\boldsymbol{\epsilon}}_1 \cdot \hat{\mathbf{e}}_R\right) E_R e^{i\Delta\mathbf{k}\cdot\mathbf{r}}, \tag{2.46a}$$

$$\vec{\nabla} E_R \cdot \hat{\mathbf{u}}_R = \frac{k_0}{4 n_R g_R} \left(\hat{\mathbf{e}}_R^T \cdot \underline{\boldsymbol{\epsilon}}_1 \cdot \hat{\mathbf{e}}_S\right) E_S e^{-i\Delta\mathbf{k}\cdot\mathbf{r}}. \tag{2.46b}$$

These equations are equivalent to Eqs. 2.15a and 2.15b in the isotropic case. However it is important to notice that the coupling terms describe the projection of the amplitude gradients along the Poynting vector direction of the corresponding wave, and not along the wavevector direction as in the theory of Kogelnik. This happens because in anisotropic materials the wavevector is no more parallel to the Poynting vector.

2.5.2 Transmission gratings

Choosing a reference system as in Fig. 2.3, transmission geometry is characterized by the condition $\cos\theta_S \cos\theta_R > 0$, where $\theta_{S/R}$ is the energy propagation angle of the signal/reference wave, i.e. the angle that versor $\hat{\mathbf{u}}_{S/R}$ makes with the z-axis. To find the spatial evolution of the signal wave, E_R is extracted from Eq. 2.40a and inserted into Eq. 2.46b, leading to the second order differential equation

$$\left[\left(\vec{\nabla} \otimes \vec{\nabla}\right) E_S \cdot \hat{\mathbf{u}}_S\right] \cdot \hat{\mathbf{u}}_R - i \left(\vec{\nabla} E_S \cdot \hat{\mathbf{u}}_S\right) (\Delta\mathbf{k} \cdot \hat{\mathbf{u}}_R) + \frac{k_0^2 \mu^2}{16 n_S n_R g_S g_R} E_S = 0, \tag{2.47}$$

where μ is the coupling constant $\mu = \left(\hat{\mathbf{e}}_S^T \cdot \underline{\boldsymbol{\epsilon}}_1 \cdot \hat{\mathbf{e}}_R\right) = \left(\hat{\mathbf{e}}_R^T \cdot \underline{\boldsymbol{\epsilon}}_1 \cdot \hat{\mathbf{e}}_S\right)$. A general solution for the equation is

$$E_S(z) = E_{S1} e^{\gamma_1 z} + E_{S2} e^{\gamma_2 z}, \tag{2.48}$$

with boundary conditions that in the case of transmission gratings are given by

$$E_S(z = 0) = 0, \tag{2.49a}$$

$$E_R(z = 0) = 1. \tag{2.49b}$$

Substituting in Eq. 2.47 and using the fact that $\Delta\mathbf{k}\cdot\hat{\mathbf{u}}_R = \Delta k\cos\theta_R$, because $\Delta\mathbf{k}$ must be parallel to the z-axis of the grating, one obtains

$$\gamma_{1,2} = i\frac{\Delta k}{2} \pm i\sqrt{\left(\frac{\Delta k}{2}\right)^2 + \chi^2}, \tag{2.50}$$

which, apart from a conventional minus, is formally equal to Eq. 2.22. Here χ has been redefined as

$$\chi = \frac{\pi\mu}{2\lambda\sqrt{n_S n_R g_S g_R \cos\theta_S \cos_R}}. \tag{2.51}$$

The constants $E_{S1,2}$ are obtained by imposing the boundary conditions

$$E_{S1} = -E_{S2} = \frac{\pi\mu}{4\lambda n_S g_S \cos\theta_S\sqrt{\left(\frac{\Delta k}{2}\right)^2 + \chi^2}} e^{i\Delta k z} \tag{2.52}$$

and lead to write the signal wave amplitude as

$$E_S(z) = \frac{\pi\mu}{4\lambda n_S g_S \cos\theta_S\sqrt{\left(\frac{\Delta k}{2}\right)^2 + \chi^2}} e^{i\frac{\Delta k}{2}z}\left[e^{iz\sqrt{\left(\frac{\Delta k}{2}\right)^2+\chi^2}} - e^{-iz\sqrt{\left(\frac{\Delta k}{2}\right)^2+\chi^2}}\right]. \tag{2.53}$$

The grating diffraction efficiency is defined as the ratio of the output signal intensity to the incident reference intensity, that is

$$\eta = \frac{|E_S|^2 n_S g}{|E_{R0}|^2 n_R g_R}\left|\frac{\cos\theta_S}{\cos\theta_R}\right| \tag{2.54}$$

Here the factor $\frac{\cos\theta_S}{\cos\theta_R}$ is an obliquity term as in the isotropic case. Instead the term $\frac{n_S g_S}{n_R g_R}$ is typical of anisotropic gratings; it can be neglected only when treating isotropic gratings or in anisotropic materials in the case of a configuration fully symmetric with respect to the z-axis and the optical indicatrix. Hence it follows that

$$\eta = \frac{\sin^2\sqrt{v^2+\xi^2}}{1+\xi^2/v^2}, \tag{2.55}$$

where ν and ξ are defined as

$$\nu^2 = \frac{\pi^2\left(\hat{\mathbf{e}}_S^T\cdot\underline{\boldsymbol{\epsilon}}_1\cdot\hat{\mathbf{e}}_R\right)^2 d^2}{4n_S n_R g_S g_R\cos\theta_S\cos\theta_R}, \tag{2.56}$$

$$\xi^2 = \frac{\Delta k^2}{4}d^2. \tag{2.57}$$

2.5.3 Reflection gratings

Reflection gratings are defined by the conditions $\cos\theta_R > 0$ and $\cos\theta_S < 0$. The boundary conditions in this case are

$$E_S(z = d) = 0, \tag{2.58a}$$

$$E_R(z = 0) = 1. \tag{2.58b}$$

For the more interesting case of $\xi = 0$, diffraction efficiency, defined as in Eq. 2.54, results to be

$$\eta = \tanh^2 \sqrt{-\nu^2}, \tag{2.59}$$

where we used for ξ and ν the previous definitions (note that for reflection gratings ν^2 is negative).

2.6 Criteria for thin-thick grating classification

It has be seen that diffraction gratings exhibit very different properties depending on the relative values of period and thickness. The reason for this difference has been given in a qualitative way, considering the lack of ideal translational symmetry along the z-direction. As a matter of fact, there are quantitative criteria to tell thin and thick holograms [11]. Introduced the parameter

$$Q = \frac{2\pi\lambda d}{n_0 \Lambda^2 \cos\theta_i}, \tag{2.60}$$

with θ_i angle of incidence, it can be demonstrated that:

- a grating is in the Raman-Nath regime, i.e. its diffraction efficiency follows Eq. 2.14 within 1% error, if

  $$Q\nu \leq 1, \tag{2.61}$$

  with ν defined as in Eq. 2.26;

- a grating operates in the Bragg regime, i.e. its diffraction efficiency follows Eq. 2.25 within 1% error, if

  $$Q/2\nu \geq 10. \tag{2.62}$$

It is interesting to notice that the ratio $Q/2\nu$ is actually independent from the thickness d. For this reason, the terms "thin" and "thick" are often misleading. Finally, there is a range of Q and ν values such that gratings are neither in Raman-Nath, nor in Bragg regime. In this condition approximate theories are no longer useful, and instead a numerical rigorous approach must be used.

These criteria remain valid also for anisotropic gratings.

Chapter 3
Holographic gratings in LC-polymer composites

3.1 Introduction

Liquid crystal-polymer composites are suitable media for holographic recording. The first holographic LC-polymer gratings, better known as holographic-PDLCs (H-PDLCs), were realized by Sutherland et al. in 1993 [2-3]. H-PDLCs are produced by curing, under a laser interference pattern, an isotropic photosensitive liquid mixture of pre-polymeric material and liquid crystal. The result of the recording process is schematically represented in Fig. 3.1: layers of LC droplets embedded in a polymeric matrix, in correspondence of the dark fringes of the curing pattern; homogenous polymer slices, possibly containing a small amount of non phase separated LC, in correspondence of the bright fringes. Because of the difference in refractive index between the polymer and the randomly oriented droplets, the spatial modulation of the LC content produces a modulation in the average refractive index. The resulting optical phase grating can be easily switched off by applying an external voltage: droplet directors align themselves along the field and the refractive index modulation disappears, provided that the polymer is chosen to match the droplet ordinary refractive index.

As discussed in the thesis introduction, H-PDLCs are very attractive for many different optical applications. Their major reason of interest is evidently connected with the electrical (or even thermal) control of the diffractive properties. In addition, H-PDLCs can reach very high diffraction efficiencies (over 90%) and show relatively fast response times (few milliseconds or even less). Furthermore, the scattering losses are very low if compared to ordinary PDLCs. Indeed, the average dimension of LC droplets in H-PDLC gratings falls well into the submicron range (typically $\sim 100\,\mathrm{nm}$), whereas is about few microns in PDLCs. Finally, another appealing feature of H-PDLCs is their simple and flexible production technique: with a standard holographic set-up and a fast one-shot exposure both reflection and transmission gratings can be realized, with spacings varying from many microns down to few hundreds of nanometers. The materials used in the photo-sensitive mixture are cheap and well–known to the industry in a profusion of different varieties, permitting an accurate tailoring of all the main chemical and physical properties.

Recently, two new variants of H-PDLCs, characterized by a complete separation of the LC phase, have been independently developed. Umeton's group at the University of

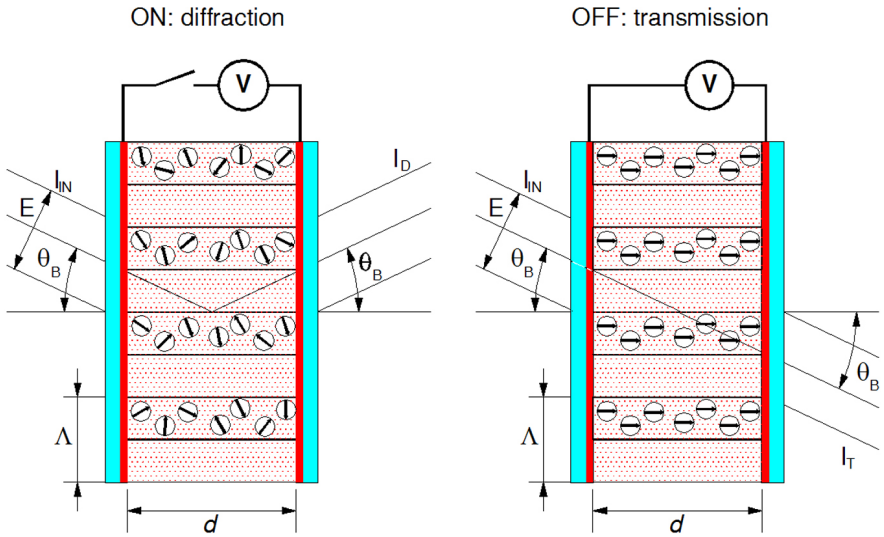

Figure 3.1: Schematic representation of H-PDLC transmission gratings.

Calabria (Cosenza, Italy) first patented what they called *Policryps* (polymer - liquid crystal - polymer slices) gratings [14]. Few years later Stumpe's group at the Fraunhofer Institute for Applied Polymer Research (Postdam, Germany) presented a patent for the somehow similar *Poliphem* (polymer - liquid crystal - polymer holograms electrically manageable) gratings [15]. In both types of gratings the droplet nucleation is inhibited so that their morphology simply consists of alternate homogeneous films of polymer and liquid crystal. This peculiar microscopic structure affects the grating macroscopic properties in many positive ways.

This chapter concerns the main issues related to the H-PDLC production: holographic set-up, materials, sample preparation, formation dynamics and morphology. Information provided comes from the experience developed during this work, complemented with several interesting published data; a very useful review on these topics is [16]. Information given for H-PDLCs are generally valid for all kinds of LC-polymer gratings. However, the specificities of Policryps and Poliphem are discussed in detail in the last two sections.

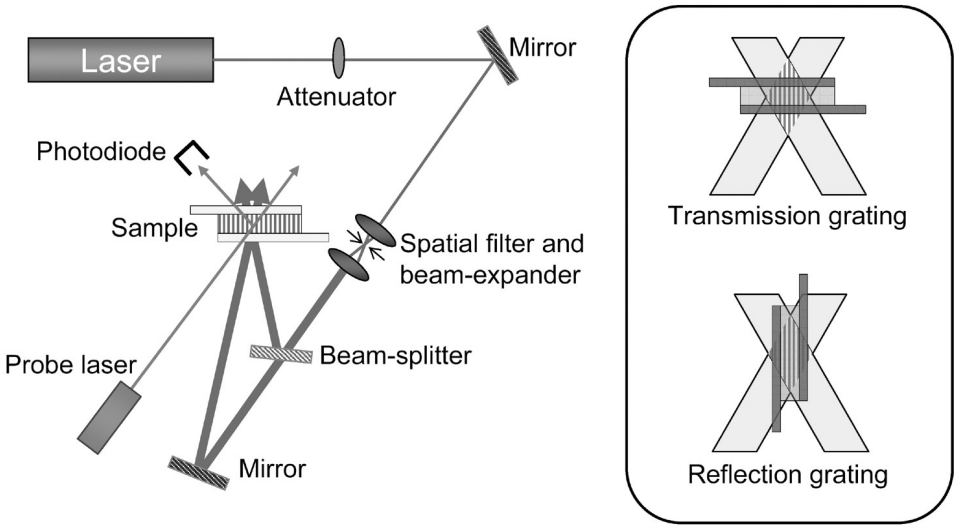

Figure 3.2: Holographic set-up for grating recording and real-time measurement of the diffraction efficiency (main picture). The grating geometry, in transmission or in reflection, is fixed by the sample orientation with respct to the interference pattern (inset).

3.2 Production procedure

3.2.1 Set-up

H-PDLC gratings are produced with a typical holographic apparatus; a general scheme is shown in Fig. 3.2. As in all holographic applications, the mechanical stability of the optical table and the absence of any source of vibrations are crucial, especially when working on small length scales (spacings $\lesssim 0.5\,\mu\mathrm{m}$). A laser is used as coherent light source; its wavelength must fall into the mixture sensitiveness region, typically in the ultraviolet (UV) or blue-green range. In most cases, the UV or visible lines of an Ar-ion laser (351, 476, 488, $514\,\mathrm{nm}$) or the second harmonic of a Nd:YAG laser ($532\,\mathrm{nm}$) are used. The first optical element is an attenuator (a neutral filter or a half-waveplate/polarizer combination), used to control the beam power. Subsequently, the beam is passed through a beam expander with an output diameter of a few centimeters. The beam edges are then cut off with an iris diaphragm, to get an almost uniform amplitude profile across an actual beam diameter typically ranging between some millimeters and one centimeter. The beam expander can be a simple telescope or rather a high precision spatial filter assembly, consisting of an objective lens, a pinhole, and a second collimating lens, so as to reduce the spatial noise and obtain a cleaner interference pattern.

Afterwards, a non polarizing beam-splitter divides the incoming light into two equal-power beams. By means of mirrors, the two branches are finally recombined over the sample, producing an interference pattern whose intensity profile (inside the sample) is

$$I = (I_1 + I_2)\left(1 + V\cos\frac{2\pi}{\Lambda}x\right), \tag{3.1}$$

in which I_1 and I_2 are the two beam intensities[9], V is the fringe contrast[10], given by

$$V = \frac{2\sqrt{I_1 I_2}}{I_1 + I_2}, \tag{3.2}$$

and Λ is the fringe spacing, as determined by the Bragg's law

$$\Lambda = \frac{\lambda_L}{2n_0 \sin\alpha/2}. \tag{3.3}$$

Here λ_L is the writing laser wavelength, n_0 is the mixture average refractive index and α is the angle formed by the interfering beams. As a matter of fact, the actual pitch of the resulting grating is shorter than the interference spacing. This reduction, usually of the order of few percent units, is caused by the polymer shrinkage during the polymerization.

With the same apparatus, both reflection and transmission gratings can be recorded, depending on the sample orientation with respect to the interference pattern (inset of Fig. 3.2).

3.2.2 Sample preparation

A typical H-PDLC sample consists in a small amount of photosensitive syrup, sandwiched between two ITO (indium tin oxide) coated glass slabs. If the syrup is fluid enough, it can be injected into the pre-assembled cell by capillarity; if necessary, operation can be done at an increased temperature. In general, the glass slabs do not undergo any special treatment, apart from an accurate cleaning; in particular, no alignment layer is used.

The grating thickness, usually in the range $5 \div 50\,\mu\mathrm{m}$, is set by MYLAR spacers placed at the sides of the cell or by silica spacers (sphere or fiber spacers) dispersed throughout the sample. Normally no glue is needed, because the polymerization itself provides the sealing. The two glass slabs are slightly staggered, in such a way that the ITO layers, which are on the inner faces of the cell, are accessible and can be used as electrodes (Fig. 3.3).

---

[9] Reflections at the air-sample interface must be considered. The sample itself is instead assumed transparent. If this is not the case, the interference pattern, hence the resulting grating, will not be uniform through the sample thickness.

[10] Actually, a perfect balance of the two beam intensities is not crucial, as the fringe contrast is not very sensitive (e.g. even for $I_2/I_1 = 0.5$ one obtains just $V = 0.94$).

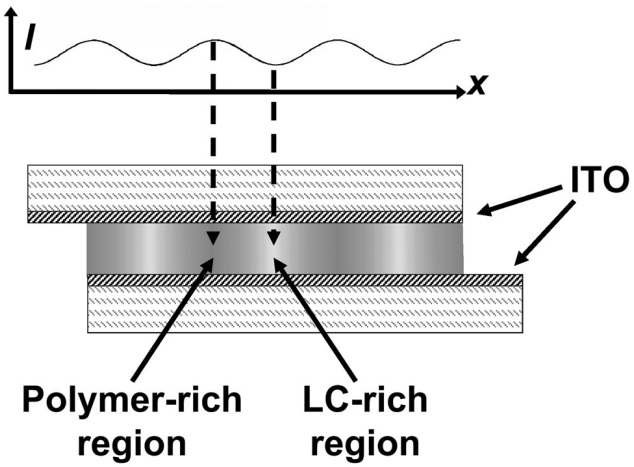

Figure 3.3: Typical H-PDLC sample (transmission configuration). When exposed to an interference pattern $I(x)$, phase separation occurs: at the end of the process polymer-rich regions are found in correspondence of the peaks of intensity, liquid crystal-rich regions in correspondence of the minima.

3.2.3 Exposure

The main parameters involved in the curing process are the writing beam intensity and the exposure time. Typical values are respectively $10 \div 100\,\mathrm{mW/cm^2}$ and $30\,\mathrm{s} \div 5\,\mathrm{min}$. However, a still wider variation is reported in literature depending on the adopted mixture; in general optimum values have to be found empirically. Usually a second laser, with low intensity and a wavelength well outside the monomer sensitiveness range, e.g. a He-Ne laser, is used to monitor the grating growth. The probe beam impinges on the sample at the correspondent Bragg angle and the power of the outgoing diffracted beam is measured by a photodiode. This real time measurement is important to stop the curing when the highest diffraction efficiency is reached; moreover it provides a great amount of information about the dynamics involved in the grating formation.

Finally, it is often useful that gratings undergo a post-writing blank exposure, in order to induce polymerization over the whole sample and ensure consumption of all unreacted monomer and photoinitiator molecules. Such treatment provides the sample a higher mechanical and electrical stability.

According to the method described above, H-PDLC recording appears straightforward. However, some care is needed to realize high quality gratings, particularly with regard to some issues.

- Mechanical stability. The polymer slices can collapse for the weakness of the polymer network. In other cases, the liquid crystal pours out from an apparently intact grating structure. Sometimes the reason is a poor adhesion of the polymer to the ITO coated glass surfaces; often the problem can be alleviated by the deposition of a polymer layer over the glass slabs. In general adopting different mixtures and /or curing parameters is the only way to get robust holograms.

- Electrical stability. Most H-PDLC gratings have to undergo high voltages (even over $20\ \mathrm{V}/\mu\mathrm{m}$) to be switched. Ionic impurities remained unreacted at the end of the curing process may diffuse under the effect of the electric field, heating the sample, short-circuiting the electrodes and eventually damaging the grating. Also in this case, an accurate choice of the syrup components can greatly reduce the problem. Of course, realizing gratings characterized by lower switching voltages remains the better solution.

- Resolution and grating quality. As a general rule, shorter is the grating pitch, greater is the influence of vibrations. With a good noise insulation, spacings as short as $100 \div 200\,\mathrm{nm}$ can be realized; further reductions are made difficult by the intrinsic molecular resolution of the polymer. Moreover, a vibration-free curing leads to neater separation between the polymer-rich and the LC-rich regions.

Overcoming these problems is mainly matter of experience. Once this empirical optimization work is done, gratings with high resolution, very good optical and electro-optical properties and long lifetimes can be readily obtained. In our experience, some well done gratings have kept working for more than one year with no significant change in their behavior.

3.3 Materials

A typical H-PDLC syrup contains the following components: monomer, liquid crystal, photoinitiator, and other optional additives, thoroughly mixed into a homogenous solution under darkroom conditions. The main features concerning the different components are now discussed.

3.3.1 Monomers

Monomers are the main component of H-PDLC mixtures, with a typical weight concentration of $30 \div 60\%$ (Tab. 3.1). Usually, multifunctional monomers that undergo a free-radical addition polymerization are used, because of their fast growth rate. A fast polymer-

Component	Typical concentration (w/w)
Monomer	$30 \div 60\%$
Liquid crystal	$30 \div 50\%$
Photoinitiator (+coinitiator)	$\lesssim 1 \div 2\%$
Reactive solvent	$5 \div 30\%$ (usu. 10%)
Surfactant	$5 \div 10\%$ (optional)

Table 3.1: Typical component concentrations in a H-PDLC mixture.

ization and a highly crosslinked network are important to get very small LC droplets (typically $\sim 100\,\mathrm{nm}$) and consequently a negligible light scattering. Two monomer parameters are particularly important in this regard: functionality, i.e. the number of C-C double bonds, and viscosity, which is related to the monomer molecular weight. The former affects the polymerization rate, the latter the monomer diffusion rate. The competition between these two processes is the key factor in determining the final grating morphology. Some studies on the monomer functionality [17-18, and references therein] have shown that the higher is the monomer functionality, the larger are the amount of phase separated LC, the average droplet size, and the anisotropy of the LC domains. Furthermore, monomer functionality affects the mechanical stability of gratings and the achievable limits of resolution.

Other important factors to be considered are: high miscibility with liquid crystal in the monomer state and poor miscibility in the polymer state, chemical inertness with liquid crystal, existence of suitable photoinitiators, good optical properties (transparency and refractive index), good adhesion to the substrates, elasticity (to improve the electro-optical properties), and mechanical stability.

Among monomers, the most widely used in H-PDLC applications is the dipentaerythritol hydroxy pentaacrylate (DPHPA). Its functionality is 5, as shown by its chemical structure reported in Fig. 3.4. Many other monomers in the acrylate family, or combinations of monomers, have also been tested; aliphatic urethane oligomers, characterized by a higher viscosity, have been used as well.

A different class of monomers are the commercially available Norland Optical Adhesives (NOA), photosensitive mixtures of polyfunctional thiols and allenes. These resins undergo a combination of free-radical addition and step-growth polymerization. Thus, they are characterized by a slower curing rate and generally need a high intensity exposure ($> 100\,\mathrm{mW/\,cm^2}$) in order to obtain small droplets. In addition, they are not much suitable for visible curing. These drawbacks have generally limited the use of these polymers as H-PDLC materials. However, NOA resins also own a number of interesting features (Tab. 3.2): they exhibit a reduced shrinkage, are much less viscous, have better adhesion and elastic properties (the latter is expected to reduce the switching voltage), and show a higher conversion efficiency (this means very few monomers remain unreacted at the end of the process). Recently, a mix-

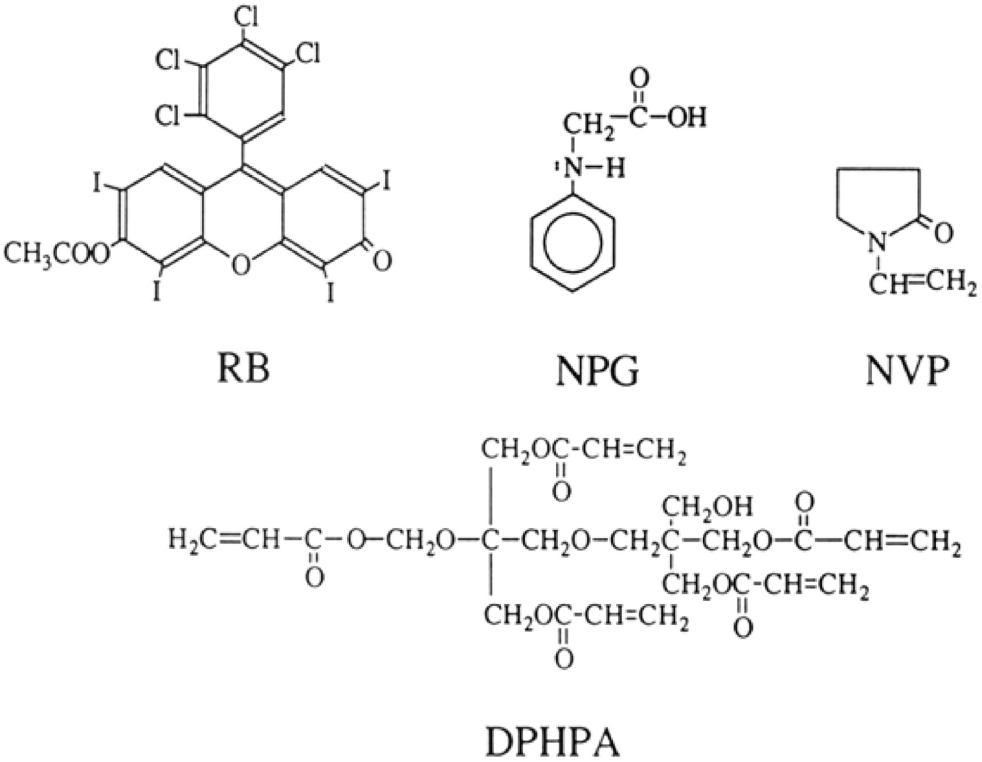

Figure 3.4: Chemical structures of four common H-PDLC components: initiator rose bengal (RB), coinitiator N-phenyl glycine (NPG), reactive diluent N-vinyl pyrrolidinone (NVP), monomer dipentaerythritol hydroxy pentaacrylate (DPHPA).

Name	Refractive index at $589\,\mathrm{nm}$	Viscosity at $25\,^{\circ}\mathrm{C}$ (cps)	Modulus of elasticity (psi)
NOA-61	1.56	300	150000
NOA-63	1.56	2000	240000
NOA-65	1.524	1200	20000
NOA-68	1.54	5000	20000

Table 3.2: Important physical property of most used Norland resins (from producer's datasheets).

ture of NOA-65, BL037 liquid crystal (30% w/w) and Irgacure 1173 UV initiator[11] (0.1% w/w) has been successfully exploited to produce reflection H-PDLC gratings [19]. Most interestingly, NOA resins are the monomer used to produce both types of non-droplet gratings: Policryps [20] and Poliphem [21].

3.3.2 Liquid crystals

Liquid crystals used in H-PDLC gratings are in large majority nematics liquid crystals[12], with a positive dielectric anisotropy. They enter the H-PDLC syrup in a $30 \div 50\%$ weight fraction (Tab. 3.1). The choice of the liquid crystal is connected with a number of chemical and physical parameters: miscibility in the monomer and immiscibility in the polymer; high dielectric anisotropy and low rotational viscosity, to obtain low switching voltages and fast response times; high birefringence, to get high refractive index modulation, hence high diffraction efficiency, and an ordinary refractive index matching the polymer refractive index, to achieve a good transmission state; finally, a wide nematic range, to guarantee a stability with temperature. In this regard, it must be considered that LC properties in composite materials can differ from the nominal ones, because of the impurities left by the curing process. Such impurities can considerably reduce the LC order parameter, thus lowering the grating optical contrast and shifting the clearing point to a lower temperature.

Two main families of nematic LCs, both provided by Merck, have been used in H-PDLCs: the first one, known as BL-series and including the very common E7 and 5CB, consists of mixtures of cyanobiphenyls and higher aromatic homologues; the second one, known as TL-series, are mixtures of chloro and fluoro substituted mesogens. The two families own different properties: BL-series LCs are very well miscible in acrylate and Norland monomers, but suffer from the presence of ionic impurities that can cause long term electric instability and high power consumption. Moreover, they are not suitable for UV curing, due to the strong absorption in that wavelength range. On the other hand, TL-series LCs

[11] NOA resins include a proprietary UV initiator. In the cited work, a supplementary initiator was added to increase the mixture sensitiveness.

[12] We just cite some work on holographic gratings based on cholesteric [22], smectic [23] and ferroelectric [24] liquid crystals.

are transparent in the UV, show better electrical properties, but have a limited solubility in monomers.

Interestingly, it has been observed that the two LC families give rise to a different droplet morphology: TL-series LCs show a tendency to form droplets aligned in the grating plane, whereas BL-series LCs tend to favor a homeotropic alignment with respect the grating plane [25]. The reason for this different behavior is still not well understood.

The chemical structure of 5CB and the composition of E7 are shown in Tab. 3.3.

Chemical structure	Weight [%]
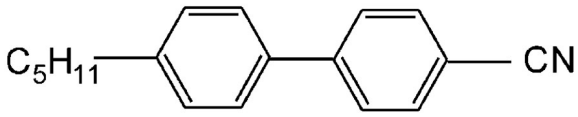	51
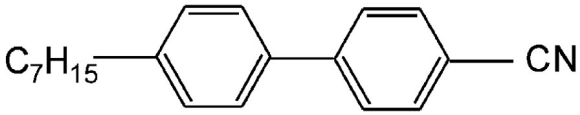	25
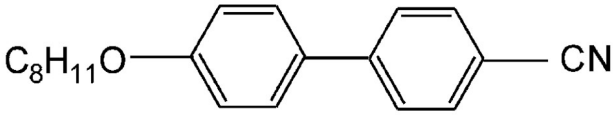	16
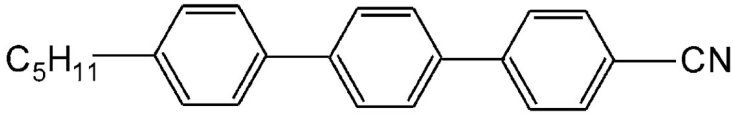	8

Table 3.3: E7 chemical composition. E7 liquid crystal is a well defined mixture of cyanobiphenyls and cyanoterphenyls, in the indicated proportions. Note that the first compound in the list is just the 5CB liquid crystal.

3.3.3 Photoinitiators

In order for the polymerization reaction to take place, monomers need to react with free radicals. Photoinitiators (PIs) are molecules producing free radicals when exposed to light. Usually a small amount, $\lesssim 1 \div 2\%$ by weight (Tab. 3.1), is enough to trigger the polymerization reaction. Two main mechanisms are possible: one, in which photon absorption induces the split of the PI molecule into two free radical molecules, and another one, which also involves a coinitiator (CI) molecule. In this case, the photoinitiator, excited by photon absorption, reacts with the coinitiator, which is an electron donor; the reaction results in the CI radical production.

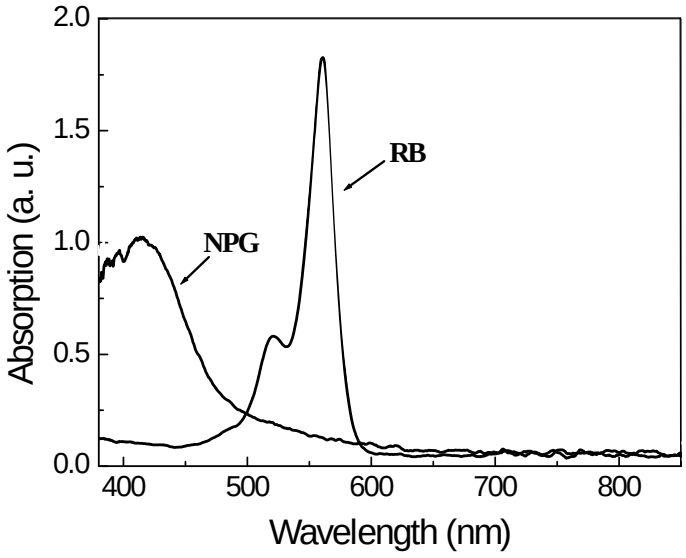

Figure 3.5: Rose bengal (RB) and N-phenyl glycine (NPG) absorption spectra.

A good photoinitiator must show high absorption at a suitable laser wavelength. Usually, two main wavelength ranges are used, one in the UV and another one in the blue-green region of the visible spectrum. UV curing ($250 \div 400\,\mathrm{nm}$) is widely used in photoinduced polymerization reactions. A large class of different compounds exists (e.g. Darocur and Irgacur families by Ciba), usually characterized by a high conversion efficiency. Many commercial resins, like Norland ones, do also include a specific, generally unknown, UV photoinitiator.

In the case of visible curing, the most common initiator system is the PI-CI combination of rose bengal (RB) and N-phenyl glycine (NPG). The respective chemical structures are shown in Fig. 3.4; Figure 3.5 shows their absorption spectra. In particular, rose bengal shows a strong absorption peak around $550\,\mathrm{nm}$, well suitable for green light laser curing (both $514\,\mathrm{nm}$ Ar-ion laser line and $532\,\mathrm{nm}$ Nd:YAG second harmonic have been widely used).

Recently, H-PDLC gratings have been realized with NIR diode and Ti-sapphire laser radiation ($800 \div 850\,\mathrm{nm}$), using as photoinitiator a commercially available cyanine dye, IR-140, in combination with etyl-dimethyl-amino benzoate [26-27].

3.3.4 Reactive diluent

In almost all acrylate-based H-PDLC recipes, N-vinyl pyrrolidinone (NVP) is added to the mixture as reactive diluent, usually in a 10% weight fraction (Fig. 3.4 and Tab. 3.1). NVP is needed to decrease the monomer viscosity and obtain a homogeneous mixture with

liquid crystal and photoinitiator. However, NVP is a mono-functional monomer, even though characterized by a low reactivity, so can play a role in the polymerization process, terminating the free-radical addition reaction and limiting the size of the polymer chains. Moreover, because of its high affinity for oxygen, increasing the NVP concentration can result in reducing the inhibition effect of oxygen, thus enhancing the gelation rate. Even if its role is still not fully understood, it has been found experimentally that an increased amount of NVP produces smaller and more isotropic droplets, thus reducing the scattering losses [28-29].

3.3.5 Surfactants

In H-PDLCs the average dimension of LC droplets is usually done as small as possible ($\sim 100\,\mathrm{nm}$) in order to reduce the light scattering. In reflection gratings the droplet dimension is also limited by the small spacing required to get the reflection band in the visible range (e.g. a notch wavelength of $600\,\mathrm{nm}$ implies a grating pitch of $\sim 200\,\mathrm{nm}$, when normal reflection and a 1.5 average refractive index is considered). The drawback is that the smaller are the LC domains, the larger is the field needed to reorient the droplet director and switch the grating off.

Experimentally, the addition of surfactants to the photosensitive mixture has proved to significantly reduce the switching field (up to 75% lower) in both transmission [30] and reflection gratings [31]. Non reactive long chain aliphatic acids, namely octoanoic acid, are typically added at this purpose in a 10% weight concentration (Tab. 3.1). These molecules operate at the polymer-LC interface and reduce the surface anchoring of the nematic droplets. It has been observed [31] that the presence of surfactants also affects the grating morphology, by delaying the onset of the phase separation process and thus reducing the average droplet dimension. However, these non reactive additives also contaminates the LC droplets, lowering the clearing point and potentially giving rise to unwanted conduction processes through the sample.

3.4 Formation dynamics

The mechanisms involved in the grating formation have been widely investigated, as they are directly connected with the grating morphology and, hence, with the final optical and electro-optical properties of H-PDLCs. The main experimental approach to the problem is the real-time measurement of the diffraction efficiency during the curing, as described in Sec. 3.2.3 [32-34]. In general, a growth in the diffraction efficiency corresponds to a growth of the refractive index modulation, indicating the appearance of a diffraction grating. On the theoretical side, the complex formation dynamics have been variously modeled with systems of differential equations linking the spatially anisotropic polymerization to the

monomer and LC diffusion [35-39]. The details of these experimental and theoretical works are beyond the scope of this thesis, even because the results obtained are often different, depending on the systems under analysis (materials, curing intensity, grating spacing, etc.) or on the mechanisms considered (e.g. it is still debated whether thermal gratings could play a role in the grating formation). Even though a full comprehension of the process is still far to be reached, a brief and general account on the topic is necessary to better understand the relations between curing parameters and morphology, as well as the difference between ordinary H-PDLCs and non-droplet gratings.

In general, the real-time measurement of the diffraction efficiency shows the following three-stage structure:

1. The first stage consists in a short inhibition period, in which the exposure does not produce any refractive index modulation, so that no increase in the diffraction efficiency is observed. This behavior is connected with the presence in the mixture of inhibitors, like oxygen or other molecules introduced by the monomer producer to avoid the unintentional onset of polymerization.

2. When all the inhibitors have reacted, the polymerization begins and a measurable diffraction efficiency is experienced. With the polymerization going on, the diffraction efficiency grows, usually (but not always) in a monotonic way. The complex microscopic process underlying this stage is described below.

3. Under a prolonged exposure, the diffraction efficiency reaches a steady state or start to decrease. This reduction can be due to the onset of strong scattering losses, as the LC droplet dimension becomes comparable to the light wavelength; in other cases the effect can be explained with an excessive refractive index modulation, drawing the grating to the overmodulation regime ($\nu > \pi/2$).

An important difference must be underlined between the dynamics involved in the PDLC and H-PDLC formation. In the former case, the LC droplet nucleation, driven by a floodlit (isotropic) exposure, is a stochastic process that takes place throughout the cell. The situation is different when the anisotropic H-PDLC curing is considered. In this kind of systems the polymerization begins and proceeds faster in the highly irradiated regions (bright regions). Consequently, in proximity of those areas the local concentration of monomers decreases, due to the monomer consumption, while the local LC concentration increases, due to the LC molecules expelled by the polymer network. As a result, a monomer diffusion from the dark to the bright areas and a LC counter-diffusion in the opposite direction occur. Obviously, the diffusion/counter-diffusion rates decrease as the polymer network is growing, until the polymer gelation prevents any further diffusion and fix a configuration in which polymer rich regions (in the bright areas) are separated by LC rich regions (in the dark

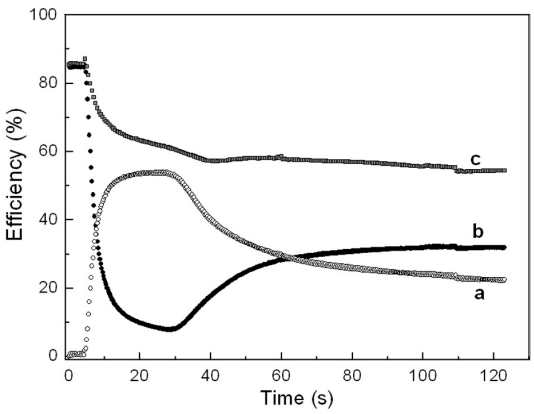

Figure 3.6: Real time formation curves: diffracted beam (a), transmitted beam (b), and sum of diffracted and transmitted (c). Measured power is normalized with respect to the incident beam power.

areas), as shown in Fig. 3.3. Here the high local concentration of LC and the low solubility of the LC in the polymer cause the liquid crystal to phase separate in the form of nematic droplets.

The moment in which the phase separation occurs can vary from sample to sample, according to the materials (PI concentration, monomer functionality, amount of liquid crystal) and the curing process (exposure intensity, grating spacing). Often first an isotropic concentration grating appears, and only later the droplet formation gives rise to a two-phase grating. Controlling the onset of the phase separation is crucial to determine the final morphology of the grating, as we will see discussing non-droplet gratings.

This dynamics can be illustrated by the graph in Fig. 3.6, taken from a sample similar to the ones described in Chapter 4 [40]: curves a and b represent respectively the power of the diffracted and transmitted beam, expressed as percentage of the impinging beam power; curve c is the sum of the two other curves and represents the total power beyond the grating, thus measuring the scattering losses. Different stages can be observed in curve a: first a $\sim 5\,\mathrm{s}$ inhibition period, then a fast growth of the diffraction efficiency, a plateau, and finally a decrease until a steady state is reached. Analysis of curve c clearly indicates that in such sample the light scattering begins just at the end of the inhibition; this clearly indicates that droplet nucleation and growth occurs from the earliest stages of the curing process, and thus is not responsible for the final decrease of the diffraction efficiency. This can be rather connected with the grating overmodulation. Indeed, the high curing intensity used in this case ($425\,\mathrm{mW/\,cm^2}$), can be responsible for a strong phase separation, formation of large droplets with consequent high amount of scattering and the same time high optical modulation.

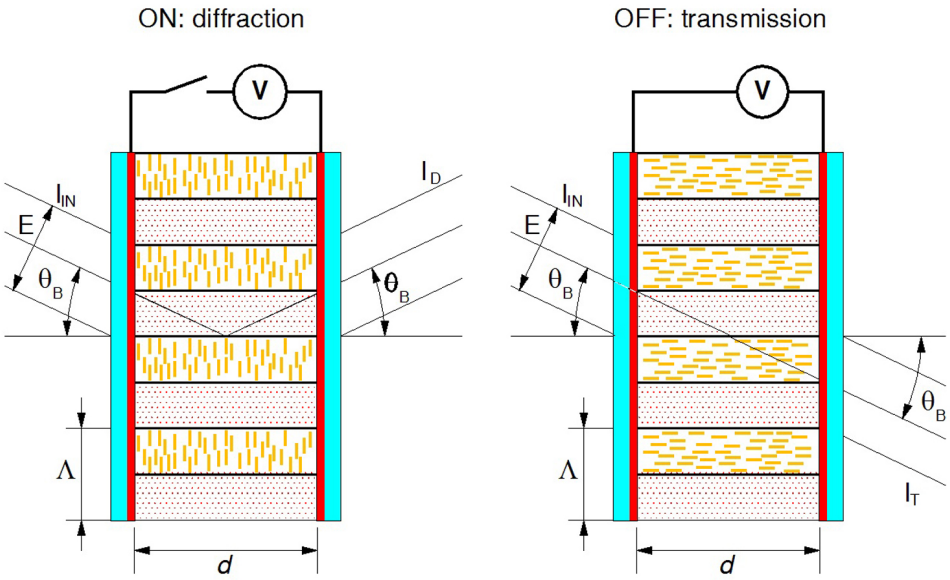

Figure 3.7: Schematic representation of non-droplet transmission gratings (Policryps and Poliphem). Notice that actually LC layers are often thinner than polymer layers.

3.5 Non-droplet gratings: Policryps and Poliphem

3.5.1 A new class of LC-polymer gratings

As explained in the previous sections, usually a great effort is made to get LC droplets as small as possible, so reducing the scattering losses. Unfortunately, the smaller is the droplet radius, the higher is the electric field necessary to reorient the droplet director. This problem can be partially overcome by adding surfactants to the photosensitive syrup. However, surfactants have other drawbacks, as they diminish the order parameter and cause conduction through the cell, thus mining the sample long term stability.

The approach proposed by Umeton's [14] and Stumpe's [15] groups is somehow opposite: they developed two new types of LC-polymer gratings (respectively called Policryps and Poliphem), in which the formation of LC droplets is completely avoided. Even though Policryps and Poliphem are realized according to different patented procedures, they share the same peculiar morphology: a periodic stack of homogeneous LC films and polymer layers, sharply separated from each other, as schematically shown in Fig. 5. Such non-droplet structure affects the grating properties in many positive ways:

- the scattering losses are strongly reduced, due to the absence of incoherent reflections, in both transmission and diffraction state;

- switching voltage is much lower, as the dimension of the LC domains is not fixed by the droplet size but by the grating spacing;
- higher refractive index modulations are achievable, hence higher diffraction efficiencies can be obtained with the same grating thickness.

The only drawback of these gratings is that their behavior is strongly dependent on the light polarization. As a matter of fact, they only work with p-polarized light. This can be well understood observing the picture in Fig. 5. For reasons that are still not well clear, LC molecules align themselves orthogonally to the polymer slices, unless an electric field is applied across the cell. Because the polymer and the LC ordinary and extraordinary refractive indices (respectively n_p, n_o, and n_e) are chosen in such a way that $n_p \approx n_o < n_e$, incident p-polarized light experiences an index modulation and is thus diffracted. When an electric field is applied, LC director rotates, still remaining in the plane of incidence; eventually, for a certain angle, the effective LC refractive index (Eq. 1.34) experienced by p-polarized light matches the polymer index and diffraction is no more observed. Conversely, an s-polarized beam does not experience any index modulation across the cell, both with and without electric field.

Even if Policryps and Poliphem are microscopically very similar, they are prepared with different techniques. They are described in the following sections, while the experimental analysis of the two kinds of gratings is subject the subject of a dedicated chapter.

3.5.2 Policryps

The basic idea behind Policryps gratings is to prevent the formation of the namatic phase during the curing process. This result is accomplished by heating the sample over the nematic-isotropic transition temperature, while the curing takes place. Indeed, the diffusion of liquid crystal molecules is much easier when they are in the isotropic phase; as a consequence an almost complete redistribution of LC and monomer can be obtained. At the end of the process, the grating is slowly cooled down to the room temperature under thermostabilized conditions (typical cooling rate $-0.2\,^{\circ}\mathrm{C}/\,\mathrm{min}$). When the sample enter the nematic range, the slow cooling permits a complete and uniform alignment of the liquid crystal director along a single direction and, as a consequence, the production of a highly ordered structure [14, 20].

The special features of these high-temperature curing are evident in Fig. 3.8. There, a Policryps observed under a polarizing optical microscope is compared with a standard H-PDLC grating with the same spacing and prepared by the same materials: the difference in sharpness and resolution is striking. Microscope observation of gratings between crossed polarizers also provides a direct verification of the LC alignment inside the sample.

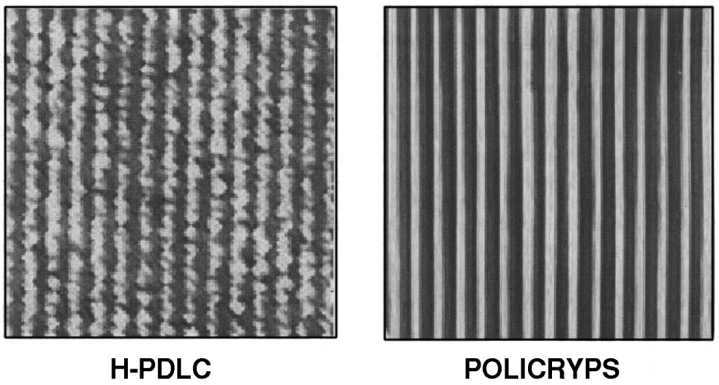

Figure 3.8: H-PDLC and Policryps morphologies with the same spatial period, as observed under a polarizing optical microscope.

Policryps gratings are realized with Norland resins, in particular NOA-61 and NOA-65 (Tab. 3.2), mainly in combination with 5CB liquid crystal in 30% weight concentration; no other additive is added to the mixture. Besides the high curing temperature, probably Norland resins also play a role in determining the Policryps special morphology. Indeed, due to the NOA delayed gelation point, LC molecules are not constrained in small droplets, but can coalesce to form large regular mono-domains.

Samples are UV cured at $351\,\mathrm{nm}$ (Ar-ion laser), with a typical exposure of $\sim 10\,\mathrm{mW/\,cm^2}$ for about $15\,\mathrm{min}$. The curing temperature is $\sim 50\,^\circ\mathrm{C}$, well above the 5CB clearing point ($35\,^\circ\mathrm{C}$)[20]. With this technique Policryps transmission gratings with spacing as small as $\sim 0.2\,\mu\mathrm{m}$ have been obtained (with optimum vibration insulation). On the other hand, Policryps in reflection configuration have still not been obtained, mainly for problems connected with the grating shrinkage. However, research is under way and new mixtures and geometries are being tested; of particular interest is the realization of Policryps gratings integrated in planar waveguides, in order to realize different kind of photonic devices. A switch of this kind has been designed during these years of activity and is now in the final stage of production.

3.5.3 Poliphem

In contrast to Polymer gratings, Poliphem are cured at room temperature. Here the special mono-domain morphology is the result of an accurate and specific choice of curing regime and syrup components [15, 21]. The photosensitive mixture is somehow similar to the one used for Polycrips. In this case a different representative of the Norland family is used (NOA-68), again in combination with 5CB liquid crystal in a $35 \div 40\%$ weight concentration; in addition, a small amount ($\sim 0.1\%$ w/w) of UV photoinitiator (Irgacure 369 by Ciba) is

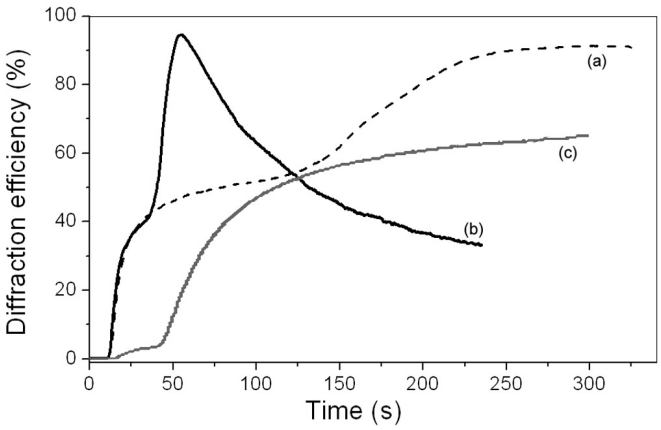

Figure 3.9: Real time formation curves in Poliphem gratings for different curing intensities: $40\,\mathrm{mW/\,cm^2}$ (a), $100\,\mathrm{mW/\,cm^2}$ (b), and $250\,\mathrm{mW/\,cm^2}$ (c).

added to increase the mixture sensitiveness. As for Policryps, the use of the NOA resins seems decisive to obtain a non-droplet morphology.

Sample is cured with the an Ar-ion laser emitting at $364\,\mathrm{nm}$; typical exposures are in the range $20 \div 100\,\mathrm{mW/\,cm^2}$ for $100 \div 300\,\mathrm{s}$. Curing regime is hence faster than for Policryps. Until now only transmission gratings have been realized, with spacings as small as $0.28\,\mu\mathrm{m}$.

Even if Policryps and Poliphem are prepared with two different methods, the production principle is fundamentally the same: to prevent phase separation until diffusion is completed. This can be well understood observing the formation curves of Poliphem gratings recorded at different curing intensities (in the range $40 \div 250\,\mathrm{mW/\,cm^2}$). In the range of intensities $40 \div 80\,\mathrm{mW/\,cm^2}$ (curve a in Fig. 3.9), the formation kinetics is characterized by a two-stage behavior: the first stage is a slow growth of the diffraction efficiency up to reaching an intermediate saturation value ($\sim 40\%$), after $30 \div 40\,\mathrm{s}$ from the start of irradiation; the second stage is characterized by a fast rise of the diffraction efficiency up to the maximum stationary value ($\sim 93\%$). For intensities of $80 \div 140\,\mathrm{mW/\,cm^2}$ (curve b), kinetics shows a three stage behavior: the first two stages are similar to the ones mentioned above, with a reduced time scale; the third stage shows a fall-down of the diffraction efficiency from $\sim 98\%$ to $\sim 30\%$, indicating a grating over-modulation. This means that, even if diffraction efficiency is decreasing, the grating optical modulation is actually increasing.

These characteristic curves can be related to different moments in the grating formation. The first stage is connected with the photopolymerization of monomers in correspondence of bright fringes of the interference pattern. This results in the development of a "density grating", due to the contrast in refractive indices between monomer and polymer

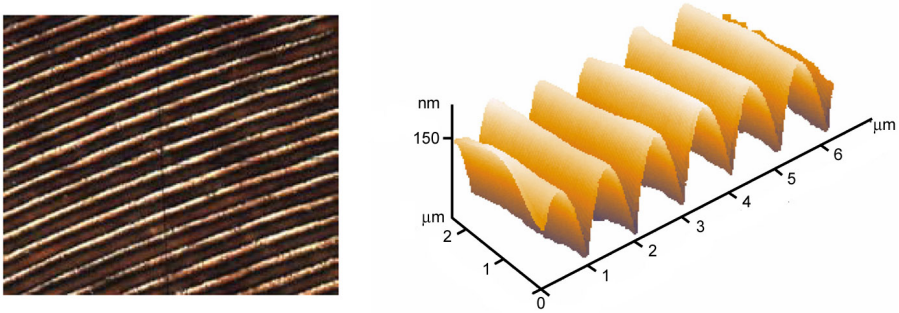

(a) (b)

Figure 3.10: Poliphem gratings observed at polarizing optical microscope (a) and atomic force microscope (b).

($n_{polymer} - n_{monomer} \approx 0.02$), and of a "concentration grating", due to the partial redistribution of the LC between the fringes ($n_{isotropic-LC} - n_{polymer} \approx 0.06$). The second stage, instead, can be explained by the phase separation and the nematic ordering of the liquid crystal in the LC-rich regions (dark fringes of the interference pattern). This gives rise to a large increase of the grating modulation ($n_{LC} - n_{polymer} \approx 0.2$ in the ideal case), and thus of the diffraction efficiency. Therefore, also for Poliphem the passage to a nematic ordered phase is delayed up to the end of the diffusion process.

This feature can be obtained only in a certain range of intensities. Indeed, a further increase of the recording intensity leads to the formation of typical H-PDLC gratings, characterized by low anisotropy, strong light scattering and lower diffraction efficiency. Curve c in Fig. 3.9 has been obtained for a $250\,\mathrm{mW/\,cm^2}$ exposure. In this case the first stage is depressed to a value of efficiency below 10%, whereas DE does not exceed 60% in the second stage. This behavior is probably caused by the fast polymerization, which hinders LC diffusion from the bright to the dark areas.

The evidence of the Poliphem non-droplet morphology is provided by different investigations. First of all, Poliphem gratings appear highly transparent on visual inspection, more than usual H-PDLCs. The highly ordered alignment of liquid crystal is evident when the sample is observed between crossed polarizer, as shown in Fig. 3.10a for a Poliphem-derived switchable Fresnel lens. This is also confirmed by the fact that Poliphem gratings are unable to diffract s-polarized light, just like Policryps. Finally, the grating structure has been also analyzed by atomic force microscope (AFM), as shown in Fig. 3.10b for a grating with spacing $1.1\,\mu\mathrm{m}$. From the image the sharpness of the non-droplet morphology is evident, even if the depth of the grooves appears much less than expected due to the limited resolution of the AFM tip.

Chapter 4
H-PDLC gratings: characterization and modeling

4.1 Introduction

The first part of the work of thesis has been dedicated to characterizing and modeling H-PDLC transmission gratings. The work has mainly consisted in measuring diffraction efficiency (DE) for visible and NIR wavelengths, at different incidence angles and applied electric fields; obtained data have been interpreted in the frame of an original morphological model. Most experimental data reported in this chapter are found in [41].

Different samples have been studied; most of them were realized in the laboratories of the Polythecnic University of Marche by Simoni's group, in the frame of an Italian National Research Project [42]. All samples shared the same composition (DPHPA and E7 liquid crystal) and the same recording technique (visible curing), and exhibited a very similar and reproducible behavior. However, for the sake of clarity, the experimental data reported in the next sections all refer to the same sample, prepared according to the following recipe: monomer DPHPA (39.8% w/w), liquid crystal E7 (40% w/w), reactive diluent NVP (20% w/w), photoinitiator RB plus coinitiator NPG (0.2% w/w). The cells containing the samples were assembled using ITO coated glass slabs, separated by Mylar spacers (thickness $23\,\mu\mathrm{m}$), and were filled by capillarity at a fixed temperature of $65\,^{\circ}\mathrm{C}$.

The photosensitive mixture was cured at a wavelength $\lambda = 0.514\,\mu\mathrm{m}$ (Ar-ion laser); the exposure time was fixed at $10\,\mathrm{min}$ and the laser intensity at $357\,\mathrm{mW/\,cm^2}$ per beam, with a spot diameter of $6\,\mathrm{mm}$. The interference angle was chosen to get a grating spacing $\Lambda = 1.72\,\mu\mathrm{m}$ and fringes orthogonal to the cell substrates. In the LC rich regions we expect droplets with average size in the range $100 \div 200\,\mathrm{nm}$, according to previous SEM analyses performed by us in samples of the same mixture. For this composition and curing conditions the droplet size is expected to be in the range $100 \div 200\,\mathrm{nm}$, according to observations reported in literature [17, 43].

4.2 Angular measurements

4.2.1 Experimental

The measurement of the diffraction efficiency at different incidence directions around the Bragg angle is interesting in many respects. First of all, angular selectivity is an important parameter for practical applications where multiplexing is required; also, it provides an indirect but easier way to measure the wavelength selectivity (wavelength and angular selectivities are related to each other, as explained in Sec. 2.4.2). Moreover, data fitting of angular curves is a powerful method to measure simultaneously two important parameters of gratings, namely the refractive index modulation and the thickness. Indeed, these two quantities are always coupled in determining the diffraction efficiency (cf. Eq. 2.26) and a single measurement at the Bragg angle does not allow one to separate the two contributions; this is instead possible by an angular fit, as the angular bandwidth is strictly dependent on the sole thickness.

Angular analysis was performed at both light polarizations and at different wavelengths: $0.532\,\mu\mathrm{m}$ (Nd:YAG laser second harmonic), $0.633\,\mu\mathrm{m}$ (He-Ne laser), $1.064\,\mu\mathrm{m}$ (Nd:YAG laser) and $1.55\,\mu\mathrm{m}$ (DFB diode laser). The sample temperature was held constant at $25.0 \pm 0.1\,^{\circ}\mathrm{C}$ via a suitable computer controlled hot stage. The external incidence angle was controlled by a motorized rotational stage, with accuracy of $0.01\,^{\circ}$. In the following, diffraction efficiency is defined as the ratio between the diffracted beam intensity and the sum of the transmitted and diffracted light intensities. In this way, one can ignore all the effects related to the losses for reflection, scattering, and absorption, the latter being very small for visible light but becoming more important in the NIR, due to the presence of ITO in the substrates. In most cases, gratings operate in a typical Bragg diffraction regime, with just one diffracted beam and negligible amount of light diffracted in higher orders. Some relevant anomalous behavior was observed and is discussed later on.

Dotted lines in Fig. 4.1 show the angular curves for s-polarization (four wavelengths) and p-polarization (only NIR wavelengths). As expected, these curves are peaked in correspondence of the wavelength dependent Bragg angle, according to Eq. 2.5. The measured values of the Bragg angle indicate a grating pitch $\Lambda = 1.61\,\mu\mathrm{m}$. This is slightly smaller than the spacing of the recording interference pattern ($1.72\,\mu\mathrm{m}$), due to the polymer shrinkage during the curing process. A small slant ($\psi \sim 0.3\,^{\circ}$) in the grating fringes was also revealed by comparing the angular positions of positive and negative diffraction orders.

The case of p-polarized visible light has been treated separately, as the observed behavior was completely different. In particular, the curves were rather irregular, with no clear peak around the Bragg angle. Instead higher asymmetric peaks appeared in place of the

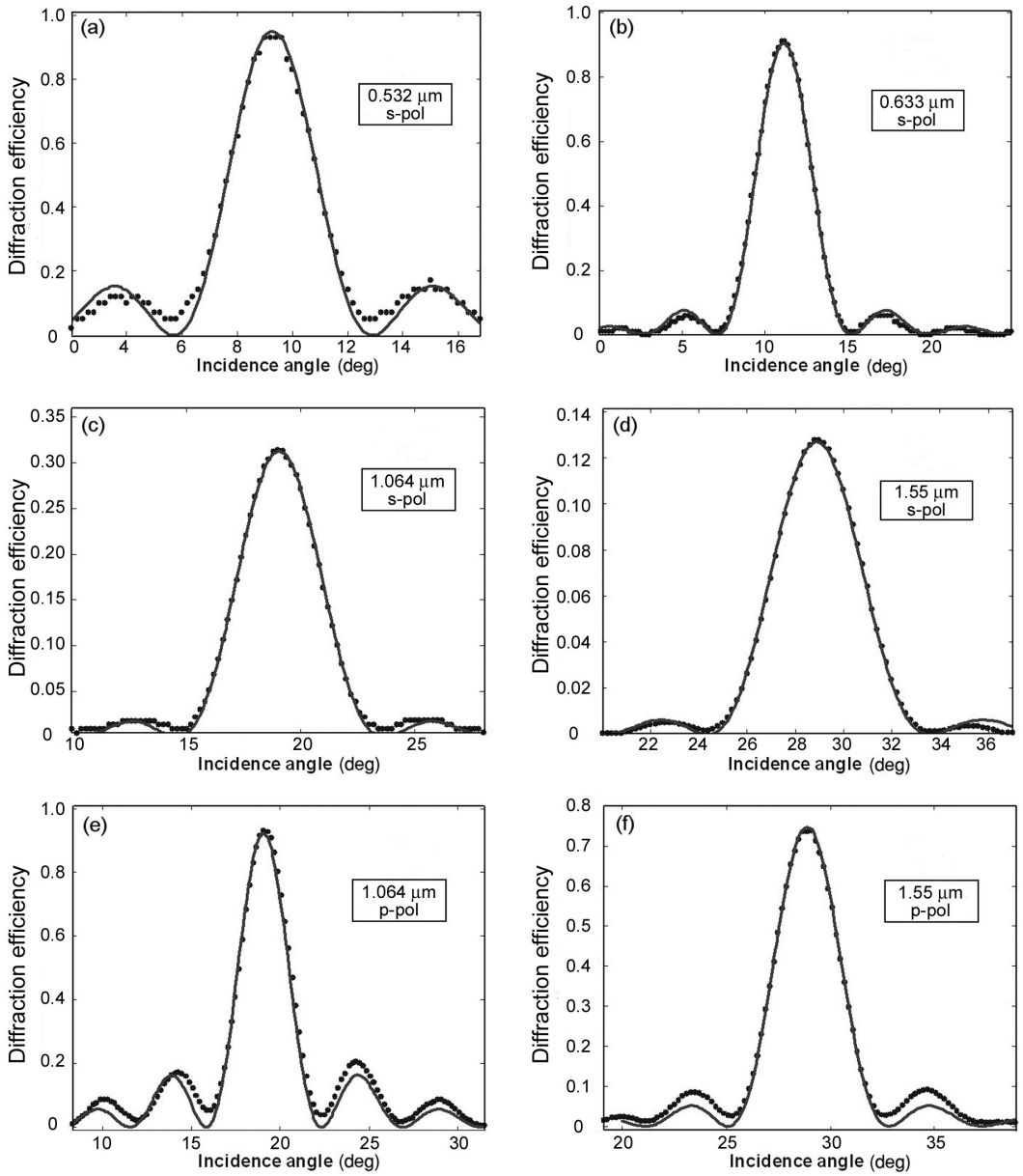

Figure 4.1: Diffraction efficiency dependence on the incidence angle for different wavelengths and polarizations: experimental data (dots) and theoretical fits (lines).

side lobes. Evidently gratings were in a condition of overmodulation, and this case will be discussed separately later on.

4.2.2 Data fitting

Considering again the more regular curves represented in Fig. 4.1, it can be noticed that the maxima of diffraction efficiency vary in a wide range of values: DE is very high for visible s-polarized light ($\gtrsim 90\%$), much lower in the NIR ($10 - 30\%$); instead, for NIR p-polarized light DE ($70 - 90\%$) is rather high as well. This large variation is in contrast with the properties of isotropic gratings. Indeed, it is not explainable in the frame of the Kogelnik theory, which predicts a higher coupling constant, i.e. a higher DE[13], for s-polarized light than for p-polarized light (see Sec. 2.4.2). This means that the assumption, correct for PDLCs and often extended to H-PDLCs, that the droplet directors are randomly oriented, does not hold true for our samples. This is not surprising since a higher efficiency in p-polarization is typical for many transmission H-PDLCs made from similar mixtures [16, 25]. This is a clear indication of the anisotropic nature of the H-PDLC gratings, due to a preferred orientation of the LC domains, in this case along the grating vector.

In this situation, trying to fit the experimental data with Kogelnik's theoretical model is pointless. Instead Montemezzani and Zgonik's theory for anisotropic gratings must be used. In this theory the grating is described by a permittivity modulation tensor $\underline{\boldsymbol{\epsilon}}_1$[14]

$$\underline{\boldsymbol{\epsilon}}_1 = \begin{pmatrix} \epsilon_{1,x} & 0 & 0 \\ 0 & \epsilon_{1,y} & 0 \\ 0 & 0 & \epsilon_{1,z} \end{pmatrix}, \tag{4.1}$$

while the grating strength ν depends on the parameter $\mu = \left(\hat{\mathbf{e}}_S^T \cdot \underline{\boldsymbol{\epsilon}}_1 \cdot \hat{\mathbf{e}}_R\right)$ (Eq. 2.56). Explicitly, one has for s- and p-polarized light

$$\mu_s = \epsilon_{1,y}, \tag{4.2a}$$

$$\mu_p = \epsilon_{1,x} \cos\theta_1 \cos\theta_2 - \epsilon_{1,z} \sin\theta_1 \sin\theta_2, \tag{4.2b}$$

where θ_1 and θ_2 are the angles made by the signal and reference energy propagation vectors (Poynting vectors) in respect to the z-axis. Consequently, one is sensitive to $\epsilon_{1,y}$ when probing in s-polarization, and to a combination of $\epsilon_{1,x}$ and $\epsilon_{1,z}$ in p-polarization. In applying Montemezzani and Zgonik's expression for the diffraction efficiency (Eq. 2.55) to the present case, it can be observed that walk-off angle β is very small and can be neglected. By the same token, the implicit dependence of n_0 on the incidence angle plays a minor role in

[13] The assertion "higher dielectric modulation⇒higher diffraction efficiency" does not hold when the grating is in overmodulation condition.

[14] Choosing a diagonal form for $\underline{\boldsymbol{\epsilon}}_1$ we are excluding the possibility of coupling between s- and p-polarization, according to the experimental evidence.

Wavelength $\lambda\,(\mu\mathrm{m})$	**Thickness** $d\,(\mu\mathrm{m})$	$\epsilon_{1,y/z}$	$\epsilon_{1,x}$
0.532	33.4 ± 0.3	0.0279 ± 0.0005	–
0.633	33.1 ± 0.2	0.0235 ± 0.0003	–
1.064	32.2 ± 0.1 36.5 ± 0.3	0.0188 ± 0.0001	0.0558 ± 0.0009
1.55	33.0 ± 0.3 36.9 ± 0.4	0.0159 ± 0.0001	0.0475 ± 0.0005

Table 4.1: Results of the fits on the angular DE curves. For the two NIR wavelengths the second value of the thickness *d* is obtained from *p*-polarized light measurements.

the calculations. In fact, we performed check calculations without assuming these approximations, but we did not get any significant difference.

The grating thickness d and the components of the permittivity modulation were hence chosen as fitting parameters. However, instead of introducing four variables in the fit, it was preferred to assume the material uniaxial, with the optical axis parallel to the grating vector, i.e. $\epsilon_{1,y} = \epsilon_{1,z}$. This assumption is commonly found in literature [44, 45, 40, 46] and is connected to the symmetry of the LC droplets in the direction orthogonal to fringes.

Fits were performed independently for each curve; results are shown as continuous lines in Fig. 4.1: the agreement with the experimental data is very good in s-polarization, slightly less in p-polarization. In this case, the model is not able to fit exactly the side lobes (cf. with similar fits in [45, 47, 48]). Even releasing the assumption on the uniaxiality of $\underline{\epsilon}_1$ does not improve the fit. In fact, the main discrepancy is that DE does not reach zero in the minima between the central and the side peaks. This is probably due to an attenuation of the permittivity modulation through the depth of the sample (tapering of the refractive index profile) [50].

The best fit parameters are reported in Tab. 4.1 for the different wavelengths. The order of magnitude of the permittivity modulation components are in agreement with published data [44, 40]; moreover, $\epsilon_{1,x}$ is always larger than $\epsilon_{1,y/z}$, indicating a preferred alignment of the LC molecules in the direction of the optical grating. This is commonly observed in H-PDLC transmission gratings containing E7 liquid crystal [16, 25]. Both components of the permittivity modulation tensor are evidently decreasing with the wavelength, due to the refractive index dispersion of the involved materials. Finally, the thickness values obtained by the s-polarization fits are reasonably higher than the spacer thickness as expected, and in good agreement with each other. The ones obtained by p-polarization fits are slightly different: this could be connected with the lower accuracy of the fit, trying to compensate the mismatch in the side lobes by increasing the thickness.

It is interesting to compare the values of efficiency measured in these experiments with other ones reported in literature for analogous samples. For instance, in Ref. [25] is mentioned an $8\,\mu\mathrm{m}$ thick grating made from the following mixture: DHPHA, E7 30%, surfactant

(octanoic acid) 4%, RB $\sim 1\%$. Authors report efficiencies at $\lambda = 633\,\mathrm{nm}$ of ~ 0.99 for p-polarization and ~ 0.13 for s-polarization, apparently very different from the one measured for our samples. However, as evident from Eqs. 2.55 and 2.56, for a given permittivity modulation tensor, DE can be moved from a maximum to a minimum by changing the sample thickness. Thus, the previously mentioned discrepancy should be analyzed in this frame. From our measurements of $\underline{\epsilon}_1$ it is possible to extrapolate the values of DE for different values of d: for instance, an $8\,\mu\mathrm{m}$ sample yields $\eta_s = 0.09$ and $\eta_p = 0.49$, whereas a $13\,\mu\mathrm{m}$ sample gives $\eta_s = 0.22$ and $\eta_p = 0.90$. These values are comparable to the ones reported in [25].

It follows that increasing d, up to a given value corresponding to $\nu = \pi/2$, produces an increase of η for both polarizations. In our sample the value of thickness is so high that a very high DE is observed for s-polarization, whereas the grating enters the overmodulation condition ($\nu > \pi/2$) and loose the Bragg regime for p-polarization. This behavior is not manifested in the NIR range, because longer wavelengths push farther the thickness corresponding to the overmodulation limit, so that it is not reached in our sample. This point is further discussed below.

Here it is important to outline that, even if DE is definitely the most important grating feature from an application point of view, it is always necessary to refer to the permittivity modulation when comparing different samples and evaluating their properties.

4.3 Morphological model

The measurement of the permittivity modulation tensor is the first fundamental step to analyze the properties of holographic gratings. The second step consists in finding a relationship between the measured values, the optical constants of all involved materials, and the grating structure. Actually, a lot of factors should be taken into account to describe the microscopic structure of a H-PDLC samples: the shape, dimension, and orientation of the LC droplets (and the correspondent distribution), as well as the alignment of the LC director inside each droplet (and the droplet order parameter) [8, 9, 51]. Most of these morphological details are unknown or highly dependent on the mixture composition, geometrical parameters (in particular on the grating spacing), and on the details of the curing process. Necessarily this approach would be either extremely complex (and involving a high number of fitting parameters) or based on quite drastic assumptions.

The model proposed in this work does not pretend to be a realistic microscopic picture of H-PDLCs; instead it is a simplified description, taking into account the main morphological features of these materials from a phenomenological point of view. With this in mind, the following parameters are introduced:

- α is the fraction of liquid crystal molecules not phase separated and randomly trapped in the polymer network; they concur with the polymer to form the matrix in which the LC droplets are embedded and cannot reorient under an applied electric field;
- β is a phenomenological parameter taking into account the effect of the fraction of liquid crystal phase separated and preferentially oriented in a given direction, namely the x-direction according to the experimental indications;
- finally, the remaining amount of the LC molecules $(1 - \alpha - \beta)$ is assumed to be phase separated and (on average) isotropically oriented.

It must be emphasized that these quantities must be considered more as phenomenological parameters than as a realistic description of the grating structure. Therefore, they are rather general and can be applied to describe different gratings, regardless of their morphological details.

Parameter α, for instance, can represent two distinct physical situations: the presence of non phase-separated LC molecules homogeneously dissolved in the polymer matrix, or the existence of very small phase-separated LC domains even in the polymer-rich regions. The two description are almost impossible to tell without an analysis at the microscope. For instance, SEM images reported in [44] seem to confirm the second hypothesis; unfortunately authors also state that the presence of small droplets in the irradiated regions is strongly dependent on the grating pitch. In other words, a wide variability is present among H-PDLC samples. Probably the most realistic picture is a gradient in the droplet density and dimension moving from the non irradiated to the irradiated areas, as suggested by [49]. However, knowledge of microscopic details is often not really necessary if one is interested in the effects of morphology on optical and electro-optical properties. What is relevant in this case is that such "LC content trapped in the polymer network" is characterized by 1) an isotropic distribution and 2) a lack of mobility under electric fields[15]. Therefore, its only effect is a reduction of the refractive index modulation, which is completely described by introducing an α-dependent effective permittivity for the polymer matrix

$$\epsilon_{mat} = \frac{f_p}{f_p + \alpha f_{lc}} \epsilon_p + \frac{\alpha f_{lc}}{f_p + \alpha f_{lc}} \epsilon_{iso}. \tag{4.3}$$

Here f_p and $f_{lc} = 1 - f_p$ are respectively the fraction of polymer (monomer + reactive diluent) and liquid crystal in the initial mixture, $\epsilon_p = n_p^2$ is the polymer permittivity, $\epsilon_{iso} = \frac{1}{3}\left(n_e^2 + 2n_o^2\right)$ is the LC permittivity in the randomly distributed state.

[15] In the case of small phase separated nematic droplets, some mobility is still possible, but for electric field much higher than the ones nedeed to reorient the larger droplets forming the LC-rich regions.

A similar approach is used to take into account the experimental evidence of grating anisotropy. A realistic description of the liquid crystal alignment would assume the knowledge of the many variables describing droplet morphology in PDLC-like materials. As before, this knowledge is difficult to obtain, never general and often unnecessary for most practical purposes. Introducing a parameter β, as defined above, overcomes this difficulty. As a matter of fact, the LC tendency to stay aligned along the x-axis can be modeled as if a fraction β of the LC molecules were phase-separated and fully aligned along the grating vector, and a fraction $1-\alpha-\beta$ were phase-separated but isotropically oriented. Of course, β should be regarded as an averaged parameter, representing at the same time two different effects: the LC alignment in each droplet (hence the droplet order parameter S_d), and the distribution in shape, dimension, and orientation of the LC droplets in the whole sample.

In this simplified description, the i-th diagonal component of the average (anisotropic) permittivity tensor $\underline{\boldsymbol{\epsilon}}_0$ is easily expressed as

$$\epsilon_{0,i} = f_p\epsilon_p + \beta f_{lc}\epsilon_{lc,i} + (1-\beta)\, f_{lc}\epsilon_{iso}, \tag{4.4}$$

where $\epsilon_{lc,i}$ represents the i-th diagonal component of the LC permittivity tensor. Assuming that the grating consists of stripes of homogeneous polymer/LC matrix and stripes containing LC droplets, all having the same thickness, as shown in [17] for similar materials, one can express the i-th component of the permittivity modulation tensor $\underline{\boldsymbol{\epsilon}}_1$ simply as the difference between the average permittivity and the polymer matrix one:

$$\epsilon_{1,i} = \epsilon_{0,i} - \epsilon_{mat}. \tag{4.5}$$

Here we are also making the implicit assumption that the modulation profile is sinusoidal. In principle this could not be the case, of course; then, in order to use coupled-wave theory, one should apply a Fourier expansion to the actual profile, and thus add a coefficient in front of $\underline{\boldsymbol{\epsilon}}_1$. However, the low sharpness of the interface between polymer- and LC-rich layers, typical of H-PDLCs (cf. again SEM images in [17]), makes reasonable to consider such parameter very close to one.

Equation 4.5 can be recasted to point out the role of α and β. For $\beta = 0$ (isotropic grating), it becomes (we can drop the index i)

$$\epsilon_1 = \frac{f_p f_{lc}}{f_p + \alpha f_{lc}}\,(1-\alpha)\,(\epsilon_p - \epsilon_{iso})\,, \tag{4.6}$$

which tends to $\epsilon_1 = 0$ for $\alpha = 1$ (absence of phase-separated liquid crystal), and to $\epsilon_1 = f_{lc}\,(\epsilon_p - \epsilon_{iso})$ for $\alpha = 0$. For this reason α, or better $1-\alpha$, plays the role of an optical contrast parameter.

Analogously, one can writes the difference between the two components of the permittivity modulation as

$$\epsilon_{1,x} - \epsilon_{1,y/z} = \beta f_{lc}\Delta\epsilon, \tag{4.7}$$

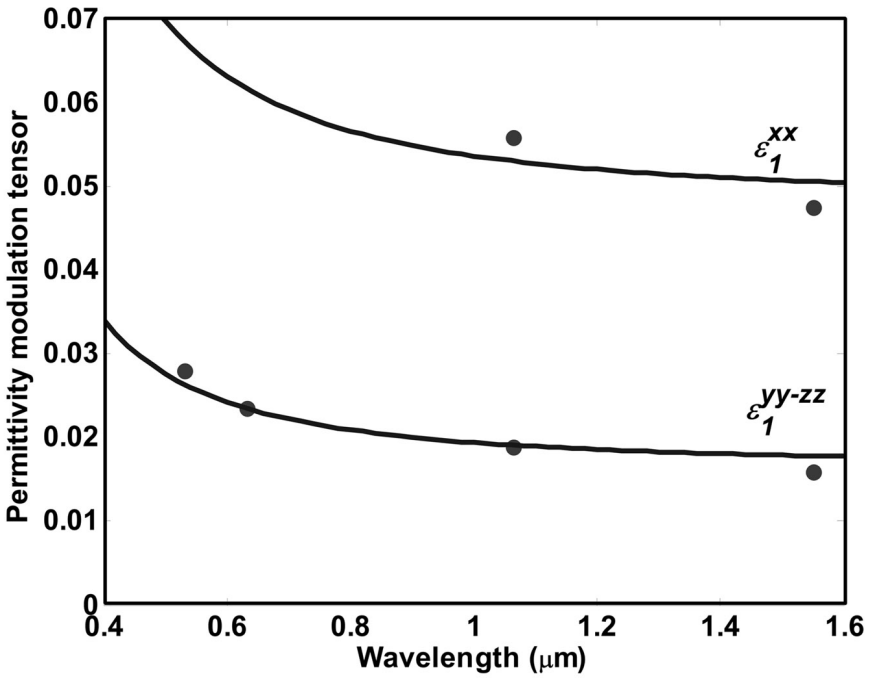

Figure 4.2: Components of the permittivity modulation tensor versus wavelength: dots correspond to the values reported in Tab. 4.1; continuous lines are the best fit curves on these points, according to the model described in the text.

in which $\Delta\epsilon$ is the liquid crystal anisotropy. Hence β is the parameter connecting the grating and the liquid crystal anisotropy.

Using this model it is possible to fit the experimental values of the components of $\underline{\epsilon}_1$, as resulted by the angular measurements (Tab. 4.1), with α and β as fit parameters. The results are shown in Fig. 4.2. Again, s-polarization provides better agreement with experimental data than p-polarization; however, points in p-polarization are affected by a larger error due to the poorer accuracy in the angular fits. The values of α and β that better fit our experimental values are $\alpha = 0.44 \pm 0.01$ and $\beta = 0.138 \pm 0.008$.

A comparison of these values to other ones reported in literature requires some care, due to different models and definitions. Moreover, it is generally accepted, as we mentioned above, that the grating morphology strongly depends on many parameters that can vary from experiment to experiment. Hence, such comparison can be only qualitative. For instance, our value of α leads to a matrix composition given by 77% of polymer and 23% of LC; for similar samples a LC percentage of 19.4% is reported in [52]. Another quantity that can be calculated is the ratio between the effective fraction of aligned LC and the total amount of phase-separated LC, i.e. the quantity $\beta/(1-\alpha)$. For the studied sample this value is 0.25,

which can be cautiously compared to the LC order parameter reported in [29] (~ 0.3), which is somehow a different way to indicate a similar characteristic.

4.4 Comments on the effects of the optical dispersion

In studying diffraction Bragg gratings the influence of wavelength is two-fold: through the definitions of ν (Eq. 2.26), and through the refractive index optical dispersion. The latter is neglected in most studies on holographic gratings. Indeed this simplification is reasonable for those conventional materials, in which exposure induces only a slight change in the optical properties of the recording medium. In this case, the exposed and non-exposed areas exhibit dispersion curves that are almost parallel. As a consequence, optical modulation remains almost constant with the wavelength, in the range of interest.

This is not the case for gratings like H-PDLCs, recorded in composite materials. In these systems optical dispersion acts in a different way on polymer and liquid crystal; in general dispersion curve is much steeper for LC extraordinary refractive index than for polymer and LC ordinary refractive index. Therefore, even a small variation of the absolute values of the optical constants can result in a significant variation of the refractive index modulation. In transmission gratings the effect is also amplified by the fact that diffraction efficiency has an oscillatory dependence on the grating modulation.

Unfortunately considering optical dispersion in H-PDLC gratings is not straightforward, for the simple reason that optical constants of the involved materials are known only for few visible wavelengths. In particular, almost nothing is known about LC refractive indices in the NIR range, making difficult a precise design of LC-based telecom devices. In performing the analysis described in the previous section, effects of optical dispersion were taken into account by assuming for all materials a two-parameter Cauchy dispersion formula:

$$n(\lambda) = A + \frac{B}{\lambda^2}. \tag{4.8}$$

The Cauchy parameters a and b used for polymer and liquid crystal are reported in Tab. 4.2. Dispersion curve for the polymer was obtained by a direct measurement. The one for LC was a rough estimate obtained by fitting few data available in literature at three single wavelengths. After this part of the work of thesis was completed, new spectroscopic measurements were carried out on E7 and a much more reliable dispersion curve was obtained. This is discussed in Chapter 6. However, remade calculations using the new data have not resulted in significantly different values of α and β.

Conversely, not considering dispersion produces significant displacements from the real values. This is evident in Fig. 4.3, where two curves of DE vs. wavelength are plotted: the first one is obtained neglecting dispersion, assuming for the permittivity modulation

Material	A	B (μm^2)
Polymer	1.5081	0.0061
LC, ordinary	1.4950	0.0090
LC, extraordinary	1.6858	0.0210

Table 4.2: Cauchy coefficients used to describe the dispersion curves for the polymer and the liquid crystal refractive indices in H-PDLC gratings. For more accurate values of E7 Cauchy parameters see Chapter <ref>Chapter-ellipsometry</ref>.

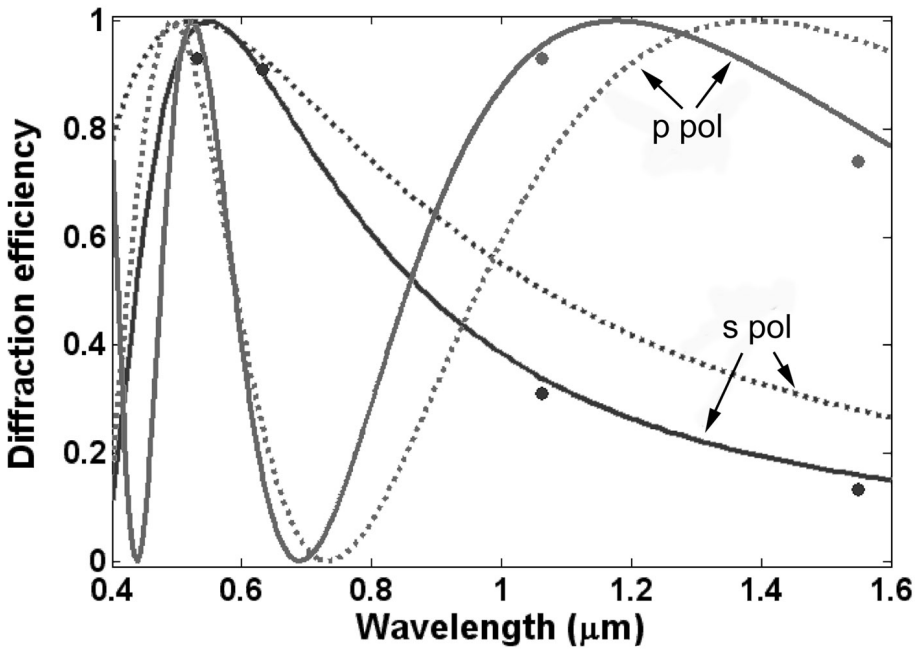

Figure 4.3: Experimental DE values (points), and two different theoretical curves: including optical dispersion (continuous line), and neglecting it (dotted line).

tensor the value measured at $0.633\,\mu m$; the second one is computed using the dispersion coefficients reported in Tab 4.2. Quite obviously, the experimental points are much better fitted by the second curve. Correspondingly, the first curve gives more and more unreliable predictions as further one moves from the wavelength region where the refractive indices were measured. The disagreement is even more pronounced for thicker samples.

In conclusion, the role of optical dispersion is very important to produce reliable descriptions of the behavior of gratings recorded in composite materials. This is especially true, when the efficiency in the infrared range is extrapolated from measurements in the visible range. Furthermore, optical dispersion also reflects on the switching properties. Indeed, gratings switch to the OFF state when the condition of perfect index matching is reached. Clearly, when indices change according to different curves, the matching condition can be

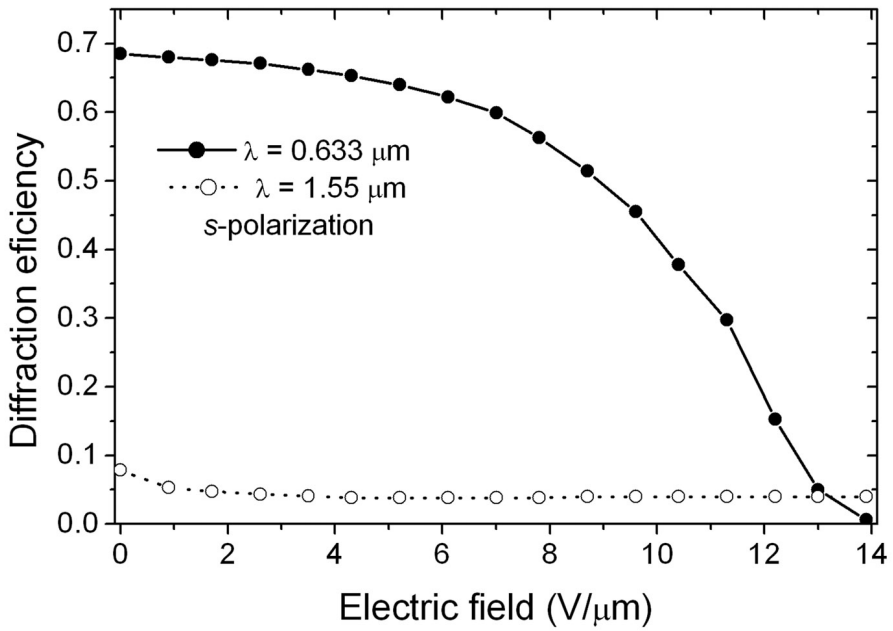

Figure 4.4: Diffraction efficiency versus applied electric field for *s*-polarized light at two different wavelengths: $0.633\,\mu\mathrm{m}$ (full circles) and $1.55\,\mu\mathrm{m}$ (open circles).

obtained at different voltages for different wavelengths; at certain wavelengths a perfect match could be impossible as well.

4.5 Measurements under electric field

H-PDLC electro-optical properties were studied by applying an AC square voltage at a sufficiently high frequency, say $1\,\mathrm{kHz}$, as usually made in order to avoid unwanted DC screening and current effects. The electro-optical response of the sample is shown in Fig. 4.4: at $0.633\,\mu\mathrm{m}$, DE is reduced to one half at $11\,\mathrm{V}/\,\mu\mathrm{m}$ and vanishes at $14\,\mathrm{V}/\,\mu\mathrm{m}$; at $1.55\,\mu\mathrm{m}$, a small initial DE decreasing is obtained at weak fields, from 1 to $2\,\mathrm{V}/\,\mu\mathrm{m}$, after that DE stabilizes not going to zero, indicating that a perfect index matching of the two components is never reached.

The switching behavior shown for red light is rather typical for H-PDLC gratings. In particular, the measured switching voltage is relatively high (but in the average for H-PDLCs), and the DE curve goes to zero with a very smooth slope. Lower switching voltages for these kind of gratings have been reported in literature [51], when surfactants were added to the photosensitive mixture; drawbacks of these solution have been discussed previously.

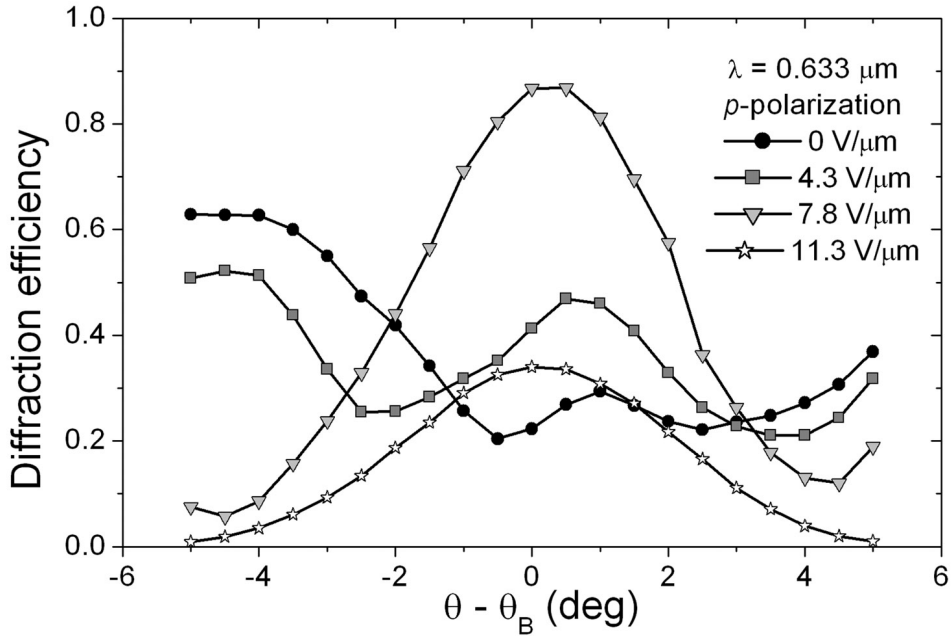

Figure 4.5: Diffraction efficiency versus incidence angle for different applied electric fields, p-polarization and $\lambda = 0.633\,\mu\mathrm{m}$.

The effect of the electric field for p-polarized visible light is also very interesting. It has been previously observed that in this condition the studied sample did not show any diffraction peak around the Bragg angle. However, by applying an electric field the angular behavior of DE was continuously changing (Fig. 4.5): finally, at $7.8\,\mathrm{V}/\,\mu\mathrm{m}$, a curve very similar to the one obtained for s-polarization and zero field was observed; a further increase of the electric field led to switch the grating off, as expected.

This strange behavior is explainable considering the measured values of the permittivity modulation tensor. From the upper curve reported in Fig. 4.2, one can extrapolate the values of $\epsilon_{1,x}$ at visible wavelengths: they are so high that result in a grating overmodulation. In this condition a drastic change in DE angular dependence is expected, because a decrease of the central Bragg peak in favor of the side maxima is observed for increasing $\nu > \pi/2$ (at $\nu = \pi$, Bragg peak amplitude gets a null value and a minimum is obtained). However, in this case it was not possible to fit the experimental angular dependence of DE with the coupled-wave model, even considering overmodulation.

Although different reasons can be involved in producing the observed phenomenon, a critical one should be connected with the actual diffraction regime of the studied gratings. In Sec. 2.6 the limits of Bragg and Raman-Nath regimes have already be seen to depend on two conditions (Eq. 2.61 and 2.62). These inequalities define three areas in the $Q - \nu$ plane, corresponding to three different diffraction conditions: the Raman-Nath, the Bragg, and an

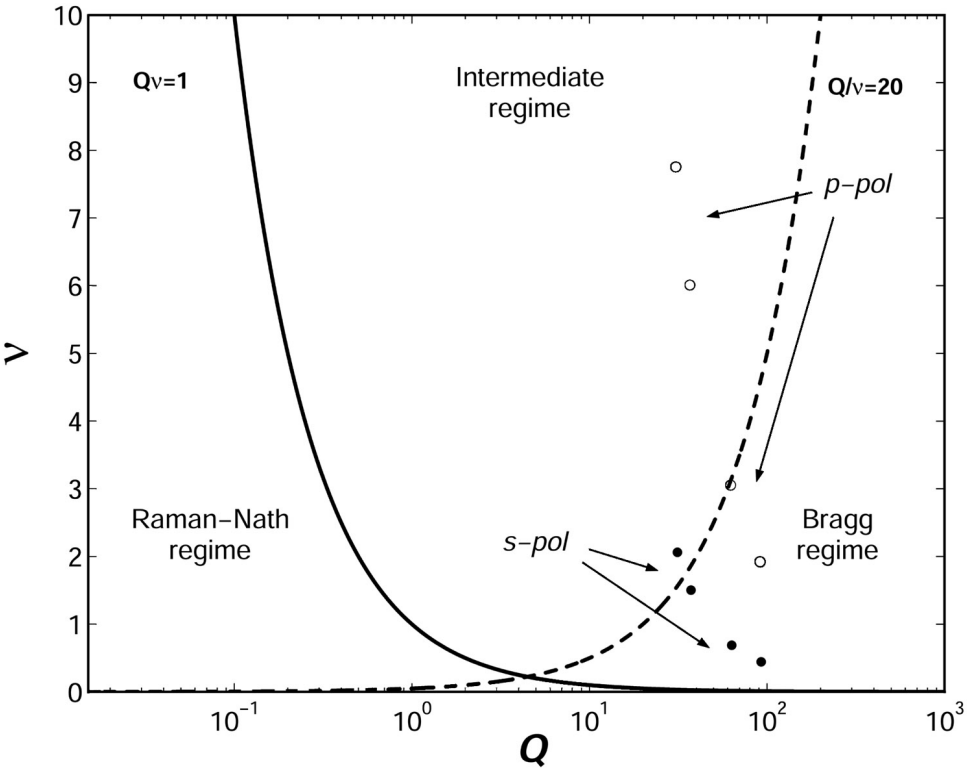

Figure 4.6: .Diffraction regime diagram as a function of the grating strength ν and the thickness parameter Q, according to Eqs. (XXX). Full and open circles represent gratings studied with s-polarized and p-polarized light, respectively, at four wavelengths ($0.532\,\mu\mathrm{m}$, $0.633\,\mu\mathrm{m}$, $1.064\,\mu\mathrm{m}$, and $1.55\,\mu\mathrm{m}$). For each polarization, wavelength is decreasing with ν (the shorter the wavelength, the higher the respective circle position in the diagram).

intermediate regime. For the last case, no analytical theory exists and a numerical approach has to be used.

The grating position in the $Q - \nu$ plane is showed in Fig. 4.6, for the different polarizations and wavelengths: for s-polarization, our samples are always in the Bragg regime or very close to it (at $\lambda = 0.532\,\mu\mathrm{m}$); for p-polarization points fall in the Bragg area for the longest wavelengths, but are in the intermediate area for the visible wavelengths, due to the high value of ν. This was confirmed observing an increase in the intensity of the higher order diffracted beams.

This consideration also provides a qualitative explanation to the observed behavior under an external voltage. The applied electric field induces the reorientation of the LC molecules along the z-axis, resulting in a smaller value of the coupling constant and, hence, of ν. As a consequence, increasing the voltage, the points in the graph move down vertically and finally enter the Bragg regime area for a certain value of ν

Chapter 5
Policryps and Poliphem characterization

5.1 Introduction

The second part of the thesis work has regarded the study of non-droplet gratings, namely Policryps and Poliphem. In comparison to H-PDLCs, this new class of gratings is at an earlier stage of development, so much work is still to be done in order to test and optimize all their properties and get a deeper insight into their morphology. This work wants to provide a contribution in this direction, aiming to demonstrate the improved capabilities of these materials, both in the visible and in the NIR range. Measurements discussed in this chapter mostly regard Policryps gratings, which have been studied for a longer time [53, 54, 55, 56]. However, a number of Poliphem gratings was also characterized and some early results is reported, mainly to compare the properties of the two types of gratings; data regarding Poliphem are mostly unpublished.

The main properties of the sample analyzed in this chapter are summarized in Tab. 5.1. Policryps gratings were provided by Umeton's group at the University of Calabria (Cosenza, Italy), in the frame of two Italian National Research Projects [42, 57]. Several Poliphem gratings were prepared by Stumpe's group at the Fraunhofer Institute for Applied Polymer Research (Potsdam, Germany); others were realized in our laboratory at the University of Naples (Naples, Italy). All they were produced according to the special production procedures described in Sec. 3.5.

	Policryps			**Poliphem**		
Sample	A	B	C	D	E	F
Thickness	8.8	7.8	12	5.6	5.0	
Spacing	1.34	1.34	0.6	0.39	0.37	

Table 5.1: Geometrical parameters of Policryps and Poliphem samples.

As in the previous chapter, diffraction efficiency is defined as the ratio between the diffracted beam intensity and the sum of the transmitted and diffracted light intensities, in order to ignore all possible losses. However, in contrast to H-PDLCs, here all the measurements are referred to p-polarized light. As explained in Sec.3.5, because of the highly oriented configuration of the LC molecules orthogonally to the polymer slices, the grating optical contrast is very high for p-polarized light, but almost null for s-polarized light; in the lat-

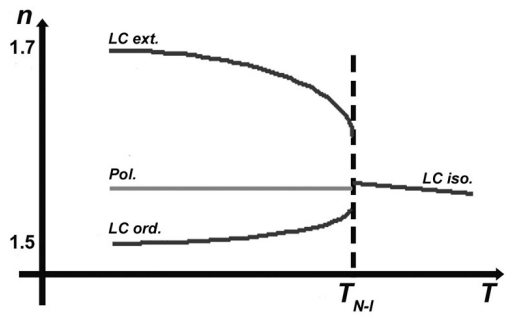

Figure 5.1: Qualitative dependence on the temperature of liquid crystal refractive indices. In comparison to liquid crystal, polymer refractive index is almost constant with temperature.

ter case, even applying an electric field does not increase the diffraction efficiency and in general a diffracted beam is barely visible.

5.2 Thermal properties

In general polymer-LC gratings can operate at room temperature without any temperature control on the sample. However, when the clearing point is close to the room temperature, a change in the temperature by few degrees can produce a noticeable change in the grating diffraction properties. In Fig. 5.1 is shown the typical thermal behavior of LC refractive indices: the closer is the transition point, the steeper is the change of n_e, which decreases, and n_o, which increases; at $T = T_{N-I}$, birefringence goes abruptly to zero and the refractive index of the isotropic phase becomes approximately $n_{iso} \simeq \frac{1}{3}(n_e + 2n_o)$. This value is typically very close to the polymer refractive index n_p; for instance $n_p = 1.56$ for NOA-61 (Tab. 3.2), while $n_{iso} \simeq 1.57$ for 5CB liquid crystal. As a consequence, when the operating temperature reaches the clearing point, the refractive index modulation vanishes and with it the diffraction efficiency.

This was evident in the samples of Policryps and Poliphem gratings containing 5CB as liquid crystal. Because of its low clearing point ($\sim 35\,^{\circ}\mathrm{C}$), 5CB is definitely not the best choice for final devices. Nonetheless, it was initially chosen, in phase of development, for its well-known optical properties and the good behavior when mixed in with NOA resins. DE variation with temperatures is shown in Fig. 5.2a for a typical policryps grating (sample A), at two different wavelengths, $0.633\,\mu\mathrm{m}$ and $1.55\,\mu\mathrm{m}$. At both wavelengths diffraction efficiency drops off sharply at a temperature $6 \div 7\,^{\circ}\mathrm{C}$ lower than the nominal value. This shift is due to residual chemical impurities (non reacted monomer and photoinitiator molecules) present in the phase-separated liquid crystal at the end of the curing process. For $T > T_{N-I}$,

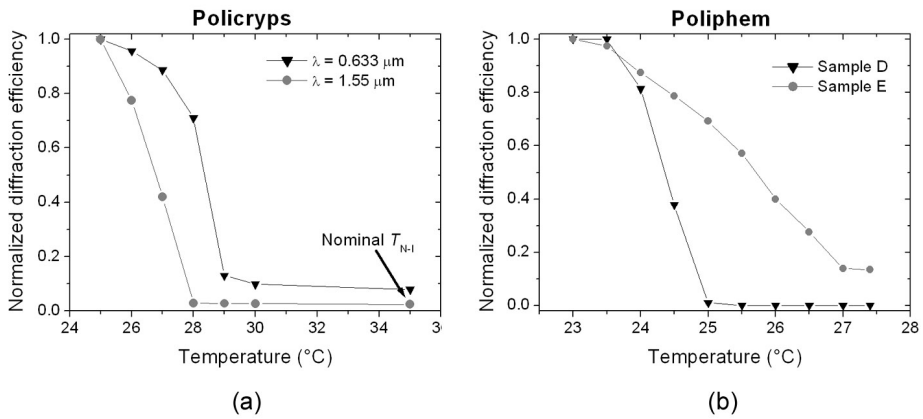

Figure 5.2: Normalized diffraction efficiency vs. temperature: for a Policryps grating (sample A) at two different wavelengths, $0.633\,\mu\mathrm{m}$ and $1.55\,\mu\mathrm{m}$ (a); for two Poliphem gratings (samples D and E) at $\lambda = 0.633\,\mu\mathrm{m}$ (b).

liquid crystal enters the isotropic phase and the diffraction efficiency becomes insensitive to a further increase of temperature; DE extinction is not complete for red light, because of a residual mismatch between the polymer and isotropic LC refractive index at that wavelength.

A similar behavior has been observed in Poliphem gratings. Fig. 5.2b shows the behavior of two different samples (D and E), tested at $\lambda = 0.633\,\mu\mathrm{m}$. Here the effective clearing point is different for the two samples, and in one case significantly lower than in Policryps samples. This indicates the presence of more impurities and hence a worse curing process.

The thermal instability can be greatly reduced, or even completely overcome, by using LC with a wider nematic range. For instance, Poliphem realized with a mixture of 7CB and 5CB in a ratio $1:3$ ($T_{N-I} \simeq 42.5\,^{\circ}\mathrm{C}$ for 7CB) instead of 5CB are significantly more stable and work up to a temperature of $\sim 30 \div 35\,^{\circ}\mathrm{C}$. Analogously, E7 liquid crystal ($T_{N-I} \simeq 58\,^{\circ}\mathrm{C}$) has been recently used to improve the operating range of Policryps gratings. Clearly, the change of liquid crystal in the photosensitive mixture is not trivial, because all the curing parameters must be changed consequently to preserve non-droplet morphology.

However, thermal effects can be also considered for non-electrical switching, when external voltages cannot be applied for any reason and fast response times are not required.

5.3 Diffraction efficiency and switching properties

The first important consequence of non-droplet morphology is the lowering of the switching field. Electric measurements were performed on Policryps and Poliphem by ap-

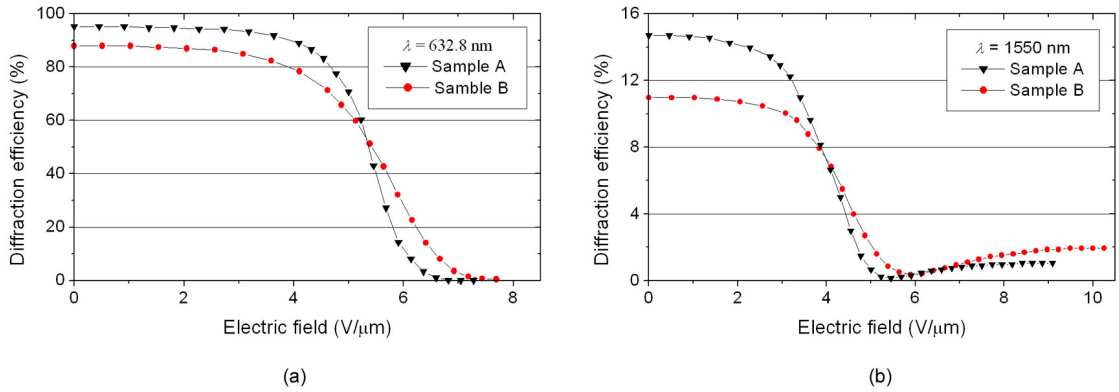

Figure 5.3: Diffraction efficiency vs. applied electric field for two Policryps gratings (samples A and B) at two different wavelengths: $\lambda = 0.633\,\mu\mathrm{m}$ (a) and $\lambda = 0.633\,\mu\mathrm{m}$ (b).

plying a $1\,\mathrm{kHz}$ AC square voltage. Typical results for two Policryps samples are shown in Figs. 5.3a-b, for both visible and NIR light wavelengths.

For red light, the reorientation begins around $4\,\mathrm{V}/\,\mu\mathrm{m}$ and the switching off is completed at $7\,\mathrm{V}/\,\mu\mathrm{m}$; in the NIR values are even lower, with DE starting to decrease at $2.5\,\mathrm{V}/\,\mu\mathrm{m}$ and vanishing at $5.5\,\mathrm{V}/\,\mu\mathrm{m}$. These values are interesting for applications, especially if compared with the larger values commonly observed in H-PDLCs, e.g. compare with Fig. 4.4. Furthermore, they have been obtained in the very first Policryps samples, not optimized at all for electric performance.

For NIR wavelength, a small "bounce" of DE is observed when the electric field is increased beyond the switching value (Fig. 5.3b). This means that at $\lambda = 1550\,\mathrm{nm}$ the grating OFF state is not reached when the molecular reorientation is completed in the LC regions, as is the case using red light, but instead for some intermediate configuration. Even more striking is the difference in the zero-field diffraction efficiency, which is very high ($\sim 90\%$) for red light, but much lower ($\sim 15\%$) in the infrared. This is not surprising, as early samples were optimized for working at visible wavelengths.

Figures 5.4a-b show similar characterizations performed on two different Poliphem samples. Interestingly, the switching fields observed in this case were even lower than for Policryps. In particular sample D was completely switched off by a field lower than $2.5\,\mathrm{V}/\,\mu\mathrm{m}$. It seems that a correlation exists between the electric switching and the thermal switching, with samples exhibiting a lower transition temperature, also showing a lower switching field. Actually, LC optical properties do not depend on the absolute working temperature T, but rather by the difference $T^*_{N-I} - T$, where T^*_{N-I} is the effective clearing point ($25\,^\circ\mathrm{C}$ for sample D, $27\,^\circ\mathrm{C}$ for sample E). Thus, on the base of Fig. 5.1, we can conclude

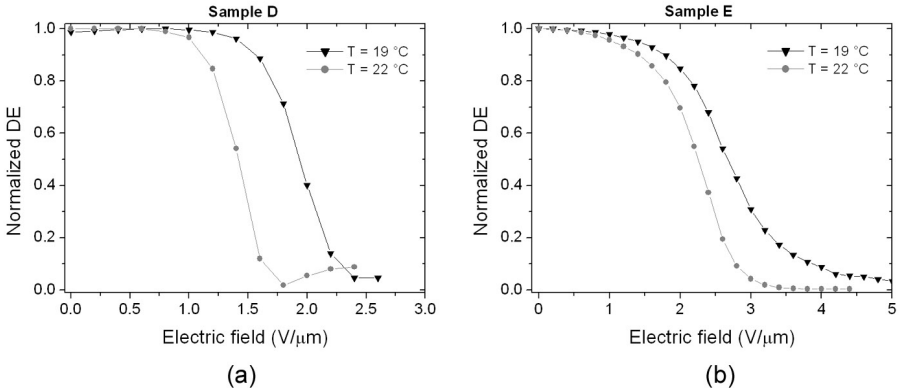

Figure 5.4: Normalized diffraction efficiency vs. applied electric field for two Poliphem samples: sample D (a) and sample E (b).

that the LC films in sample D show as a value of n_e lower than that one expected for sample E; as a consequence sample D needs a smaller reorientation to match the polymer refractive index. This qualitative interpretation is confirmed by the observation that the switching field for the same sample decreases when the temperature increases. However, this is not a real advantage as the diffraction efficiency, normalized to one in Figs. 5.4, decreases with the temperature as well.

5.4 Bandwidth and losses

Angular bandwidth is an important parameter for photonic applications. In Fig. 5.5 the grating response vs. the angle of incidence is shown. The full-width at half-amplitude is $\sim 9\,^\circ$ in agreement with prediction of Kogelnik theory (Eq. 2.31a). It is clear that thicker gratings would be necessary to increase the grating selectivity. For instance, measurements carried out on Policryps sample C, resulted in an FWHA value of $\sim 2\,^\circ$.

The wavelength bandwidth was measured in Poliphem samples: Fig. 5.6 shows transmission spectra for different incidence angles, corresponding to different Bragg wavelengths. The width of the minima is $\sim 50\,\mathrm{nm}$, equivalent to a $\sim 4\,^\circ$ angular bandwidth and in agreement with Eq. 2.32a. In Fig. 5.6 note also the high diffraction efficiency exhibited at $\lambda \simeq 0.425\,\mu\mathrm{m}$ (transmissivity vanishes almost completely), compared to the relatively low losses, less than 20% for $\lambda > 0.400\,\mu\mathrm{m}$ (below this value glass absorption is significant and transmissivity consequently falls off).

In general, the values of losses observed for Policryps and Poliphem were typically in the range $10 \div 20\%$, measured as the ratio between the total light power beyond the sample

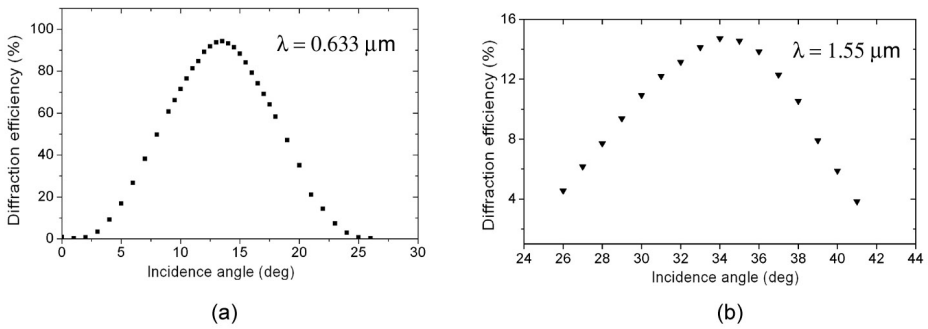

Figure 5.5: Diffraction efficiency vs. incidence angle for Policryps sample A at two different wavelengths: $\lambda = 0.633\,\mu\mathrm{m}$ (a) and $\lambda = 0.633\,\mu\mathrm{m}$ (b).

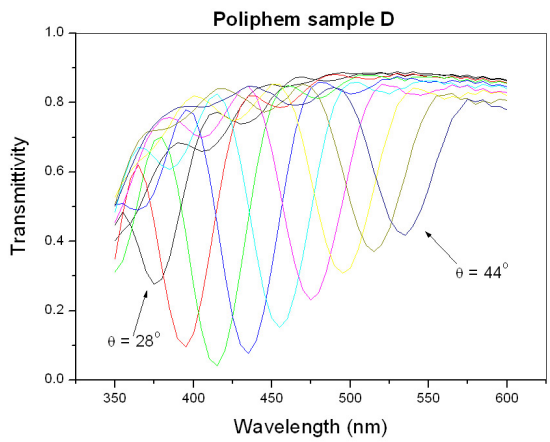

Figure 5.6: Poliphem transmission spectra at different angles of incidence (angular step $2\,°$).

(transmitted plus diffracted beam) and the incident beam power. Hence this estimates also includes reflection losses at the air-glass interface and possible absorption (by the glass at short wavelengths, by the ITO in the NIR). In the H-PDLC gratings analyzed in the previous chapter, losses were always larger than 30%, also reaching 50%. The great improvement of the optical quality derived by a non-droplet morphology is evident.

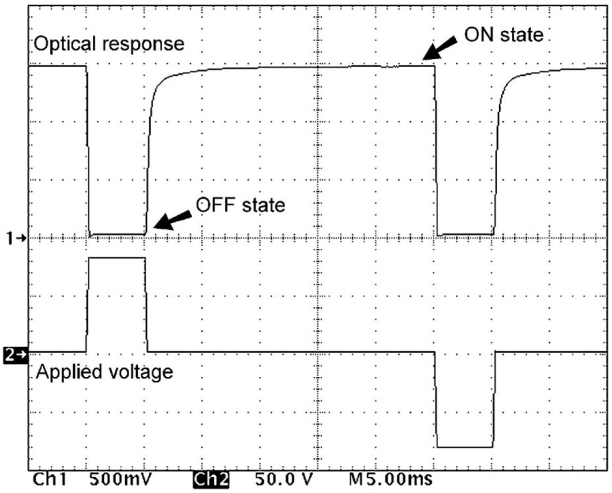

Figure 5.7: Oscilloscope snapshot of the applied field (channel 2) and the diffracted beam optical response (channel 1).

5.5 Switching times

5.5.1 Policryps dynamic measurements

A fundamental parameter for switchable Bragg gratings is the response time to variable electric fields. A thorough analysis of this property was performed on Policryps samples.

Experimentally, switching dynamics was measured by recording the diffracted beam signal detected by a photodiode, while electric pulses were applied to the grating with frequencies in the range $1 \div 100\,\mathrm{Hz}$; pulse amplitude was always large enough to completely switch off the diffractive device. In order to avoid static electric biasing of the sample, all the applied waveforms were zero-average over long time scales ($\gtrsim 100\,\mathrm{ms}$). Figure 5.7 shows a typical oscilloscope image, with the applied waveform and the optical response. As the response is measured on the diffracted beam, the grating ON state, i.e. the diffraction state, corresponds to no voltage applied (voltage off); vice versa the grating OFF state, i.e. the transmission state, occurs in presence of the electric field (voltage on).

Two typical measurements performed at $\lambda = 633\,\mathrm{nm}$ on the Policryps sample B are shown in Figs. 5.8a-b for two voltage frequencies f_1, $100\,\mathrm{Hz}$ and $1\,\mathrm{Hz}$, respectively (here time interval between consecutive pulses was taken equal to the pulse width). Here, instead of applying alternate positive and negative pulses as in Fig. 5.7, each pulse was further modulated at a faster frequency f_2, in the range $1 \div 10\,\mathrm{kHz}$[16], the voltage amplitude being

[16] Notice that in Figs. 5.8b and 5.9b, recorded with $f_1 = 1\,\mathrm{Hz}$, the modulation at f_2 is not viewable in the waveform, because the ratio f_2/f_1 is too high to allow both frequencies to be displayed

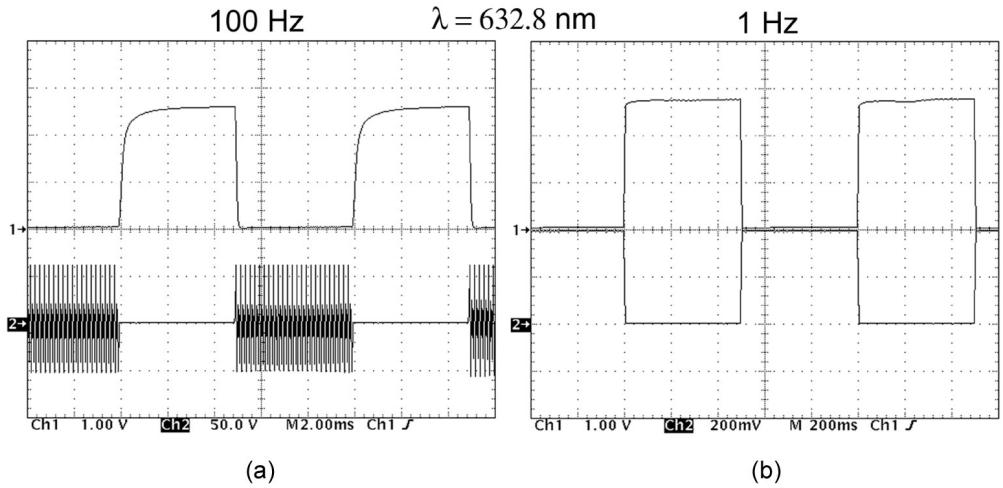

Figure 5.8: Optical response, upper curves, and driving waveform, lower curves, at $\lambda = 632.8\,\mathrm{nm}$; voltage frequency $100\,\mathrm{Hz}$ (a) and $1\,\mathrm{Hz}$ (b).

fixed at $60\,\mathrm{V}$ (corresponding to $7.7\,\mathrm{V}/\,\mu\mathrm{m}$). Indeed, liquid crystals have response times too slow to follow such fast driving signals as the ones at frequency f_2, so that the reorientation torque is almost equivalent to that imposed by a constant voltage of same rms value. The same set of measurements was performed also at $\lambda = 633\,\mathrm{nm}$, as shown in Figs. 5.9.

A summary of the measured times is presented in Tab. 5.2. Here τ_{fall} represents the response time when the electric field is applied (grating ON-OFF transition), τ_{fall} the response time after the electric field has been removed (grating OFF-ON transition); both times were automatically measured by the oscilloscope as the time interval between 10% and 90% of the optical signal; very similar values were obtained for Policryps sample A as well. For the way they were obtained, these values are affected by a rather large error, estimated around $15 \div 25\%$. Nonetheless, some conclusions can still be drawn:

- response times for NIR probe light are always longer than for red light, with a ratio varying between 1.5 and 4.5;
- rise times are always one order of magnitude longer than fall times;
- both rise and fall times seem generally to decrease with increasing pulse frequency.

The first conclusion could appear surprising, as the LC molecular reorientation is only driven by the electric and elastic forces and must not depend on the wavelength of the probe light. However, what is measured here is not the LC reorientation, but the consequent varia-

simultaneously; for the same reason the shown amplitude scale (channel 2) is meaningless.

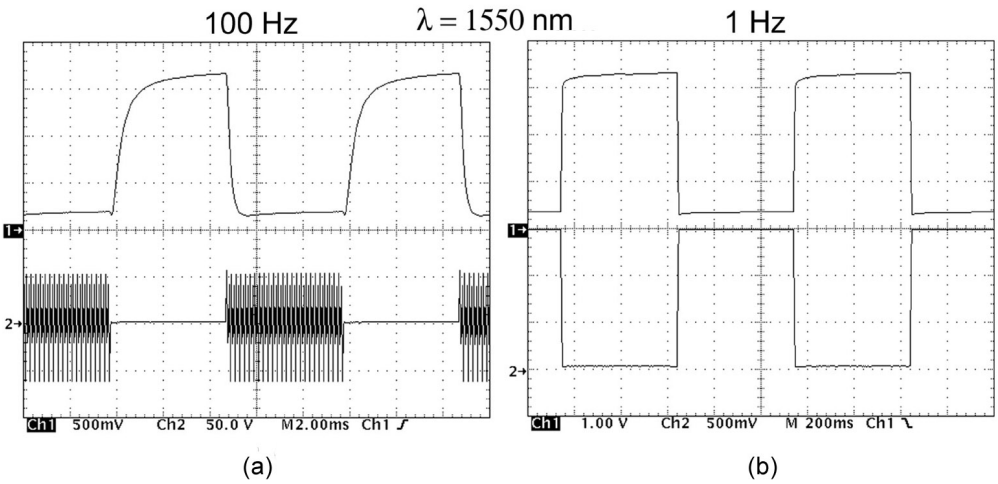

Figure 5.9: Optical response, upper curves, and driving waveform, lower curves, at $\lambda = 1550\,\mathrm{nm}$; voltage frequency $100\,\mathrm{Hz}$ (a) and $1\,\mathrm{Hz}$ (b).

tion of the diffraction efficiency; actually DE can be more or less sensitive to the LC orientation according to the light wavelength.

Light wavelength	Pulse frequency	Modulation frequency	Fall time	Rise time
$\lambda(\mathrm{nm})$	$f_1(\mathrm{Hz})$	$f_2(\mathrm{Hz})$	$\tau_{fall}(\mu\mathrm{s})$	$\tau_{rise}(\mu\mathrm{s})$
633	1	1000	160	1300
633	10	1000	130	1000
633	100	10000	70	900
1550	1	1000	440	2800
1550	10	10000	320	3200
1550	50	5000	370	1500
1550	100	10000	320	1300

Table 5.2: Response times of Policryps sample B.

The third conclusion is instead more questionable, because of the large error in the measurements. This is especially true for data taken at higher frequency: in this case pulse duration is too short to allow DE to reach the steady value, as evident in Figs. 5.8a and 5.7a. Time measurements are clearly affected by this bug; for instance, this could explain why fall times seem to decrease at higher frequencies. To clarify this point a new set of more precise dynamic measurements was carried out; it is discussed in the following section.

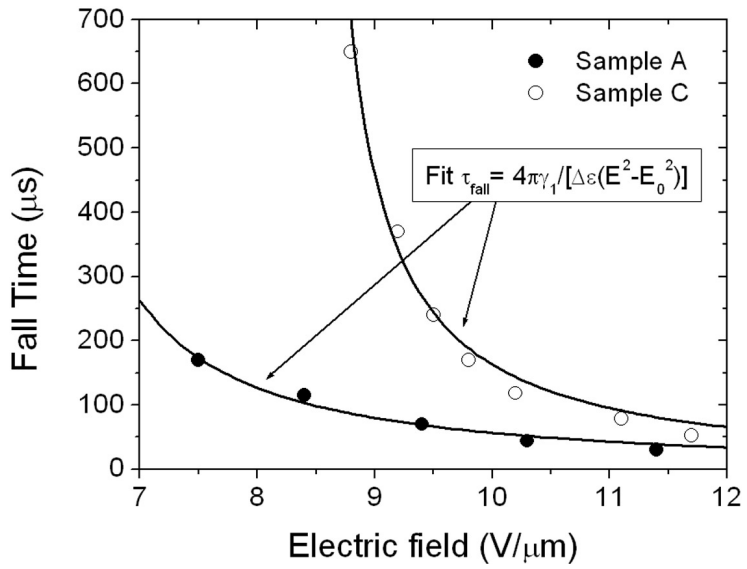

Figure 5.10: Fall time dependence on the applied field, experimental points and fit.

5.5.2 A model for Policryps dynamics: switching off

First of all, two samples characterized by different geometrical properties, namely samples A and C described in Tab. 5.1, were analyzed. The two sample also differ for the curing conditions; in particular they have been produced under a different vibration control, quite rough for sample A, much more refined for sample C.

In these measurements only red probe light was used, because the pitch of sample C was too small to satisfy the Bragg's law for $\lambda = 1550\,\mathrm{nm}$. At the respective Bragg angles, both gratings exhibited high diffraction efficiency, 95% and 93% respectively. Dynamic behavior was studied by applying a series of alternate electric pulses, as in Fig. 5.7, generated by a PC driven arbitrary waveform generator and amplified by a suitable external amplifier. In contrast to the previous measurements, no high frequency modulation was superimposed to the pulses, as pulse duration was always short enough to prevent unwanted conduction effects.

In order to check possible variations of the response times, both the pulse amplitude and duration were varied, respectively in the range $7.5 \div 11.7\ \mathrm{V}/\,\mu\mathrm{m}$ and $0.1 \div 10\,\mathrm{ms}$.In all cases it was verified that pulses were able to completely switch off the grating. Analogously, the pulse time delay was kept greater than $30\,\mathrm{ms}$, so that grating had always enough time to restore the undistorted ON state. Time constant measurements were carried out by the oscilloscope as for the previous set of data; however, the careful design of the voltage waveform led to a reduced uncertainty of about 5%, mainly due to fluctuations in the maximum amplitude of the optical signal.

Experimental values of the samples' fall times for different pulse amplitudes are shown in Fig. 5.10. Experimentally, it was first determined the minimum voltage required to obtain a complete switching off; then, the voltage was increased stepwise up to reach a saturation in the fall times. As expected, for both samples it was found that a higher electric field corresponds to a faster response time. However, this dependence was much more evident in sample C than in sample A. For the former, a variation in the range $50 \div 650\,\mu\mathrm{s}$ was measured, while for the latter exhibited reorientation times within the narrower interval $30 \div 170\,\mu\mathrm{s}$ (cf. Tab. 5.3).No dependence on the pulse duration was observed, as natural.

The fall time dependence on the pulse amplitude can be well understood considering the particular structure of Policryps gratings. In these material, LC molecules are confined both from the polymer slices and the cell glass slabs (see Fig. 3.7). However, the first interaction looks much more important, for the double reason that 1) the alignment is likely induced by the polymer (glass slabs do not undergo any aligning treatment) and 2) the effective distance L between the polymeric slices, i.e. the thickness of LC films, is much shorter than the cell thickness d. In fact, it can be assumed that L does not exceed 30% of the nominal pitch, proportionally to the LC concentration in the photosensitive mixture. Thus, one gets $L \lesssim 0.40\,\mu\mathrm{m}$ for sample A and $L \lesssim 0.18\,\mu\mathrm{m}$ for sample C. These are (maximum) theoretical values, calculated by assuming a complete material separation during the fabrication process. Actually, one does expect shorter experimental values.

	Fall Time (μs)		Rise Time (μs)	
	min	max	min	max
Sample A	30	170	180	1040
Sample C	50	650	130	280

Table 5.3: Response time ranges for the second set of dynamic measurements.

When an external voltage is applied to the cell electrodes, an electric field is created orthogonally to the LC director, which in the undistorted configuration is perpendicular to the polymer slices. This experimental geometry is quite similar to a bend distortion in a Fréedericksz experiment (Fig. 1.3). It is thus reasonable to fit the experimental values of τ_{fall} with the expression ruling the reorientation time constant in presence of electric fields (Eq. 1.28)[17]. Of course, the system considered here is more complicated than a simple homeotropic LC cell, because one cannot observe directly the director reorientation, but only the effect produced by the reorientation on the optical response of the grating. Nevertheless, Eqs. 1.28 and 1.30 are useful to understand the experimental behavior of Policryps samples. It is worth noting that those relations have been widely used well beyond the limit-

[17] Note that Eqs. 1.28 and 1.30 refer to the usual exponential time constant τ, which is related to the experimentally measured $10 \div 90\%$ response time τ_{10-90} by means of relation $\tau_{10-90} = 2.2\tau$.

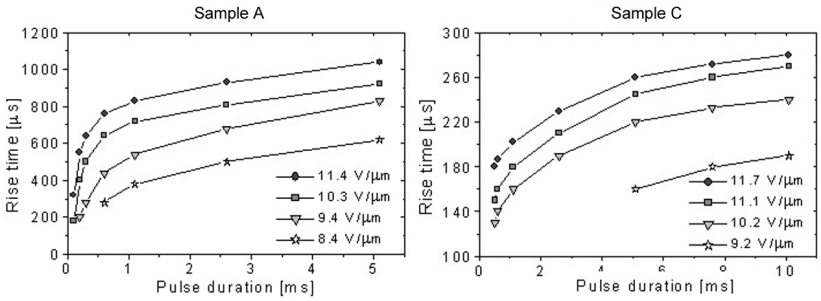

Figure 5.11: Rise time dependence on the pulse duration for different pulse amplitudes.

ing conditions assumed for obtaining them, providing results in good agreement with more sophisticated models [58].

Using for the dielectric anisotropy the value $\Delta\epsilon = 11.5$, experimental data were fitted with Eq. 1.28, with the rotational viscosity γ_1 and the threshold field E_0 chosen as fit parameters; agreement with data points is rather good, as visible in Fig. 5.10). Values obtained for γ_1 are $0.17 \pm\ 0.02\,\mathrm{Pa}\cdot\ \mathrm{s}$ for sample A and $0.22 \pm\ 0.02\,\mathrm{Pa}\cdot\ \mathrm{s}$ for samples C; these values are $3 \div 4$ times larger than the value provided in literature for 5CB at the same reduced temperature ($\sim\ 10^{-2}$ [59]). This difference is likely due to the presence of impurities and residuals of the fabrication process, like polymeric clusters, that affect the LC domains. From the same fit procedure, one obtains for the threshold field E_0 the values $5.9 \pm\ 0.3\,\mathrm{V}/\,\mu\mathrm{m}$ and $8.37 \pm\ 0.04\,\mathrm{V}/\,\mu\mathrm{m}$, for sample A and C, respectively. The ratio of these values, say 1.4, is quite different from the value 2.2, calculated from Eq. 1.22 by using the maximum theoretical width of the LC layers and a value of the band elastic constant $k_3 = 8.4 \times 10^{-12}\,\mathrm{N}$. In fact, putting E_0 fitted values in Eq. 1.22, one gets for the width L of the LC films the values $0.15\ \mu\mathrm{m}$ ($= 0.11 \cdot \Lambda$) and $0.11\ \mu\mathrm{m}$ ($= 0.18 \cdot \Lambda$), for the two samples respectively. Both values are much less than 30% of the grating pitch Λ. Even adopting a simplified model, it seems reasonable to infer that the pitch fraction occupied homogeneously by the liquid crystal is always less than the theoretical maximum and strongly dependent on the fabrication procedure. In particular, the two different results are likely to be related to the different control of the mechanical stability ensured during the curing process to the whole set-up. Larger vibrations produce wider irradiated areas and broader polymer layers.

5.5.3 A model for Policryps dynamics: switching on

Unlike the switching off, the switching on process, which restores the high diffraction state of the grating, is not ruled by the electric field, but only by the elastic torque induced by the surface anchoring. This torque drives the relaxation of the LC director towards the

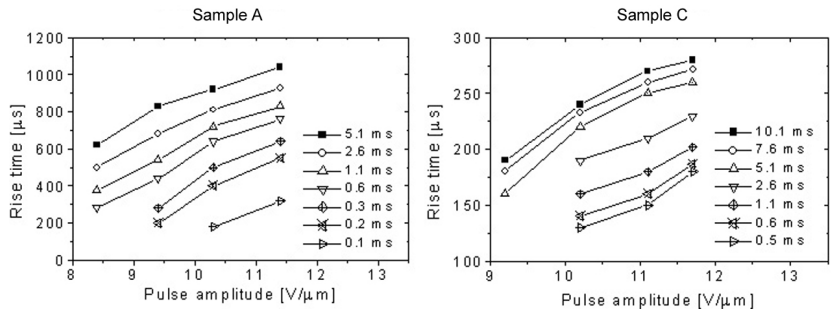

Figure 5.12: Same experimental points as in Fig. 5.11; here rise time is reported versus pulse amplitude for different pulse duration.

initial (zero-field) orientation. Nonetheless, contrary to an intuitive expectation, also the characteristic time of this dynamics (rise time) was found to depend on the pulse shape.

In Fig. 5.11, the non linear dependence of the rise time on the pulse duration is shown for different amplitudes; in Fig. 5.12, the same experimental data, reported versus the pulse amplitude for different values of the pulse duration, show an almost linear behavior. In these experiments, sample A showed the largest variation of the response time values ($180 \div 1040\ \mu$s), while sample C rise time changed only in the range $130 \div 280\ \mu$s (Tab. 5.3). Hence, experimental results indicate that some kind of "memory" of the (previously applied) electric field remains even when only the elastic restoring torque is effective. Moreover, this memory effect is sample dependent.

The observed behavior can be explained by assuming a partial anchoring breaking and restoring, ruled by the surface viscosity, at the LC-polymer interface. In fact, interfacial region is not expected to be very sharp and thin, say of the order of few molecular layers. On the contrary, due to peculiar characteristics of the fabrication process, a 100% completed phase separation is not realistic. Instead it is much more reasonable to consider that a fraction of the LC molecules remains partially embedded in the adjacent polymer slices, close to the border; these interfacial LC molecules can retain some reduced mobility. Moreover, the curing interference pattern has not a rectangular profile, but instead a $\cos^2$ one. Thus, one expects a reduced number of polymeric links to be formed close to the LC-polymer border. Finally, the degree of spatial stability of the pattern does certainly affect the width and softness of the interfacial region.

By the above indications, the following scenario appears quite realistic: when the electric field is switched on, surface and bulk molecules reorient with a different viscosity, corresponding to different time constants. Bulk response is faster and is responsible for the strong reduction of the diffraction efficiency. The response of the surface layer is slower but its influence on the optical signal is almost negligible, because this layer is much thinner than the whole LC film. When the electric field is switched off, the boundary configuration plays the

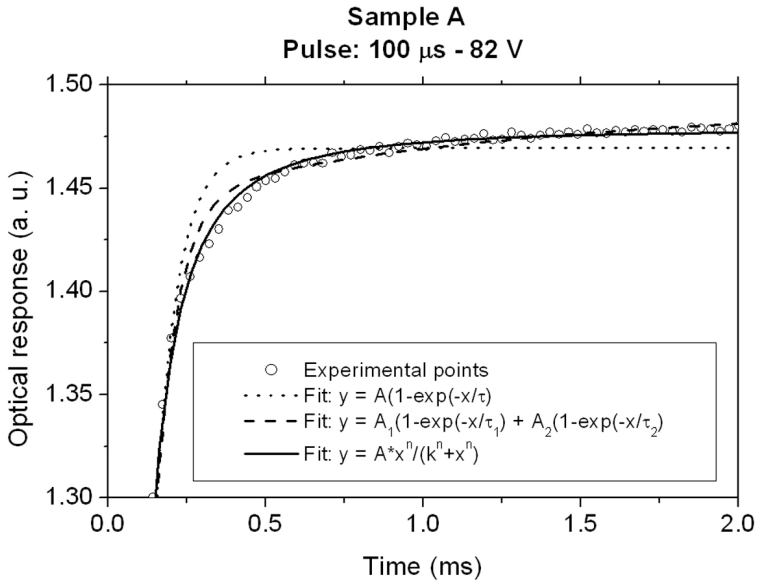

Figure 5.13: Diffracted beam optical signal (circles) during the OFF-ON transition; lines show different fitting curves.

main role in the relaxation process, and, when it is the case, also in determining the fall time dependence on the pulse shape. Short and/or weak electric pulses are not able to affect significantly the reorientation of the director in the boundary region and only bulk molecules reorient and relax, respectively. This means that in this case our LC film should behave like a homeotropic LC cell with strong anchoring conditions. It can be studied in the framework of the Fréedericksz transition model, and Eqs. 1.28 and 1.30 should apply.

Putting in the last equation the data for γ_1 and L obtained from our fit, one obtains for the elastic relaxation time of the two samples the values $110 \pm 20\,\mu$s and $68 \pm 7\,\mu$s, respectively. These can be considered as limiting values, attainable in the case of a perfect, namely sharp and rigid, interface between the LC film and the polymer slice. Obviously, these values are smaller than the smallest measured relaxation times.

For long and/or strong pulses, also the molecules in the interfacial region are partially reoriented by the applied electric field. These molecules exhibit a higher surface viscosity and, in order to resume the initial orientation, need more time than the bulk ones. At the removal of the electric field, the molecular director in the bulk undergoes a first quick reorientation towards the intermediate orientational state held by the director at the surface. Then, the director at the surface will relax towards the unperturbed state with a slower time constant and the bulk director will follow it adiabatically. The final result is that the overall relaxation process is ruled by a mix of the bulk and surface time constants, and depends on the intermediate state of reorientation reached by the director at the surface, under the action of the applied electric field.

This hypothesis can also account for the quite complex shape of the relaxation optical signal. As reported by several authors, the time dependence of an optical signal in a LC cell is a complex function of the reorientation angle [58]. Anyway, in most cases a single time constant is sufficient for describing quite satisfactorily the studied process. When this is not the case, and, for instance, two well recognized different time constants emerge from experimental data, this is generally assumed as an indication for two different physical phenomena playing a role in the process [60].

For studied Policryps samples a good fit of the experimental relaxation curves is obtained only by using a double exponential, or some kind of sigmoid curve, Fig. 5.13. At the present stage, it is not possible to infer a direct physical meaning for the parameters entering in these mathematical formulae. Probably, they are just a good approximation of the real behavior. Anyway, all these functions have a common general shape, with a fast growing part, followed by a very slow saturation tail. It was never possible for a single time constant function fit the experimental data. It is another suggestion of the existence of different bulk and surface viscosity values.

Finally, from an application point of view, it must be stressed that, choosing short driving pulses and a proper voltage, it is possible to get simultaneously both rise and fall response times in the range $50 \div 150\,\mu$s. Furthermore, as mentioned above, the large value of the bulk viscosity found in the LC films determines the limiting values for the attainable response times: optimization of the fabrication process would have a positive effect also in lowering the viscosity, hence on the switching dynamics.

Chapter 6
Optical characterization of soft materials

6.1 Introduction

It has been seen in the previous chapters how the knowledge of the material optical properties is important to correctly predict the behavior of holographic gratings. If this is not crucial for gratings recorded in ordinary mono-phase materials, it is instead essential when dealing with multi-phase systems, like LC-polymer composites (Sec. 4.4). Because polymer and liquid crystal refractive indices change in a different measure with the wavelength (and the temperature), it is clear that the optical contrast, and the grating behavior with it, do not remain constant over a wide range of wavelengths (and temperatures).

The problem is even greater when these materials are considered for telecom applications, which typically operate in the NIR range. At these wavelengths the optical properties of polymers and in particular of liquid crystals are almost unknown, even for the most common compounds. For this reason, the optical characterization of the materials used in switchable gratings was a complementary activity of the work of thesis.

The measurements of polymer optical constants is rather straightforward. In contrast liquid crystals present some specific difficulties that make measurements much less trivial: for their intrinsic nature, liquid crystal films are highly anisotropic, partly depolarizing and inhomogenous; samples consist of thick multilayer stacks, including the glass substrates and the alignment layers; finally their optical properties are extremely sensitive to temperature and impurities.

Two different techniques were used to perform spectroscopic measurements on polymers and liquid crystals, spectroscopic ellipsometry and half-leaky guided mode (HLGM) technique. Both of them are discussed in this chapter. The focus is more on the potentialities and drawbacks of each method, especially in regard to liquid crystals; for more detailed descriptions of the techniques proper references are provided. The chapter ends with some interesting results obtained for 5CB and E7 liquid crystals.

Part of the described measurements have been published [61], for others, papers are in preparation [62].

6.2 Experimental techniques

6.2.1 Spectroscopic ellipsometry

Standard spectroscopic ellipsometry [63, 64] is based on the measurement of two physical quantities, the relative phase change Δ and the relative amplitude change Ψ, suffered by the incident light when reflected (or transmitted) by a layered structure. This technique is very powerful, as Ψ and Δ spectra, possibly measured at various incidence angles, can provide information on thickness and optical constants of all the layers composing the sample.

By the adoption of the 2×2 Jones matrix formalism [63], ellipsometry can be extended to the characterization of anisotropic media (generalized ellipsometry, GE). In this way it is possible to generalize the standard ellipsometry parameters, Δ and Ψ, to the case in which the interaction with the sample changes the light polarization state. The six GE parameters, Δ, Ψ, Δ_{ps}, Ψ_{ps}, Δ_{sp}, Ψ_{sp}, are linked to the Jones matrices of reflected (J_r) or transmitted (J_t) beam through the following equations:

$$\begin{aligned} \tan\Psi \cdot e^{i\Delta} &= \frac{J_{pp}}{J_{ss}} \\ \tan\Psi_{ps} \cdot e^{i\Delta_{ps}} &= \frac{J_{ps}}{J_{pp}} \\ \tan\Psi_{sp} \cdot e^{i\Delta_{sp}} &= \frac{J_{sp}}{J_{ss}} \end{aligned} \tag{6.1}$$

where $J = J^r$, J^t and

$$J^r = \begin{pmatrix} r_{pp} & r_{sp} \\ r_{ps} & r_{ss} \end{pmatrix} \text{ and } J^t = \begin{pmatrix} t_{pp} & t_{sp} \\ t_{ps} & t_{ss} \end{pmatrix} \tag{6.2}$$

with r_{pp}, r_{ss}, r_{ps}, r_{sp} (t_{pp}, t_{ss}, t_{ps}, t_{sp}) representing the reflection (transmission) coefficients for p-, s-, and cross-polarizations respectively. In the isotropic case the Jones matrices are diagonal, and Eqs. 6.1 reduce to the first one, as for standard ellipsometry. However, Jones matrix off-diagonal elements also vanish for anisotropic uniaxial media, provided that the optical axis is oriented parallel or perpendicular to the plane of incidence [67]; this condition makes possible a simpler analysis of complex birefringent materials, like liquid crystals.

The Jones matrix formalism is based on the assumption of a completely polarized light. Therefore, when a significant amount of reflected or transmitted light becomes depolarized, it may be necessary to introduce the Mueller matrix representation [63]]. In this scheme, a 4×4 Mueller matrix $\underline{\mathbf{M}}$ connects the Stokes vectors representing the polarization state of

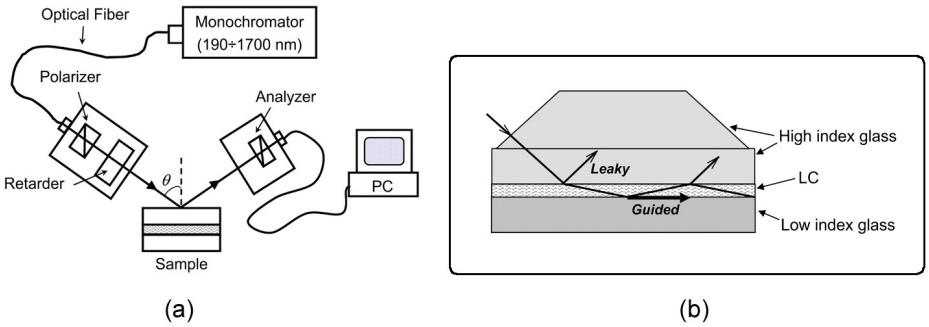

Figure 6.1: Scheme of the VASE ellipsometer (a). Typical HLGM sample, including the high index coupling prism (b).

the input ($\mathbf{S}_{IN}$) and output beam ($\mathbf{S}_{OUT}$)

$$\begin{pmatrix} S_0 \\ S_1 \\ S_2 \\ S_3 \end{pmatrix}_{OUT} = \begin{pmatrix} M_{11} & M_{12} & M_{13} & M_{14} \\ M_{21} & M_{22} & M_{23} & M_{24} \\ M_{31} & M_{32} & M_{33} & M_{34} \\ M_{41} & M_{42} & M_{43} & M_{44} \end{pmatrix} \cdot \begin{pmatrix} S_0 \\ S_1 \\ S_2 \\ S_3 \end{pmatrix}_{IN} . \tag{6.3}$$

Due to the fluctuations of the molecular director, liquid crystals, even in the nematic phase, always manifest a certain depolarizing effect, so a measurement of the Mueller matrix corresponding to the LC sample is often necessary to obtain reliable results on this kind of materials (Mueller matrix ellipsometry, MME). This is not a simple task, but the advanced Variable Angle Spectroscopic Ellipsometer (VASE), by J. A. Woollam Company, is able to perform it, taking advantage of a rotating polarizer with adjustable retarder incorporated in input module[18] (Fig.6.1a).

Once the experimental data are acquired, it is necessary to convert them into final values for the unknown sample parameters, typically optical constants and/or thickness. This task is accomplished by a specific software provided with the instrument. Its operating principle is shown in Fig. 6.2. First, it is necessary to draw up an optical model for the sample, specifying for each constituent layer which parameters are known, and which ones must be calculated starting from reasonable initial values. Software generates theoretical values from the model and compares them with the measured ones; it iteratively changes the fit variables, until the mean square error (MSE), representing the discrepancy between experimental and model-generated data, reaches a minimum.

Spectroscopic, variable angle ellipsometry is a very powerful and sensitive technique that can provide a great amount of detailed information on geometrical and optical properties

[18] Due to the absence of a retarder in the output module, VASE ellipsometer can measure only the elements in the first three rows of $\underline{\mathbf{M}}$, each one normalized to M_{11}. Fortunately, for most materials, including LC samples, remaining elements are unnecessary due to the simmetry of $\underline{\mathbf{M}}$ [68, 69].

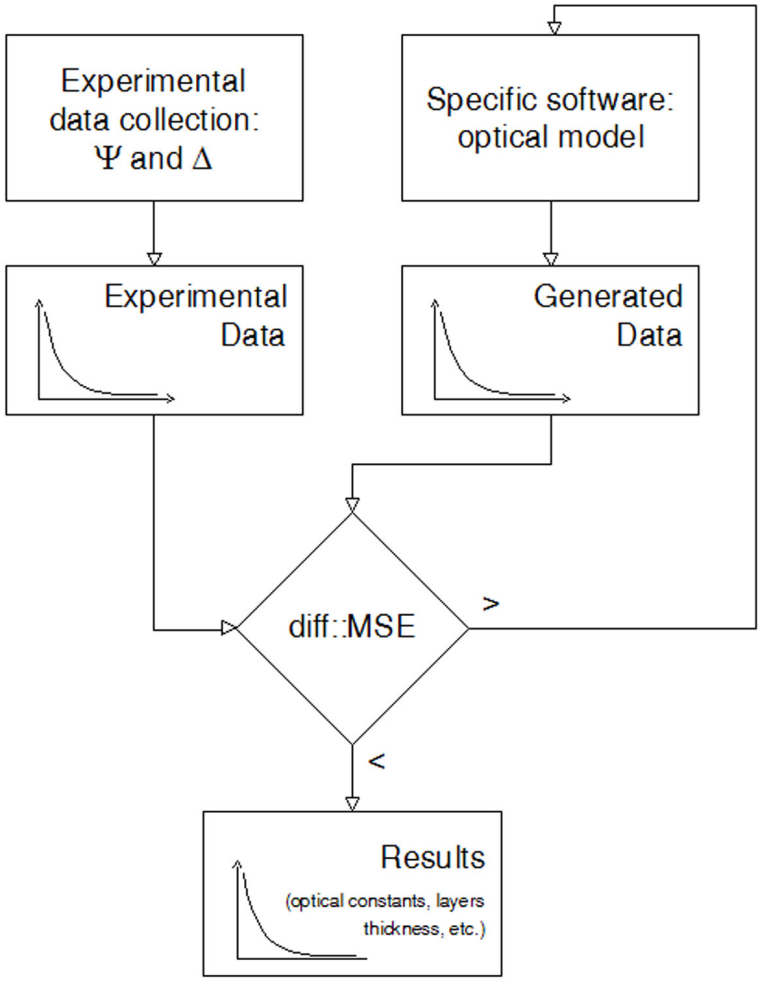

Figure 6.2: Spectroscopic GE data analysis flow chart.

of the studied sample, over a wide and almost continuous spectral range. Its main drawbacks are connected with: 1) accuracy of the optical model; 2) a proper choice of the initial values in the fitting procedure; 3) statistical correlation among fit parameters.

6.2.2 Half-leaky guided mode technique

A common method for measuring refractive index is based on exciting modes of propagation in a guiding structure. This method is suitable to study thin films of materials deposed on (or sandwiched between) substrates whose optical properties are well-known. The relative values of the refractive indices in the layered sample determines what kind of modes can be excited: confined, leaky, or half -leaky. The measurement method takes different names

accordingly: m-line, fully-leaky guided mode, or half-leaky guided mode technique. The latter is the most appropriate for studying liquid crystals.

In HLGM method, liquid crystal is sandwiched between two glass slabs, the upper one and the lower one, whose refractive indices are respectively higher and lower than LC refractive indices (Fig. 6.1b). At this purpose SF6 glass ($n = 1.8056$ at $\lambda = 0.589\,\mu\mathrm{m}$) and fused silica ($n = 1.4585$ at $\lambda = 0.589\,\mu\mathrm{m}$) were used; both slabs were coated with a thin SiO_x layer ($\sim 30\,\mathrm{nm}$) to induce planar alignment of liquid crystal. In this configuration modes are confined by the substrate, while are leaky on the upper side, hence the name of the technique.

Monochromatic light impinges on the sample through a prism placed in contact with the upper slab and made of the same material; proper matching fluid is used in between. Intensity of the reflected beam is measured for a continuously varying incidence angle. In correspondence of a set of definite angles, light is coupled into the LC film and minima are observed in the reflected light. From the angular position of such minima, refractive index and thickness of the LC layer can be calculated, by using a fitting program based on the Fresnel multiple reflection theory [63].

Compared to ellipsometry, HLGM main advantages are the simple experimental set-up and the ease of data analysis; drawbacks are the need of monochromatic sources, which limits the number of usable wavelengths, and the necessity of high-precision angular data. Both problems have been overcome by adapting VASE ellipsometer to HLGM measurements. In this way the broad spectrum ($0.3 \div 1.7\,\mu\mathrm{m}$) of the ellipsometer Xe lamp and the high precision and accuracy of its rotation stage can be exploited.

6.3 Optical dispersion in liquid crystal

6.3.1 HLGM measurements on liquid crystals

Implementation of a HLGM set-up over a VASE ellipsometer allowed the fast and accurate measurements of liquid crystal ordinary (n_o) and extraordinary (n_e) refractive indices. A LC cell was realized according to the HLGM requirements and placed with a prism on the ellipsometer sample holder, as described above; nematic molecular director was in the plane of the cell, in vertical direction. As the ellipsometer plane of incidence lies horizontally, TE and TM propagation modes were excited by s- and p-polarized incident light, respectively ; in the first case, light is sensitive to n_o, in the second case to n_e. Angular spectra were recorded for eight wavelengths ($\lambda = 0.532$, 0.6328, 0.7, 0.8, 1.064, 1.3, 1.55, and $1.7\,\mu\mathrm{m}$), selected by the ellipsometer monochromator.

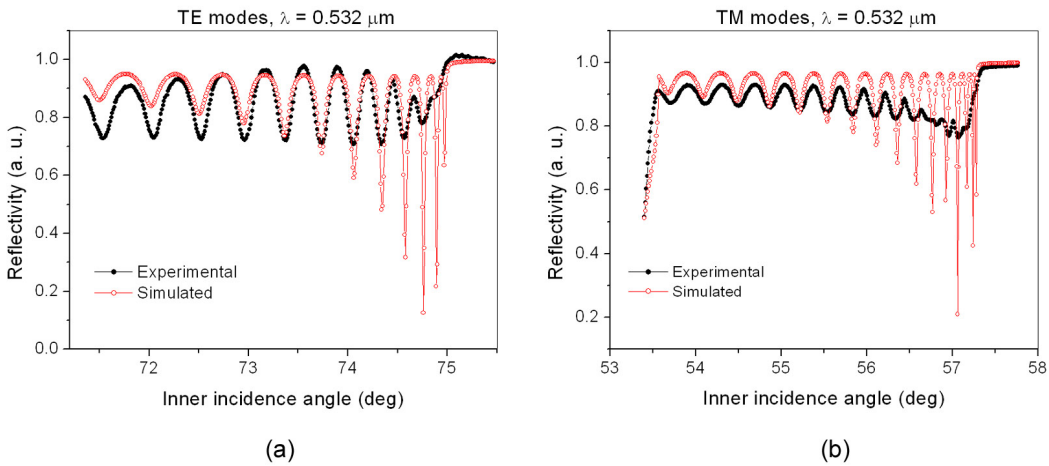

Figure 6.3: HLGM angular spectra for E7 liquid crystal at $\lambda = 0.532\,\mu\mathrm{m}$: TE modes ($a$), and TM modes ($b$).

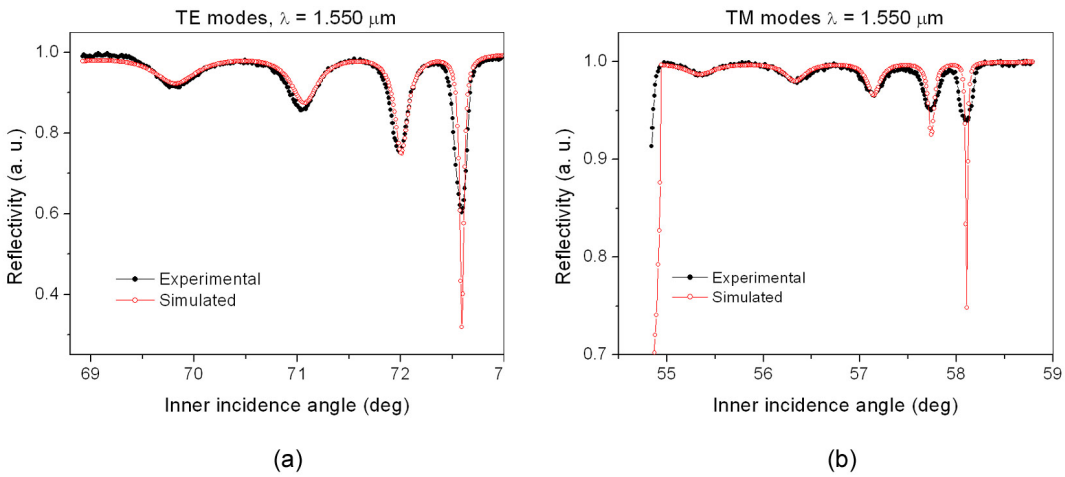

Figure 6.4: HLGM angular spectra for E7 liquid crystal at $\lambda = 1.550\,\mu\mathrm{m}$: TE modes ($a$), and TM modes ($b$).

Graphs in Figs. 6.3 and 6.4 show typical HLGM angular spectra for the E7 liquid crystal, and the respective best-fit curves. Here the horizontal axes represent the internal incidence angle, calculated at the upper glass-LC interface. At $\lambda = 0.532\,\mu\mathrm{m}$ modes at the right–hand side of the experimental curve are partially overlapped, due to the limited monochromaticity of the ellipsometer light source; however, although the limited spectral resolution, experimental data can still be fitted precisely because of the presence of a large number of excited modes. Furthermore only the peak location, and not the overall curve shape, is important for index evaluation. On the other side, in the NIR range modes are more spaced and always well resolved.

In Fig. 6.3b and 6.4b spectra appear left-limited by a cut-off angle; for incidence angles below the such value reflectivity drops off to zero, because the light is no longer confined in the LC layer, but penetrates the substrates. The cut-off angle only depends on the upper and lower slab refractive indices, therefore it can be used to set the zero of the angular scale with accuracy of $\pm\ 0.01\,^{\circ}$. Such accuracy guarantees the determination of the refractive index within ± 0.0002. In this condition temperature remains the main source of error: for instance, according to Ref. [70], a temperature variation $T_{N-I} - T = 5.5 \pm 1\,\mathrm{K}$ produces a change in 5CB refractive indices of $\pm 1.5 \times 10^{-3}$ and $\pm 5 \times 10^{-3}$, respectively for n_o and n_e.

An advantage of HGLM is the possibility to fit the refractive index and the LC layer thickness independently. In fact, the refractive index determines the location of the first minimum, while the film thickness influences the number of excited modes and the relative spacing. This gives the possibility to easily determine both the refractive index and the thickness unambiguously, in contrast with some optical measuring techniques which are sensitive to the product of these layer parameters.

The values of n_o and n_e for E7 and 5CB obtained from the fit of the reflectivity curves are presented in Fig.3a and Fig.3b respectively.

6.3.2 Ellipsometric measurements on liquid crystals

Recently generalized and Mueller matrix ellipsometry have been used to measure liquid crystal refractive indices [61, 69, 71]. However, obtaining accurate ellipsometric measurements of the LC optical parameters still presents some difficulties. When working in reflection, the basic problem is the presence of glass substrates, whose refractive index is comparable to those ones of liquid crystal; as a consequence, the greatest part of the reflected signal comes from the air-glass interface, rather than from the glass-LC interface. On the other side, when working in transmission the correlation between d, n_o and n_e is very high, as the light is sensitive to the product $d\,(n_e - n_o)$; varying the sample orientation can partially overcome the problem, but the final result remains affected by the initial guess of fitting parameters.

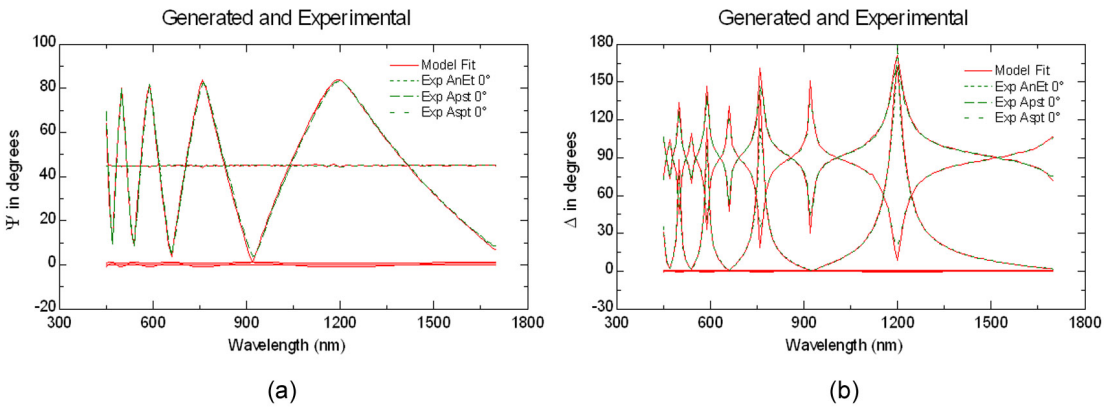

Figure 6.5: Fit of the GE parameters: Ψ, Ψ_{ps}, and Ψ_{sp} in (a); Δ, Δ_{ps}, and, Δ_{sp} in (b).

A better solution to the problem is to complement the ellipsometric measurements with other independent measurements; in this case the values for thickness and refractive indices obtained by HLGM technique have been used as initial values in the fitting procedure.

Experimentally, generalized and Mueller matrix ellipsometric data were acquired at normal incidence in transmission configuration; samples were usual planar liquid crystal cells, oriented with the optical axis making an angle of $\varphi \sim 45\,^{\circ}$ with the plane of incidence. Data were fitted with a stepwise procedure, in which the different parameters were fitted separately:

- (a) d and n_o were fixed on the base of HLGM values; GE data were fitted choosing as variable parameters n_e and the angle φ.

  (b) Twist is considered, i.e. a different value of in correspondence of φ the two substrates. Without including twist it is impossible to fit adequately the experimental data; for instance, for E7 a twist of just $2.5\,^{\circ}$ produced a great variation in the generated curves. It is a demonstration of the high sensitiveness of the ellipsometric measurements.

  (c) All the parameters are fixed apart from the thickness; only specific Mueller matrix elements that are sensitive to d are fitted.

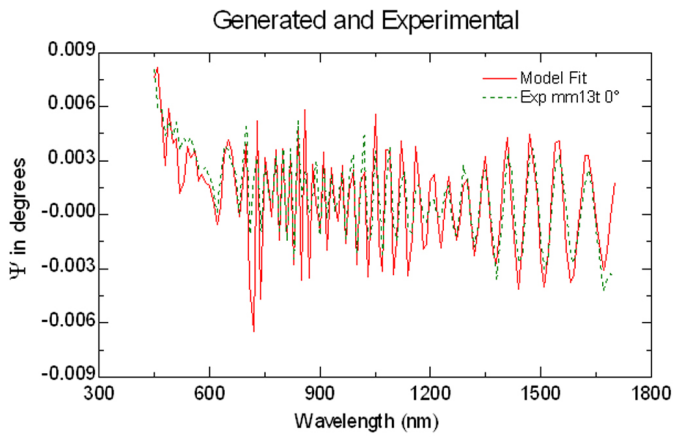

Figure 6.6: Ellipsometric fit of one of the Mueller matrix elements. Oscillations are sensitive to the cell thickness.

(d) All experimental data are fitted with only n_e variable.

(e) Points 3 and 4 are repeated until MSE cannot be further minimized (final results for E7 are shown in Figs. 6.5 and 6.6)..

The main features of this procedure are:

- initial guess uncertainty is greatly reduced due to the adoption of HLGM results;
- in respect to simple GE measurements, thickness and birefringence can be resolved, exploiting the thickness dependent oscillations of some MM elements;
- only n_e, or equivalently the birefringence, is measured, because at normal incidence it is impossible to distinguish the individual contribution of the two refractive indices; this could be done, even if with a reduced accuracy, by taking additional measurements at different incidence angles. However, the ellipsometric measurement of n_e is independent of that one obtained by HLGM; thus, it makes sense to compare the results to check the accuracy of the final data.

6.3.3 E7 and 5CB dispersion spectra

Combining HGLM with ellipsometry, accurate and precise measurements have been carried out on 5CB and E7 liquid crystals. As these materials are transparent over tho whole range of interest, the refractive index dependence on wavelength can be described by a three

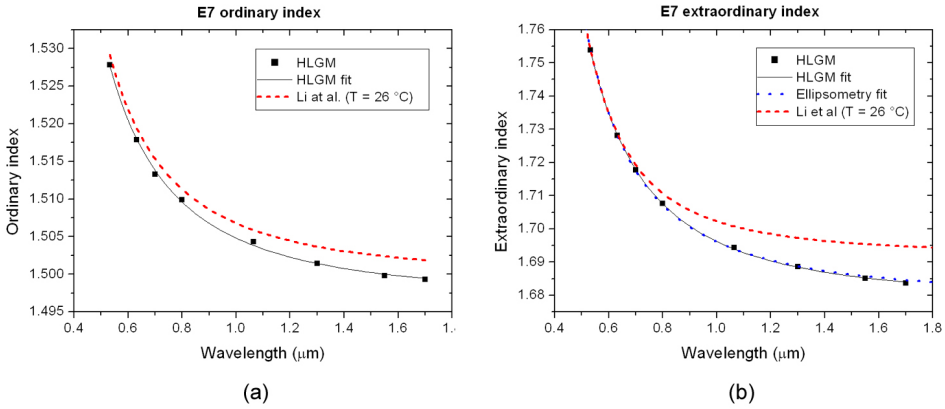

Figure 6.7: E7 dispersion curves: ordinary refractive index (a) and extraordinary refractive index (b).

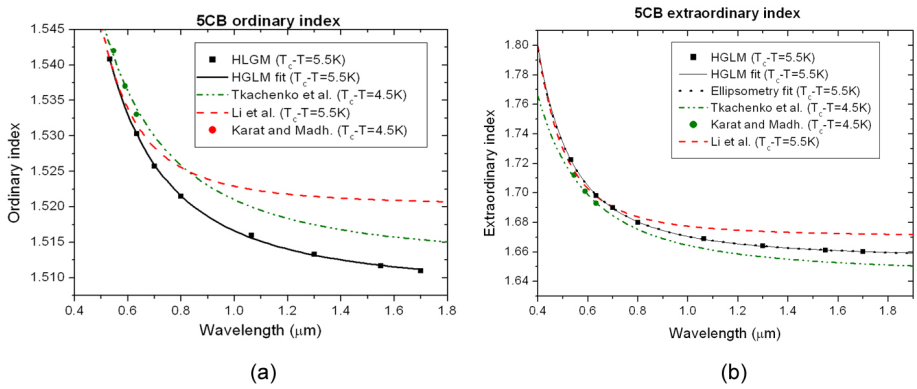

Figure 6.8: 5CB dispersion curves: ordinary refractive index (a) and extraordinary refractive index (b).

parameter Cauchy model [7]

$$n_{o,e} = A_{o,e} + \frac{B_{o,e}}{\lambda^2} + \frac{C_{o,e}}{\lambda^4}. \tag{6.4}$$

This model has been used to fit the discrete HGLM measurements, obtaining the values of Cauchy parameters presented in Tab. 6.1; the agreement between HGLM data and Cauchy fit is very good, as shown in Figs. 6.7 and 6.8. As explained, the values of thickness and ordinary index measured in this way were used as initial guess for fitting ellipsometric data; results are practically indistinguishable from the HGLM data, this proving the accuracy of the measurement.

Final values were also compared to the few data available in literature: Ref. [72] for E7, and Refs. [70, 73] plus our previous work [61] for 5CB. Discrepancies are evident mainly

LC	$\mathbf{A}_o$	$\mathbf{B}_o\left(\mu\mathrm{m}^2\right)$	$\mathbf{C}_o\left(\mu\mathrm{m}^4\right)$	$\mathbf{A}_e$	$\mathbf{B}_e\left(\mu\mathrm{m}^2\right)$	$\mathbf{C}_e\left(\mu\mathrm{m}^4\right)$
5CB	1.50849	0.00774	0.00040	1.65535	0.01355	0.00153
E7	1.49669	0.00785	0.00026	1.67798	0.01696	0.00127

Table 6.1: Cauchy coefficients for 5CB and E7 refractive indices.

in the infrared. However, two factors should be considered: first, results reported in [72] and [70] are affected by a great uncertainty in the IR comparable or higher then the difference with our data; actually results in the NIR were extrapolated by measurements in the visible [70] or based on just too few points (at $1.55\,\mu\mathrm{m}$ and $10.6\,\mu\mathrm{m}$) [72]. More problematic is the partial disagreement with our previous ellipsometric measurement. Here a possible explanation can regards, on one hand, the initial guess biasing of the past ellipsometric approach, on the other side a difference in the sample temperature. In both cases sample was not thermostabilized. However there were at least 1K of difference between the two sets of measurements; considering this the discrepancy is much reduced.

Final values for the E7 and 5CB Cauchy parameters are presented in Tab. 6.1.

Bibliography

[1] L. Eldada, *Rev. Sci. Instrum.* **75**, 575 (2004).

[2] R. L. Sutherland, L. V. Natarajan, V. P. Tondiglia, and T. J. Bunning, *Chem. Mater.* **5**, 1533 (1993).

[3] R. L. Sutherland, L. V. Natarajan, V. P. Tondiglia, T. J. Bunning, and W. W. Adams, *Appl. Phys. Lett.* **64**, 1074 (1994)

[4] L. V. Natarajan, R. L. Sutherland, T. J. Bunning, and V. P. Tondiglia, *Proc. SPIE* **3292**, 44 (1998).

[5] P. G. De Gennes and J. Prost, *The physics of liquid crystals*, 2nd ed. Oxford University Press (1993).

[6] S. Chandrasekhar, *Liquid crystals*, Cambridge University Press (1977).

[7] M. Born and E. Wolf, *Principles of optics: electromagnetic theory of propagation, interference and diffraction of light*, 7th ed. Cambridge University Press (1999).

[8] F. Simoni, *Nonlinear optical properties of liquid crystals and polymer dispersed liquid crystals*, World Scientific (1997).

[9] B.-G. Wu, J. H. Erdmann, and J. W. Doane, *Liq. Cryst.* **5**, 1453 (1989).

[10] P. Hariharan, *Optical holography: principles, techniques and applications*, 2nd ed. Cambridge University Press (1996).

[11] T. K. Gaylord and M. G. Moharam, *Proc. IEEE* **73**, 894, (1985).

[12] H. Kogelnik, *Bell Syst. Tech. J.* **48**, 2909 (1969).

[13] G. Montemezzani and M. Zgonik, *Phys. Rev. E* **55**, 1035 (1997).

[14] R. Caputo, C. Umeton, A. Veltri, A. Sukhov, and N. Tabiryan, patent number WO2005006065 (January 20, 2005).

[15] J. Stumpe, O. Sakhno, and S. Slussarenko, reference number 04f45088-iap.

[16] T. J. Bunning, L. V. Natarajan, V. P. Tondiglia, and R. L. Sutherland, *Annu. Rev. Mater. Sci.* **30**, 83 (2000).

[17] R. T. Pogue, L. V. Natarajan, S. A. Siwecki, V. P. Tondiglia, R. L. Sutherland, and T. J. Bunning, *Polymer* **41**, 733 (2000).

[18] M. De Sarkar, N. L. Gill, J. B. Whitehead, and J. P. Crawford, *Macromolecules* **36**, 630 (2003).

[19] L. V. Natarajan, C. K. Shepherd, D. M. Brandelik, R. L. Sutherland, S. Chandra, V. P. Tondiglia, D. Tomlin, and T. J. Bunning, *Chem. Mater.* **15**, 2477 (2003).

[20] R. Caputo, L. De Sio, A. Veltri, C. Umeton, and A. V. Sukhov, *Opt. Lett.* **29**, 1261 (2004).

[21] O. Sakhno, S. Slussarenko, and J. Stumpe, *Proc. SPIE* **5521**, 38 (2005).

[22] G. Strangi, V. Barna, R. Caputo, A. De Luca, C. Versace, N. Scaramuzza, C. Umeton, R. Bartolino, and G. N. Price, *Phys. Rev. Lett.* **94**, 063903 (2005).

[23] M. Date, Y. Takeuchi, and K. Kato, *J. Phys. D: Appl. Phys.* **31**, 2225 (1998).

[24] J. N. Eakin, G. P. Crawford, and M. D. Radcliffe, *Mol. Cryst. Liq.Cryst*. **439**, 1889 (2005).

[25] R. L. Sutherland, L. V. Natarajan, V. P. Tondiglia, S. Chandra, C. K. Shepherd, D. M. Brandelik, S. A. Siwecki, and T. J. Bunning, *J. Opt. Soc. Am. B* **19**, 3004 (2002).

[26] B. Pilot, Y. B. Boiko, and T. V. Galstyan, *Proc. SPIE* **3638**, 26 (1999).

[27] P. Nagtegaele and T. V. Galstian, *Synth. Met.* **127**, 85 (2002).

[28] T. J. Bunning, L. V. Natarajan, V. P. Tondiglia, and R. L. Sutherland, *Proc. SPIE* **2651**, 44 (1996).

[29] M. E. Holmes and M. S. Malcuit, *Phys. Rev. E* **65**, 066603 (2002).

[30] L. V. Natarajan, R. L. Sutherland, V. P. Tondiglia, T. J. Bunning, and W. W. Adams, *J. Nonlin. Opt. Phys. Mater.* **5**, 89 (1996).

[31] J. Klosterman, L. V. Natarajan, V. P. Tondiglia, R. L. Sutherland, T. J. White, C. A. Guymon, and T. J. Bunning, *Polymer* **45**, 7213 (2004).

[32] R. L. Sutherland, V. P. Tondiglia, L. V. Natarajan, and T. J. Bunning, *Appl. Phys. Lett.* **79**, 1420 (2001).

[33] A. Y.-G. Fuh, T.-C. Ko, M.-S. Tsai, C.-Y. Huang, and L.-C. Chien, *J. Appl. Phys.* **83**, 679 (1998).

[34] R. Caputo, A. V. Sukhov, and C. Umeton, *Chem. Phys.* **245**, 463 (1999).

[35] C. C. Bowley and G. P. Crawford, *Appl. Phys. Lett.* **76**, 2235 (2000).

[36] J. Qi, M. DeSarkar, G. T. Warren, and G. P. Crawford, *J. Appl. Phys.* **91**, 4795 (2002).

[37] J. Qi, L. Li, M. DeSarkar, and G. P. Crawford, *J. Appl. Phys.* **96**, 2443 (2004).

[38] R. Caputo, A. V. Sukhov, N. V. Tabirian, C. Umeton, and R. F. Ushakov, *Chem. Phys.* **271**, 323 (2001).

[39] A. Veltri, R. Caputo, C. Umeton, and A. V. Sukhov, *Appl. Phys. Lett.* **84**, 3492 (2004).

[40] D. E. Lucchetta, L. Criante, and F. Simoni, *J. Appl. Phys.* **93**, 9669 (2003).

[41] F. Vita, A. Marino, V. Tkachenko, G. Abbate, D. E. Lucchetta, L. Criante, and F. Simoni, *Phys. Rev. E* **72**, 011702 (2005).

[42] Research Project of National Interest (PRIN 2000) by Italian Ministry of Education and Research, *Devices for routing in optical networks using new liquid crystals materials and composites*.

[43] D. E. Lucchetta, A. Manni, R. Karapinar, L. Gobbi, and F. Simoni, *Mol Cryst. Liq. Cryst.* **375**, 397 (2002).

[44] M. Jazbinsek, I. Drevensek-Olenik, M. Zgonik, A. K. Fontecchio, and G. P. Crawford, *J. Appl. Phys.* **90**, 3831 (2001).

[45] S. Harbour, T. Galstian, R. S. Akopyan, and A. V. Galstyan, *Opt. Commun.* **238**, 261 (2004).

[46] D. E. Lucchetta , L. Criante, and F. Simoni, *Opt. Lett.* **28**, 725 (2003).

[47] A. D'Alessandro, R. Asquini, C. Gizzi, R. Caputo, C. Umeton, A. Veltri, and A. V. Sukhov, *Opt. Lett.* **29**, 1405 (2004).

[48] C. Neipp, A. Beléndez, S. Gallego, M. Ortuño, I. Pascual, and J. T. Sheridan, *Opt. Express* **11**, 1835 (2003).

[49] D. E. Lucchetta, O. Francescangeli, L. Lucchetti, and F. Simoni, *Liq. Cryst.* **28**, 1793 (2001).

[50] H. Kogelnik, *Bell Syst. Tech. J.* **55**, 109 (1976).

[51] R. L. Sutherland, *J. Opt. Soc. Am. B* **19**, 2995 (2002).

[52] J. J. Butler, M. S. Malcuit, and M. A. Rodriguez, *J. Opt. Soc. Am. B* **19**, 183 (2002).

[53] G. Abbate, A. Marino, and F. Vita, *Mol. Cryst. Liq. Cryst.* **398**, 269 (2003).

[54] G. Abbate, A. Marino, and F. Vita, *Acta Phys. Pol. A* **103**, 177 (2003).

[55] A. Marino, F. Vita, V. Tkachenko, R. Caputo, C. Umeton, A. Veltri, and G. Abbate, *Eur. Phys. J. E* **15**, 47 (2004).

[56] G. Abbate, F. Vita, A. Marino, V. Tkachenko, and S. Slussarenko, *Opt. Pur. y Apl.* **38**, 11 (2005).

[57] Research Project of National Interest (PRIN 2003) by Italian Ministry of Education and Research, *New liquid crystal composite materials for opto-electronic devices*.

[58] H. Wang, T. X. Wu, X. Zhu, and S. Wu, *J. Appl. Phys.* **95**, 5502 (2004).

[59] S. T. Wu and C. S. Wu, *Phys. Rev. A* **42**, 2219 (1990).

[60] F. M. Aliev and G. P. Sinha, *Mol. Cryst. Liq. Cryst.* **303**, 325 (1997).

[61] V. Tkachenko, A. Marino, F. Vita, F. D'Amore, L. De Stefano, M. Malinconico, M. Rippa, and G. Abbate, *Eur. Phys. J. E* **14**, 185 (2004).

[62] V. Tkachenko,G. Abbate, A. Marino, F. Vita, M. Giocondo, A. Mazzulla, and L. De Stefano, submitted to *Mol. Cryst. Liq. Cryst.* (2005).

[63] R. M. A. Azzam and N. M. Bashara, *Ellipsometry and polarized light*, North-Holland (1987).

[64] H. G. Tompkins and W. A. McGahan, *Spectroscopic ellipsometry and reflectometry: a user's guide*, John Wiley & Sons (1999).

[65] P. K. Tien, R. Ulrich, and R. J. Martin, *Appl. Phys. Lett.* **14**, 291 (1969).

[66] J. S. Wei and W. D. Westwood, *Appl. Phys. Lett.* **32**, 819 (1978).

[67] H. Touir, M. Stchakovsky, R. Ossikovski, and M. Warenghem, *Thin Solid Films* **455**, 628 (2004).

[68] G. E. Jellison, *Thin Solid Films* **33**, 313 (1998).

[69] J. N. Hilfiker, C. M. Herzinger, T. Wagner, A. Marino, G. Del Gais, and G. Abbate, *Thin Solid Films* **591**, 455 (2004).

[70] J. Li and S. T. Wu, *J. Appl. Phys.* **95**, 896 (2004).

[71] J. N. Hilfiker, B. Johs, C. M. Herzinger, J. F. Elman, E. Montbach, D. Bryant, and P. J. Bos, *Thin Solid Films* **455**, 596 (2004).

[72] J. Li, S. T. Wu, S. Brugioni, R. Meucci, and S. Faetti, *J.Appl. Phys.* **97**, 073501 (2005).

[73] P. P. Karat and N. V. Madhusudana, *Mol. Cryst. Liq. Cryst.* **36**, 51, (1976).